RADIATION FROM SLOTS ON CYLINDRICAL BODIES USING.

GEOMETRICAL THEORY OF DIFFRACTION AND

CREEPING WAVE THEORY

DISSERTATION ·

Presented in Partial Fulfillment of the Requirements for
the Degree Doctor of Philosophy in the Graduate
School of The Ohio State University

By

Constantine A. Balanis, B.S.E.E., M.E.E.

* * * * *

The Ohio State University

1969

Approved by

Adviser
Department of Electrical Engineering

RADIATION FROM SLOTS ON CYLINDRICAL BODIES USING

GEOMETRICAL THEORY OF DIFFRACTION AND

CREEPING WAVE THEORY

ABSTRACT OF
DISSERTATION

Presented in Partial Fulfillment of the Requirements for
Degree Doctor of Philosophy in the Graduate
School of The Ohio State University

By

Constantine A. Balanis, B.S.E.E., M.E.E.

* * * * * *

The Ohio State University

1969

Approved by

_____
Adviser
Department of Electrical Engineering

RADIATION FROM SLOTS ON CYLINDRICAL BODIES USING

GEOMETRICAL THEORY OF DIFFRACTION AND

CREEPING WAVE THEORY

By

Constantine A. Balanis, Ph.D.

The Ohio State University, 1969

Professor Leon Peters, Jr., Adviser

A hybrid solution employing wedge diffraction and creeping wave
theory is used to compute the principal planes (equatorial and
elevation) radiation patterns of axial and circumferential slots on
conducting cylinders of finite and infinite lengths. The slots are
excited by parallel-plate waveguides operating in the TEM and TE_{10}
modes.

For the equatorial plane pattern, the total field in the "lit"
region is obtained by the superposition of two fields; that is, the
wedge-diffracted and the creeping wave fields. The wedge-diffracted
field is obtained by approximating the parallel-plate-cylinder geometry
with two wedges, each formed by a wall of the waveguide and a tangent
plane to the cylinder surface at the edge point. The creeping wave
contribution is obtained by the method commonly employed for the
computation of scattered fields from curved surfaces. The total field

.in the "shadow" region is obtained solely from the creeping wave contribution. For the elevation plane pattern, wedge diffraction techniques for the entire pattern are employed.

The method is checked computationally by comparison with the modal solutions for axial and circumferential slots on right circular cylinders and experimentally for elliptical cylinders since modal solutions are not readily available. Experimental models are also used for the verification of the elevation plane pattern computations since boundary-value solutions are not available for finite length cylinders.

Computed results using this technique compare favorably with those obtained from existing modal expansion boundary-value solutions and experimental results. The main advantages of the present technique are that it can be applied to geometries where modal solutions are not possible, in numerical ranges where the convergence properties of modal expansions are relatively poor, in parametric design problems since the contribution from each field is separated, and in the analysis of antennas with finite physical sizes.

ACKNOWLEDGMENTS

VITA

██████████████████   Born - ████████

1964 . . . . . .   B.S. in Electrical Engineering
                      Virginia Polytechnic Institute
                      Blacksburg, Virginia

1964 - 1969 . .   Aero-Space Technologist
                      NASA Langley Research Center
                      Hampton, Virginia

1966 . . . . . .   Master of Electrical Engineering
                      University of Virginia
                      Charlottesville, Virginia

1968 - 1969 . .   Assistant Professorial Lecturer in Electrical
                          Engineering
                      The George Washington University
                      Washington, D.C.

PUBLICATIONS

"Analysis of Aperture Radiation From an Axially Slotted Circular
  Conducting Cylinder Using Geometrical Theory of Diffraction."
  IEEE Transactions on Antennas and Propagation, AP-17, pp. 93 - 97,
  January 1969.

"Equatorial-Plane Pattern of an Axial-TEM Slot on a Finite Ground
  Plane." IEEE Transactions on Antennas and Propagation, AP-17,
  pp.   -   , May 1969.

"Aperture Radiation From an Axially Slotted Elliptical Conducting
  Cylinder Using Geometrical Theory of Diffraction." IEEE Transactions
  on Antennas and Propagation, AP-17, pp.   -   , July 1969.

"Dielectric Constant and Loss Tangent Measurements at 60 and 90 GHz
  Using the Fabry-Perot Interferometer." (Accepted for publication
  in the Microwave Journal.)

FIELDS OF STUDY

Major Field: Electrical Engineering

Studies in Electromagnetic Field Theory. Professor L. Peters, Jr.

Studies in Antenna Theory. Professor J. H. Richmond

Studies in Control Theory. Professor F. C. Weimer

Studies in Classical Mechanics. Professor W. H. Shaffer

Studies in Mathematics. Professor H. D. Colson

TABLE OF CONTENTS

.

Chapter

LIST OF TABLES

LIST OF ILLUSTRATIONS

INTRODUCTION

The radiation properties of slot antennas on conducting cylinders have been studied extensively.[1-5] Such analyses have been restricted to geometries where modal expansion field functions are readily available and whose physical length is infinite. Moreover, the solutions obtained are poorly convergent for objects more than a wavelength or so in extent. However, many practical problems involve slot antennas mounted on finite size conducting bodies whose geometrical shape does not conform to a coordinate system where the wave equation is separable. Wedge diffraction[6-9] and creeping wave theory are used in the analysis presented here to compute the radiation patterns of axial and circumferential slots on conducting cylinders of finite and infinite lengths. The method employed is an extension of the geometrical theory of diffraction[10,11] and creeping wave theory.[12-16]

The geometrical theory of diffraction and creeping wave theory are extensions of geometrical optics which account for diffraction. They introduce diffracted rays in addition to the usual rays of geometrical optics. These rays are produced by incident rays which hit edges, corners, vertices, or curved surfaces. Some of these diffracted rays enter the shadow regions and account for the field intensity there.

1

The distribution of the incident energy among those diffracted rays is described by a diffraction coefficient. The diffraction of the incident rays is a local phenomenon, so the diffraction coefficient depends on the geometry of the edge or curved surface in the vicinity of the point of diffraction and on the polarization of the incident field.

A field is associated with each diffracted ray and the total field at a point is the sum of the fields of all rays at that point. The phase of the field on a ray is assumed to be proportional to the optical length of the ray from some reference point. Appropriate phase jumps must be added as a ray passes through a caustic. The amplitude is assumed to vary in accordance with the principle of conservation of energy in a narrow tube of rays. The initial value of the field on a diffracted ray is determined from the incident field with the aid of an appropriate diffraction coefficient. These diffraction coefficients are determined from certain canonical problems.

The canonical problem, which yields the diffraction coefficient for an edge, is the diffraction of a linearly polarized plane wave by a two-dimensional, infinite wedge. The diffraction coefficient is found from Sommerfeld's[17] asymptotic, high frequency solution to this problem. Pauli[18] has obtained a practical formulation for the diffraction coefficient and Hutchins[19] has generalized it. He has obtained a series solution which is valid for the exterior and interior regions of a wedge. In addition, his solution is accurate for wedges of large included angles where the Pauli solution is not accurate. Oberhettinger[20] has obtained a similar series in which the leading term is identical to the Fresnel integral form for half-plane diffraction.

The work of Hutchins tends to bridge the solutions of Pauli and Oberhettinger.

The primary task in applying the creeping wave theory is the determination of the diffraction, attenuation, and ray path factors for a general body (and it is not yet always practical). Thus it is · necessary to evaluate these factors for canonical targets whose exact solutions are available, such as the cylinder and sphere.[12-16,21-23] In order to obtain a more general solution for these factors· it is convenient to utilize experimental data to validate an empirical model for more general targets such as the prolate spheroid.[24-26]

The attenuation and diffraction coefficients for a cylinder have been obtained by comparing·the asymptotic series of the scattering boundary-value solution with that of the diffraction problem formulation.[13-16] The ray paths along the surface of the cylinder are geodesics (great circles). The scattering by a sphere is, however, a most important problem. The classical solution of Mie using separation of variables and series techniques can be considered as the starting point. Senior and Goodrich[21] have obtained an asymptotic form to the Mie series solution for the sphere through the application of the Watson transformation. Hong[22] has derived attenuation and diffraction coefficients with higher order correction terms. The formidable task of implementing this solution numerically has yet to be accomplished.

An approach to the general formulation of the creeping wave paths on bodies of revolution has been developed by Kinber.[27] Kinber has shown that the wave equation may be expanded in a set of ray coordinates

in which the solution can be written in a form whose magnitude is dependent upon the cross section of the ray tube and whose phase is dependent only upon the propagation constant and path length traversed.

The empirical approach[24-26] utilizes a simplified ray path geometry to determine approximate attenuation and diffraction coefficients for a sphere. This approach is of interest in that it lends itself to extension to more general targets. This method is a simplified creeping wave analysis. It uses a single nonconvergent (and nondivergent) ray path together with approximate diffraction and attenuation coefficients to construct an approximate solution for the scattered field due to creeping waves propagating in each direction along the ray path. The path chosen is the path traversed by the "major" ray (that is, the path corresponding to the E-plane of the sphere). This analysis suggests that an approximate picture of scattering by a sphere can be constructed by neglecting the creeping waves which have a radial magnetic field (that is, the "minor" creeping waves) and by considering only the creeping waves which have a radial electric field (that is, the "major" creeping waves) except for the H-plane scattered fields.

The prolate spheroid represents a body for which an exact closed form solution is not available except on the axis of rotation. In order to find the ray path geometries for the prolate spheroid for an arbitrary angle of incidence, the geodesic corresponding to the point of attachment and the tangent direction at that point must be calculated. The determination of the tangent direction of the creeping wave at the shadow boundary is not an easy task in general. It is therefore suggested that the simplified ray path geometry[24-26] for the

sphere can be applied to the prolate spheroid. In this case, the creeping wave paths are elliptical, thus the total attenuation must be expressed as an integral which is dependent upon the radius of curvature along the path. Also the radius of curvature at the points of attachment and reradiation must be computed in order to determine the diffraction coefficient. The specific solution for the prolate spheroid has been presented by Ryan[24,26] and Peters and Ryan.[25]

Many other antenna problems have been treated using wedge diffraction techniques. Russo, Rudduck, and Peters[28] applied the geometrical theory of diffraction to calculate the total antenna pattern of a horn in the E-plane, including the backlobe region. Theoretical and experimental patterns are in excellent agreement, thus demonstrating that the method for treating diffraction by edges is valid. Obha[29] used the geometrical method of diffraction to calculate the radiation pattern and gain of a finite width corner reflector antenna. This method yields also good results for the computation of backscattering from an antenna having conducting plates finite in extent.

Extensive work of applying the wedge diffraction method to waveguides has been carried out by Rudduck.[6-9] The principal tool employed is diffraction by a conducting wedge; the resulting electromagnetic field may be treated as a superposition of the geometrical optics field and the diffracted field which behaves as a cylindrical wave radiating from the edge of the wedges. These techniques may be applied to any two-dimensional antenna or scattering body which may be constructed from a set of wedges; the radiation or scattering pattern may be obtained for any excitation which can be expressed in terms of plane or cylindrical

waves by superposition of the individual wedge diffractions. Some elementary examples include parallel-plate waveguides, walls of finite thickness, and polygonal cylinders.

A basic feature of this technique is that it does not require an assumption of the value of the total field or current on some surface, as do conventional methods of aperture integration which employ the approximation of physical optics. This feature thus allows more accurate treatment of problems than ordinarily obtained by approximate methods; it also provides knowledge of the fields in terms of the incident field, thus resulting in the ability to analytically determine admittance and gain of antennas,[6] radiation patterns,[7,8] mutual coupling,[30,31] and reflection coefficient.[32-34]

The geometrical ray techniques of this method provide conceptual simplicity with which solutions may be formulated. This together with superposition of wedges allows structural aspects to be taken into account, for example, antennas mounted with and without ground planes, structures with thin or thick walls, and arbitrary waveguide truncations can be treated. In addition, the fields in all space can be determined, thus allowing backlobe regions to be treated.

Since the introduction of the geometrical theory of diffraction, it has been employed successfully in the solution of various types of diffraction problems. Previous work in applying the wedge diffraction and creeping wave theories, each one individually, to scattering and radiation antenna problems has been outlined. However, no one has attempted a hybrid solution in using both, wedge diffraction and creeping wave theories, on the same scatterer. The work outlined in

the pages to follow, is an attempt to formulate a hybrid solution making use of both wedge diffraction and creeping wave theories on the same antenna. The antenna of interest is a slotted, axially and circumferentially, conducting cylinder. The slots are excited by parallel-plate waveguides operating in the TEM and TE_{10} modes.

The essential feature of this approach is that it is applicable to all types of complicated problems, some of which are impossible to solve rigorously. The approach is to resolve a complicated problem into simpler ones, each of which will have relative simple rigorous solutions. The basic building blocks will be rigorous solutions to such canonical diffraction problems as the wedge, cylinder, sphere, etc., which will be put together to solve more complicated problems.

The work outlined in this hybrid solution will be for general conducting cylinders of arbitrary convex cross section. However, computations will be restricted to circular cylinders for which boundary-value solutions exist for comparison and elliptical cylinders for which models and experimental data are available for comparison. The radiation patterns of interest for each case are the principal plane patterns, equatorial plane ($\theta = 90^{\circ}$) and elevation plane ($\phi = 0^{\circ}$) in the usual spherical coordinate system.

The equatorial plane pattern will be obtained by the superposition of diffracted fields from a set of wedges and creeping wave fields propagating around the surface of the cylinder. The set of wedges approximate the parallel-plate-cylinder geometry in the vicinity of the discontinuity formed by the waveguide and the cylinder. Each wedge is

formed by a wall of the parallel-plate waveguide and the tangent plane
to the cylinder surface at the edge point.

For the equatorial plane pattern, two distinct regions can be
identified: the "lit" and "shadow" regions. The "shadow" region
encompasses the space occupied by the set of wedges and cylinder surface
and the "lit" region the remaining space. The total field in the "lit"
region is obtained by the superposition of two fields; that is, the
wedge-diffracted and creeping wave fields. The total field in the
"shadow" region is obtained solely from the creeping wave contribution.
For the elevation plane pattern, wedge diffraction techniques for the
entire pattern are employed.

The most interesting part of this hybrid solution is the coupling
mechanism between the wedge-diffracted and creeping wave fields.
Creeping waves are launched by the tip of the wedges in a direction
tangent to the cylinder surface at the edge point. Since the field
must be continuous along the line separating the "lit" and "shadow"
regions, the wedge-diffracted fields along the surface of each
wedge will be used as the initial value of the creeping waves to
preserve the continuity of the fields. The creeping waves continually
shed energy in a tangential direction as they propagate around the
cylinder surface until they reach the opposite wall of the slot and
again illuminate the wedges; this is a second order field contribution
and it is neglected. The loss of energy due to reradiation is accounted
by the use of an attenuation factor.

The method is checked computationally by comparison with the modal
solutions for axial and circumferential slots on right circular cylinders

and experimentally for elliptical cylinders since modal solutions are not readily available. Experimental models are used for the verification of the elevation plane pattern computations since boundary-value solutions are not available for finite length cylinders.

Computed results using this technique compare favorably with those obtained from existing modal expansion boundary-value solutions and experimental results. The main advantages of the present technique are that it can be applied to geometries where modal solutions are not possible, in numerical ranges where the convergence properties of modal expansions are relatively poor, in parametric design problems since the contribution from each field is separated, and in the analysis of antennas with finite physical sizes.

CHAPTER I

WEDGE DIFFRACTION

Wedge diffraction techniques are applied for the analysis of the radiation pattern of the parallel-plate waveguide shown in Figure 1. This geometry has been treated using wedge diffraction concepts by Rudduck and his co-workers.[6-9] Their solution is incorporated in the slotted cylinder radiation pattern analysis and will be outlined below. In this approach a single-diffracted wave emanates from each wedge that is illuminated by an incident plane wave. The single-diffracted waves produced by one wedge illuminate the other producing double-diffracted fields. This process continues to higher orders of diffraction.

Single Diffraction

The principal method employed in the analysis of a parallel-plate waveguide is diffraction by a conducting wedge. The diffraction of a plane wave by a wedge was solved by Sommerfeld.[17] Pauli[18] obtained a practical formulation of the solution for a finite angle conducting wedge which was later improved by Hutchins[19] (see Appendix). The total electromagnetic field from the wedge may be treated as the superposition of geometrical optics and of diffracted fields which behave as cylindrical waves radiating from the edge of the wedges.
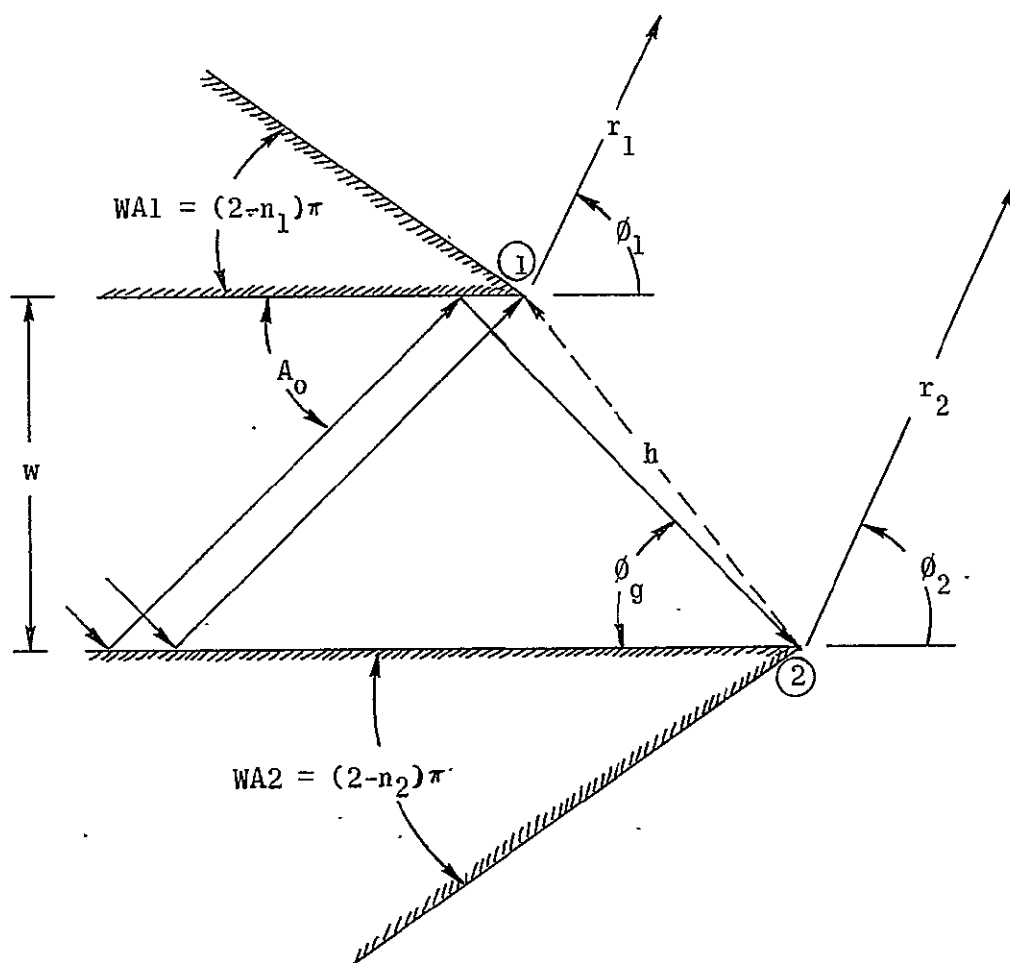
Figure 1. Geometry of a parallel-plate waveguide aperture.

The diffraction of a plane wave by a wedge is shown in Figure 2. The solution to the plane wave diffraction problem may be expressed in terms of scalar functions that represent the normal and parallel polarization components of the electromagnetic field to the plane of study in Figure 2. The total field is defined as

$$E = E_G + E_D \tag{1}$$

where E_G is the geometrical optics field and E_D is the diffracted field. The diffracted field is given by

$$E_D = V_B(r, \psi - \psi_o, n) \pm V_B(r, \psi + \psi_o, n) \tag{2}$$

where the parameters r, ψ, ψ_o, n are defined in Figure 2 and $V_B(r, \psi \pm \psi_o, n)$ is the diffraction function as defined in the Appendix. The plus (+) sign applies for the polarization of the electric field normal to the edge

$$\left(\left. \frac{\partial E}{\partial n} \right|_{wedge} \right) = 0 \tag{3}$$

where n is the unit normal to the edge of the wedge and the minus (-) sign applies for the polarization parallel to the edge

$$\left(E|_{wedge} \right) = 0 \tag{4}$$

The geometrical optics field is defined in three regions, as shown in Figure 2. For plane wave incidence, the geometrical optics field is

INCIDENT
PLANE WAVE

INCIDENT AND REFLECTED
REGION

INCIDENT REGION

OBSERVATION
POINT

ψ

ψ_0

r

INCIDENT REGION

$WA \doteq (2-n)\pi$

SHADOW REGION
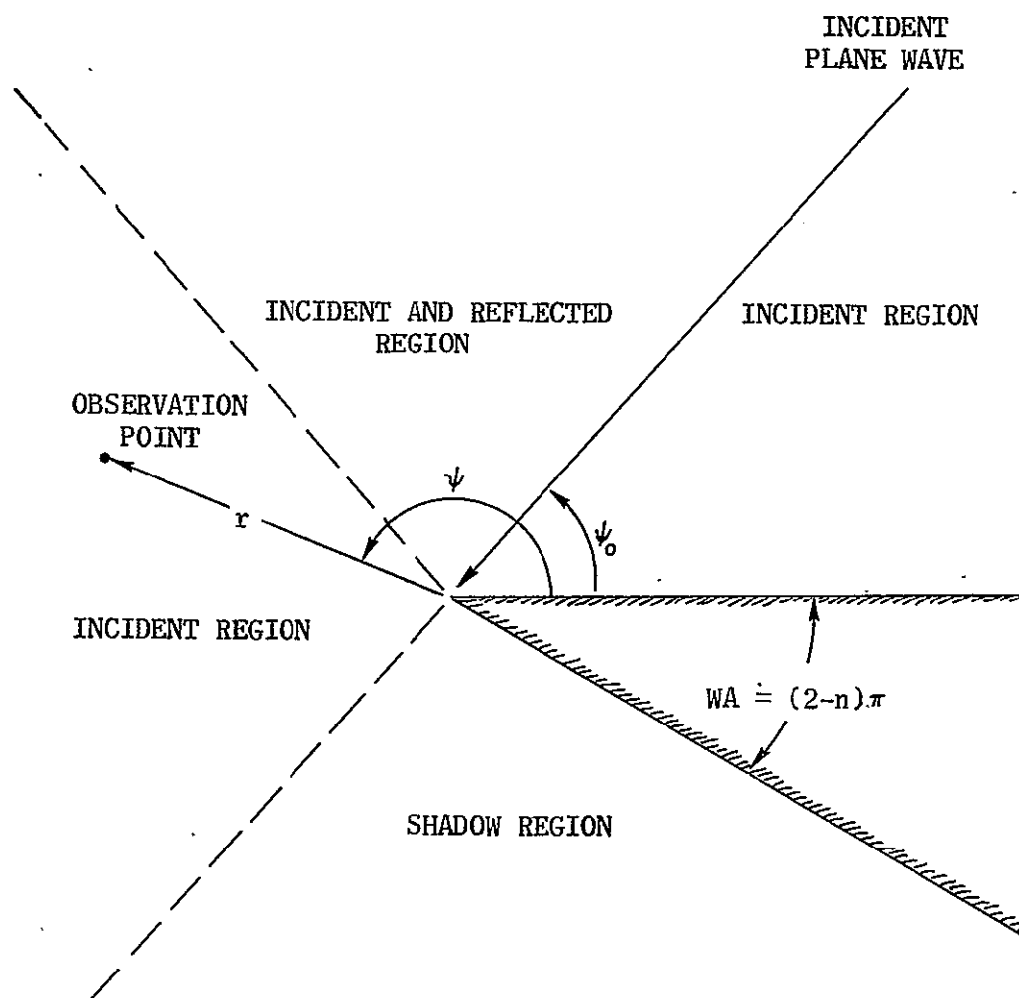
Figure 2.   Geometry for plane wave wedge diffraction with geometrical
optics region.

Incident Geometric Field	±	Reflected Geometric Field	Regions	

$$E_G = e^{jkr\cos(\psi - \psi_0)} \qquad\qquad\qquad \pi - \psi_0 < \psi < \pi + \psi_0 \qquad (5)$$

$$E_G = e^{jkr\cos(\psi - \psi_0)} \pm e^{jkr\cos(\psi + \psi_0)} \qquad 0 < \psi < \pi - \psi_0 \qquad (6)$$

$$E_G = 0 \qquad\qquad\qquad\qquad\qquad \pi + \psi_0 < \psi \qquad (7)$$

The time dependence $e^{j\omega t}$ is used throughout this analysis.

The diffracted wave E_D may be represented as a cylindrical wave radiating from the edge (see Appendix). In fact, at large distances from the edge and in regions removed from shadow boundaries E_D has the radial dependence $e^{-jkr}/\sqrt{r}$. Because of this cylindrical nature, subsequent diffractions of a diffracted wave may be treated as the diffraction of a cylindrical wave by a wedge.

Diffraction By a Pair of Wedges

The process of diffraction by a pair of wedges (parallel-plate waveguide) will be outlined below. Two polarizations which must be distinguished are those corresponding to the TEM and TE_{10} waveguide modes. The two cases of interest are shown in Figure 3. In the TEM mode, the incident plane wave is parallel to the axis of the guide having a polarization perpendicular to the edge of each wedge. The TE_{10} waveguide mode may be represented by two TEM waves which reflect
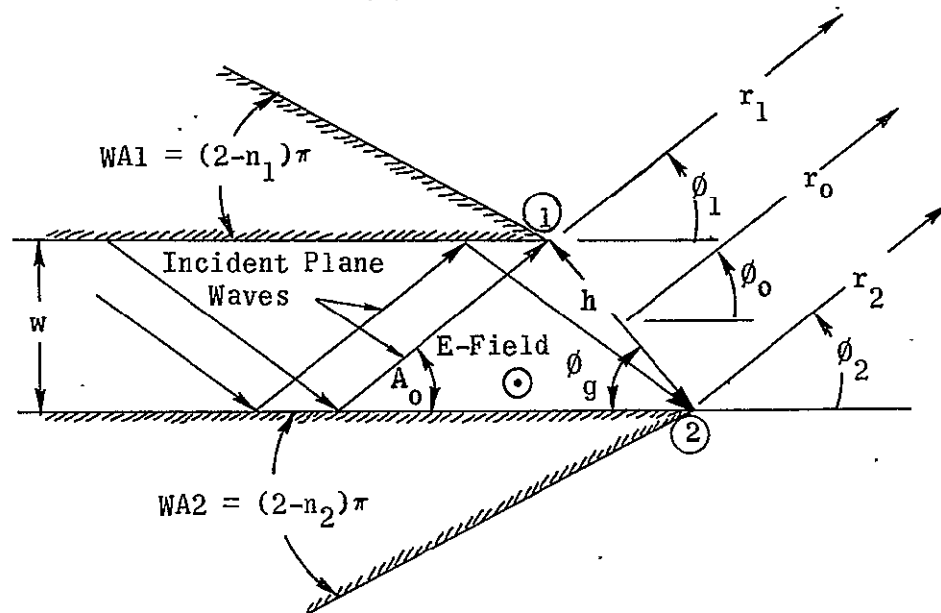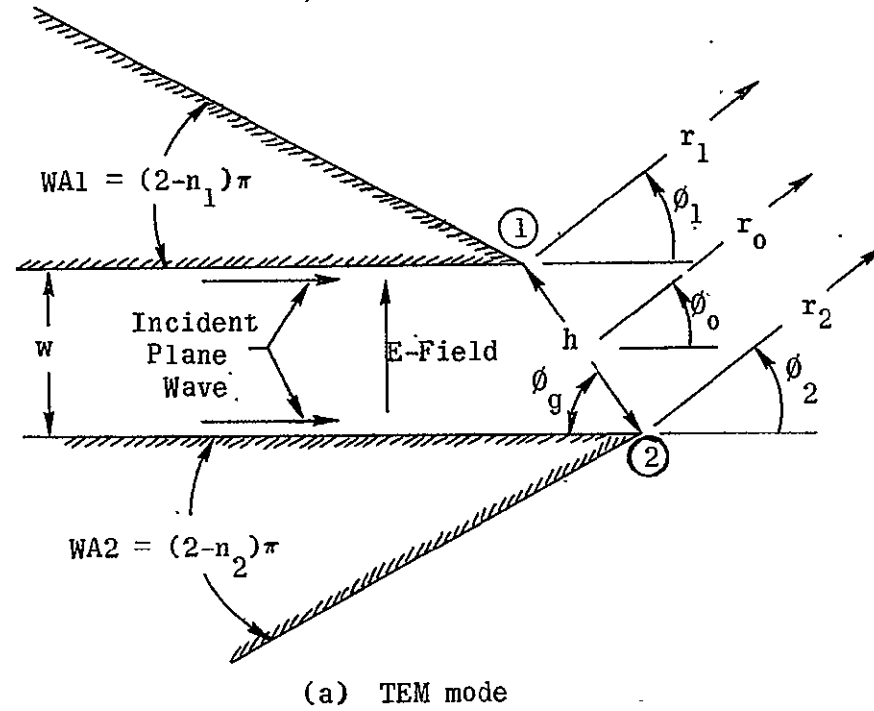
(a) TEM mode

Figure 3.- TEM and TE_{10} modes in a parallel-plate waveguide aperture.

obliquely back and forth between the waveguide walls.[35] Thus, in the TE$_{10}$ mode the incident plane waves have a polarization parallel to the edge of the wedges.

1. TEM Mode

In the TEM mode an incident plane wave propagates parallel to the axis of the guide walls as shown in Figure 3(a). The far-zone singly diffracted fields from wedges 1 and 2 are given by

$$E_{D1}^{(1)}(r_1,\phi_1) = \frac{E_1 e^{-j\left[kr_1 + \pi/4\right]}}{\sqrt{2\pi kr_1}} \left\{ \frac{\frac{1}{n_1} \sin\left(\frac{\pi}{n_1}\right)}{\cos\frac{\pi}{n_1} - \cos\left(\frac{\pi + \phi_1}{n_1}\right)} \right\} \tag{8}$$

$$E_{D2}^{(1)}(r_2,\phi_2) = \frac{E_2 e^{-j\left[kr_2 + \pi/4\right]}}{\sqrt{2\pi kr_2}} \left\{ \frac{\frac{1}{n_2} \sin\left(\frac{\pi}{n_2}\right)}{\cos\frac{\pi}{n_2} - \cos\left(\frac{\pi - \phi_2}{n_2}\right)} \right\} \tag{9}$$

The superscripts denote the order of diffraction. Expressing the phase of the incident waves with respect to edge 1

$$E_1 \doteq E = 1 \tag{10}$$

$$E_2 = Ee^{-jkwcot\phi_g} = e^{-jkwcot\phi_g} \tag{11}$$

Equations 8 and 9 reduce to

$$E_{D1}^{(1)}(r_1,\phi_1) = \frac{e^{-j\left[kr_1 + \pi/4\right]}}{\sqrt{2\pi kr_1}} R_{D1}^{(1)}(\phi_1) \tag{12}$$

$$E_{D2}^{(1)}(r_2,\phi_2) = \frac{e^{-j\left[kr_2 + \pi/4\right]}}{\sqrt{2\pi kr_2}} R_{D2}^{(1)}(\phi_2) \tag{13}$$

where $R_{D1}^{(1)}(\phi_1)$ and $R_{D2}^{(1)}(\phi_2)$ are the singly diffracted rays from wedges 1 and 2 given by

$$R_{D1}^{(1)}(\phi_1) = \frac{\frac{1}{n_1} \sin\left(\frac{\pi}{n_1}\right)}{\cos\frac{\pi}{n_1} - \cos\left(\frac{\pi + \phi_1}{n_1}\right)} \tag{14}$$

$$R_{D2}^{(1)}(\phi_2) = \frac{e^{-jkwcot\phi_g} \frac{1}{n_2} \sin\left(\frac{\pi}{n_2}\right)}{\cos\frac{\pi}{n_2} - \cos\left(\frac{\pi - \phi_2}{n_2}\right)} \tag{15}$$

Applying the far-field approximations

$$\left.\begin{array}{l} r_1 \approx r_o + \frac{h}{2} \cos(\phi_o + \phi_g) \\[2em] r_2 \approx r_o - \frac{h}{2} \cos(\phi_o + \phi_g) \end{array}\right\} \qquad \text{For phase terms} \tag{16}$$

$$r_1 \approx r_2 \approx r_o \qquad\qquad\qquad \text{For amplitude terms} \tag{17}$$

where

$$\phi_1 \approx \phi_2 \approx \phi_o \tag{18}$$

lead to

$$E_{D1}^{(1)}(r_o,\phi_o) = \frac{e^{-j\left\{k\left[r_o+(h/2)\cos(\phi_o+\phi_g)\right]+\pi/4\right\}}}{\sqrt{2\pi k r_o}} R_{D1}^{(1)}(\phi_o) \tag{19}$$

$$E_{D2}^{(1)}(r_o,\phi_o) = \frac{e^{-j\left\{k\left[r_o+(h/2)\cos(\phi_o+\phi_g)\right]+\pi/4\right\}}}{\sqrt{2\pi k r_o}}$$

$$\times R_{D2}^{(1)}(\phi_o)e^{jkh\cos(\phi_o+\phi_g)} \tag{20}$$

The singly diffracted rays may again be diffracted producing doubly diffracted rays and so on to higher orders of diffraction. The singly diffracted ray $R_{D1}^{(1)}$ illuminates edge 2, giving rise to the doubly diffracted ray $R_{D2}^{(2)}$, and $R_{D2}^{(1)}$ causes $R_{D1}^{(2)}$ in a similar manner. Also, some of the singly diffracted rays from edge 1 will be reflected from wedge 2 and appear to radiate from the image of edge 1 giving rise to

$$R_{RFL}^{(1)}(\phi_o) = R_{D1}^{(1)}(-\phi_o) \qquad \phi_g < \phi_o < \frac{\pi}{2} \tag{21}$$

The doubly diffracted ray from edge 2 is given by

$$R_{D2}^{(2)}(\phi_o) = R_{D1G}^{(1)}\left[V_B(h,\pi-\phi_o-\phi_g,n_2) + V_B(h,\pi-\phi_o+\phi_g,n_2)\right] \tag{22}$$

where

$$R_{D1G}^{(1)} = R_{D1}^{(1)}(-\phi_g) \tag{23}$$

and from edge 1 by

$$R_{D1}^{(2)}(\phi_o) = R_{D2G}^{(1)}\left[V_B(h, \phi_o + \phi_g, n_1) + V_B(h, 2\pi + \phi_o - \phi_g, n_1)\right] \tag{24}$$

where

$$R_{D2G}^{(1)} = R_{D2}^{(1)}(\pi - \phi_g) \tag{25}$$

There is an additional doubly diffracted ray by edge 1 from the image source which is given by

$$R_{D1R}^{(2)}(\phi_o) = R_{D1P}^{(1)}\left[V_B\left(2w, \frac{\pi}{2} + \phi_o, \ n_1\right) + V_B\left(2w, \frac{3\pi}{2} + \phi_o, n_1\right)\right] \tag{26}$$

where

$$R_{D1P}^{(1)} = R_{D1}^{(1)}\left(-\frac{\pi}{2}\right) \tag{27}$$

The total diffracted rays from edges 1 and 2, using single-double diffractions, are given by

$$R_{D1}(\phi_o) = R_{D1}^{(1)}(\phi_o) + R_{D1}^{(2)}(\phi_o) + R_{D1R}^{(2)}(\phi_o) \tag{28}$$

$$R_{D2}(\phi_o) = R_{D2}^{(1)}(\phi_o) + R_{D2}^{(2)}(\phi_o) \tag{29}$$

and the reflected ray from wedge 2 by

$$R_{RFL}(\phi_o) = R_{D1}(-\phi_o) \qquad (30)$$

The total diffracted field from the aperture may be expressed as the superposition of the total diffracted rays from edges 1 and 2 plus the total rays from the image source to yield

$$E_D(r_o,\phi_o) = \frac{e^{-j\left\{k\left[r_o+(h/2)\cos(\phi_o+\phi_g)\right]+\pi/4\right\}}}{\sqrt{2\pi k r_o}}\left\{R_{D1}(\phi_o)\right.$$

$$\left. + R_{D2}(\phi_o)e^{jkh\cos(\phi_o+\phi_g)} + R_{D1}(-\phi_o)e^{-j2kw\sin\phi_o}\right\} \qquad (31)$$

Each term in Equation 31 contributes to the radiation pattern only in certain regions as follows:.

$$R_{D1}(\phi_o) \qquad\qquad -\phi_g < \phi_o < \pi - WA1 \qquad (32)$$

$$R_{D2}(\phi_o) \qquad\qquad \pi + WA2 < \phi_o < \pi - \phi_g \qquad (33)$$

$$R_{D1}(-\phi_o) \qquad\qquad +\phi_g < \phi_o < \frac{\pi}{2} \qquad (34)$$

There are subsequent diffractions which result in triple and higher order diffractions from edges 1 and 2. The total higher order diffractions (that is, second and higher order) can be put in a closed form.[6] The total illumination of edge 2 from edge 1 can be expressed as

$$R_{1G} = R_1(-\phi_g) \tag{35}$$

where $R_1(\phi_o)$ is the total diffracted ray from edge 1. Consequently, the total higher order diffractions from edge 2 are given by

$$R_{D2}^{(h)}(\phi_o) = R_{1G}\left[V_B(h, \pi - \phi_o - \phi_g, n_2) + V_B(h, \pi - \phi_o + \phi_g, n_2)\right] \tag{36}$$

and the total ray by

$$R_2(\phi_o) = R_{D2}^{(1)}(\phi_o) + R_{D2}^{(h)}(\phi_o) \tag{37}$$

The total higher order illumination of edge 1 is given by

$$R_{2G} = R_2(\pi - \phi_g) \tag{38}$$

and

$$R_{1P} = R_1\left(-\frac{\pi}{2}\right) \tag{39}$$

Thus the total higher order diffractions from edge 1 are given by

$$R_{D1}^{(h)}(\phi_o) = R_{2G}\left[V_B(h, \phi_o + \phi_g, n_1) + V_B(h, 2\pi + \phi_o - \phi_g, n_1)\right]$$

$$+ R_{1P}\left[V_B\left(2w, \frac{\pi}{2} + \phi_o, n_1\right) + V_B\left(2w, \frac{3\pi}{2} + \phi_o, n_1\right)\right] \tag{40}$$

and the total diffractions by

$$R_1(\phi_o) = R_{D1}^{(1)}(\phi_o) + R_{D1}^{(h)}(\phi_o) \tag{41}$$

The total diffracted field from the aperture can be expressed as the superposition of the total diffracted rays from edges 1 and 2 plus the total reflected ray as given by Equation 31 where $R_{D1}(\phi_o)$, $R_{D2}(\phi_o)$, and $R_{D1}(-\phi_o)$ are replaced by $R_1(\phi_o)$, $R_2(\phi_o)$, and $R_1(-\phi_o)$, respectively.

The total diffracted waves from edges 1 and 2 are given in terms of the unknown illuminating rays R_{1G}, R_{2G}, and R_{1P}. These rays can be determined by the solution of three simultaneous linear equations formed by expressing each unknown ray in terms of Equations 37 or 41.

$$R_{1G} = R_{D1G}^{(1)} + R_{2G}V_{2G}(-\phi_g) + R_{1P}V_{1P}(-\phi_g) \tag{42}$$

$$R_{1P} = R_{D1P}^{(1)} + R_{2G}V_{2G}\left(-\frac{\pi}{2}\right) + R_{1P}V_{1P}\left(-\frac{\pi}{2}\right) \tag{43}$$

$$R_{2G} = R_{D2G}^{(1)} + R_{1G}V_{1G}(\pi - \phi_g) \tag{44}$$

where the quantities V_{1G}, V_{1P}, and V_{2G} are the unit-wave diffractions used in Equations 36 and 40.

2. TE_{10} Mode

The diffraction at the aperture of the parallel-plate waveguide for the TE_{10} mode may be treated in a similar manner as the TEM mode. The TE_{10} mode may be represented by two plane waves reflecting obliquely back and forth between the waveguide walls at an angle

$$A_O = \sin^{-1}\left(\frac{\lambda}{2w}\right) \tag{45}$$

as shown in Figure 3(b). The wave has a polarization parallel to the edges of the wedges which form the waveguide walls. For this mode two cases must be distinguished, as determined by

Case I: $A_O > \phi_g$ (46)

Case II: $A_O \leq \phi_g$ (47)

In Case I edge 2 is not illuminated by the incident plane wave and no singly diffracted ray emanates. For Case II both edges are illuminated by the incident wave; hence, singly diffracted rays emanate from both edges.

Since the polarization is parallel to the edges of the guide for the TE_{10} mode, the negative (-) sign in the diffraction formula is chosen. The singly diffracted ray from edge 1 is obtained from Equation 2 as

$$R_{D1}^{(1)}(\phi_O) = \frac{1}{n_1} \sin\left(\frac{\pi}{n_1}\right) \left\{ \frac{1}{\cos\frac{\pi}{n_1} - \cos\left(\frac{\pi + \phi_O - A_O}{n_1}\right)} \right.$$

$$\left. - \frac{1}{\cos\frac{\pi}{n_1} - \cos\left(\frac{\pi + \phi_O + A_O}{n_1}\right)} \right\} \tag{48}$$

For Case II ($A_O \leq \phi_g$), the singly diffracted ray from edge 2 is given by

$$R_{D2}^{(1)}(\phi_o) = -\frac{1}{n_2} \sin \frac{\pi}{n_2} e^{-jkw\left[\sin A_o + \cot\phi_g \cos A_o\right]}$$

$$\times \left\{ \frac{1}{\cos \frac{\pi}{n_2} - \cos\left(\frac{\pi - \phi_o - A_o}{n_2}\right)} - \frac{1}{\cos \frac{\pi}{n_2} - \cos\left(\frac{\pi - \phi_o + A_o}{n_2}\right)} \right\}$$

$$(49)$$

where the exponential factor and minus sign represent the phase of the incident plane wave at edge 1. The reflected rays are given by

$$R_{RFL}^{(1)}(\phi_o) = -R_{D1}^{(1)}(-\phi_o) \qquad \phi_g < \phi_o < \frac{\pi}{2} \qquad (50)$$

where the preceding minus sign results from the reflection.

Multiple diffractions occur in the same manner as for the TEM mode but with the minus sign chosen in Equations 22, 24, 26, 36, and 40. Thus the total higher order diffracted waves from edges 1 and 2 for the TE_{10} mode are given by

$$R_{D1}^{(h)}(\phi_o) = R_{2G}\left[V_B(h,\phi_o + \phi_g,n_1) - V_B(h,2\pi + \phi_o - \phi_g,n_1)\right]$$

$$- R_{1P}\left[V_B\left(2w,\frac{\pi}{2} + \phi_o,n_1\right) - V_B\left(2w,\frac{3\pi}{2} + \phi_o,n_1\right)\right] \qquad (51)$$

and

$$R_{D2}^{(h)}(\phi_o) = R_{1G}\left[V_B(h,\pi - \phi_o - \phi_g,n_2) - V_B(h,\pi - \phi_o + \phi_g,n_2)\right] \qquad (52)$$

The minus sign preceding R_{1P} results in the same manner as for the reflected rays of Equation 50. The total wave from each edge is obtained by using TE_{10} mode rays in the same equations valid for the TEM mode, that is, Equations 37 and 41-44. The unknown illuminating rays are determined in the same manner as for the TEM mode by using the formulations for $R_{D1}^{(1)}$, $R_{D2}^{(1)}$, $R_{D1}^{(h)}$, and $R_{D2}^{(h)}$ given above for the TE_{10} mode.

CHAPTER II

CREEPING WAVE DIFFRACTION CONCEPT

When a wave is incident upon an opaque object which is large
compared to the wavelength, a shadow is formed. However, some radia-
tion penetrates into the shadow region due to diffracted rays[12-16] as
shown in Figure 4. These rays are produced by incident rays which are
tangent to the surface of the body. Each tangent ray splits at the
point of tangency with one part continuing along the path of the
incident ray and the other traveling along a geodesic on the surface
of the body. At each following point, it splits again with one part
traveling along the geodesic and the other reradiating along a tangent
to the geodesic. From a single incident ray, infinitely many diffracted
rays are produced, one of which is reradiated at each point of the
geodesic. These waves traveling around the opaque body have been
designated as creeping waves introduced first by Franz and Depperman[12]
for the interpretation of scalar diffraction by circular cylinders and
spheres.

The scattered field caused by the creeping wave mechanism for a
plane wave incident on a cylinder is given by

$$E_C(s,\phi) = E_i(Q) \frac{e^{-jk(t+s)}}{\sqrt{s}} \sum_m D_{mh}(Q)D_{mh}(P)e^{-\int_0^t \alpha_{mh}(\rho)ds} \qquad (53)$$

26
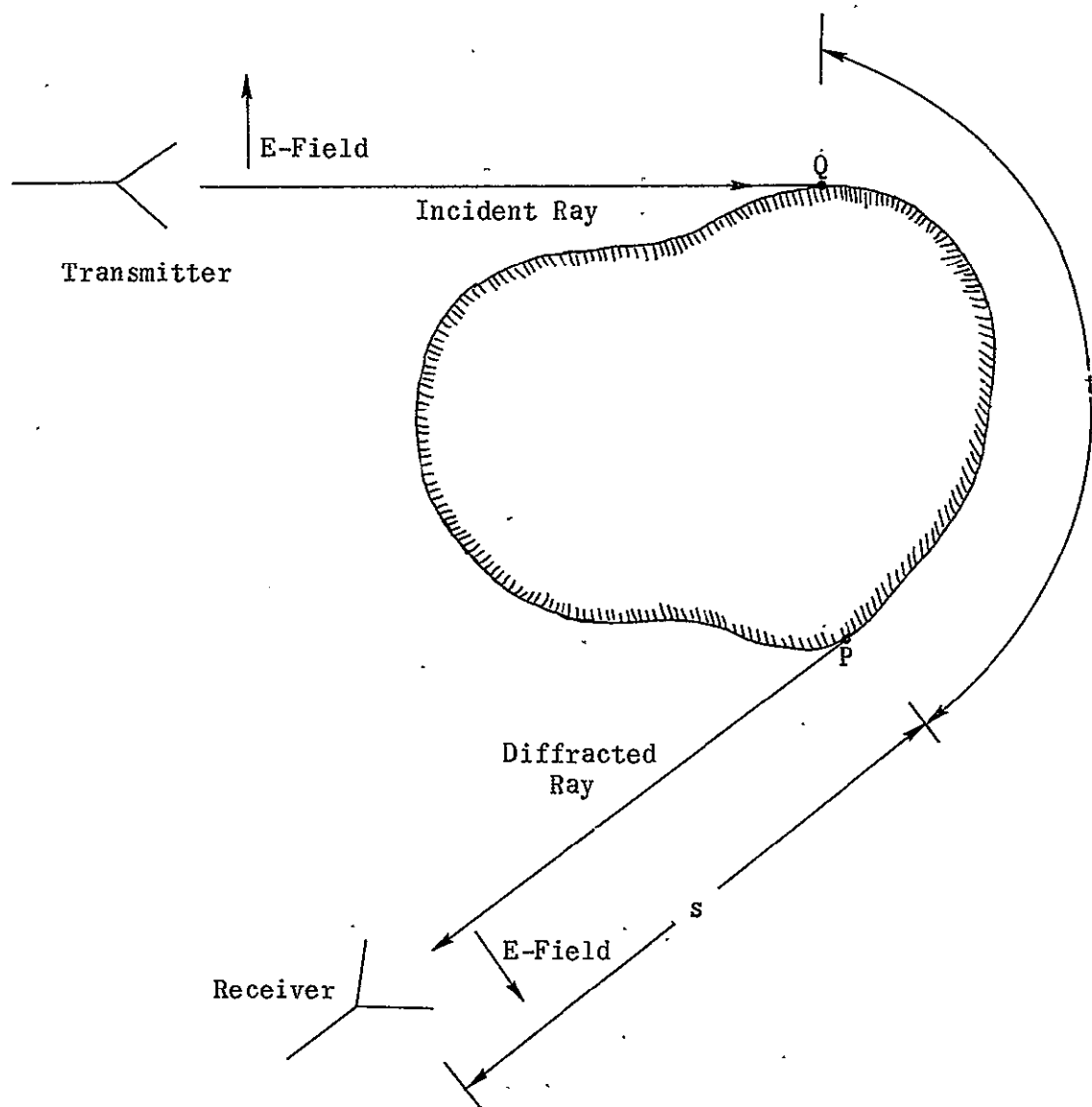
Figure 4. General concept of creeping wave diffraction.

which for a right circular cylinder reduces to

$$E_C(s, \phi) = E_i(Q) \frac{e^{-jk(t+s)}}{\sqrt{s}} \sum_m D_{mh}^2 e^{-\alpha_{mh} t} \qquad (54)$$

since the radius of curvature is constant.

$$D_{mh}^2 = D_{mh}(Q) D_{mh}(P) = \text{Diffraction Coefficients} \approx \frac{e^{-j \pi/12}}{\sqrt{k}} (k\rho)^{1/3} d_m \qquad (55)$$

$$\alpha_{mh} = \text{Attenuation Constant} \approx \frac{1}{2\rho} (k\rho)^{1/3} \left[\frac{3\pi}{4} (4m + N) \right]^{2/3} e^{j \pi/6} \qquad (56)$$

ρ is the radius of curvature of the body

k is the propagation factor

t is the path length along the body

s is the distance from point of detachment to the observation point

P is the point of detachment of the creeping wave

Q is the point of attachment of the creeping wave

For a hard surface (E-field normal to the surface) $d_0 = 1.083$,
$d_1 = 0.555$, $N = 1$, and for a soft surface (E-field parallel to the
surface) $d_0 = 0.645$, $d_1 = 0.490$, $N = 3$. The diffraction coefficients
and attenuation constants are obtained by comparing the asymptotic
series expansion for large $k\rho$ of the canonical boundary-value problem
with Equation 53.[13,14]

Slotted Cylinder Creeping Wave Mechanism

Rays diffracted by the edges of a slotted cylinder shown in Figure 5 which are tangent to the surface of the cylinder behave in a similar manner. At each apex point additional diffracted rays are introduced each of which will travel along the surface of the cylinder and will reradiate tangentially. The creeping wave field for a slotted conducting cylinder can be expressed as

$$E_C(s,\phi) = E_i(Q_1)\frac{e^{-jk(t_1+s_1)}}{\sqrt{s_1}} \sum_m D_{mh}(Q_1)D_{mh}(P_1)e^{-\int_o^{t_1}\alpha_{mh}(\rho)ds}$$

$$+ E_i(Q_2)\frac{e^{-jk(t_2+s_2)}}{\sqrt{s_2}} \sum_n D_{nh}(Q_2)D_{nh}(P_2)e^{-\int_o^{t_2}\alpha_{nh}(\rho)ds} \quad (57)$$

Considering only the lowest-order creeping wave mode, Equation 57 reduces to

$$E_C(s,\phi) = E_i(Q_1)D_{oh}(Q_1)D_{oh}(P_1)\frac{e^{-jk(t_1+s_1)}}{\sqrt{s_1}} e^{-\int_o^{t_1}\alpha_{oh}(\rho)ds}$$

$$+ E_i(Q_2)D_{oh}(Q_2)D_{oh}(P_2)\frac{e^{-jk(t_2+s_2)}}{\sqrt{s_2}} e^{-\int_o^{t_2}\alpha_{oh}(\rho)ds} \quad (58)$$

which for a circular cylinder simplifies to

$$E_C(r,\phi) = E_i(Q_1)D_{oh}^2(Q_1)\frac{e^{-jk(t_1+r)}}{\sqrt{r}} e^{-\alpha_{oh}t_1}$$

$$+ E_i(Q_2)D_{oh}^2(Q_2)\frac{e^{-jk(t_2+r)}}{\sqrt{r}} e^{-\alpha_{oh}t_2} \quad (59)$$

since the local radius of curvature is the same at P_1, P_2, Q_1, and Q_2.
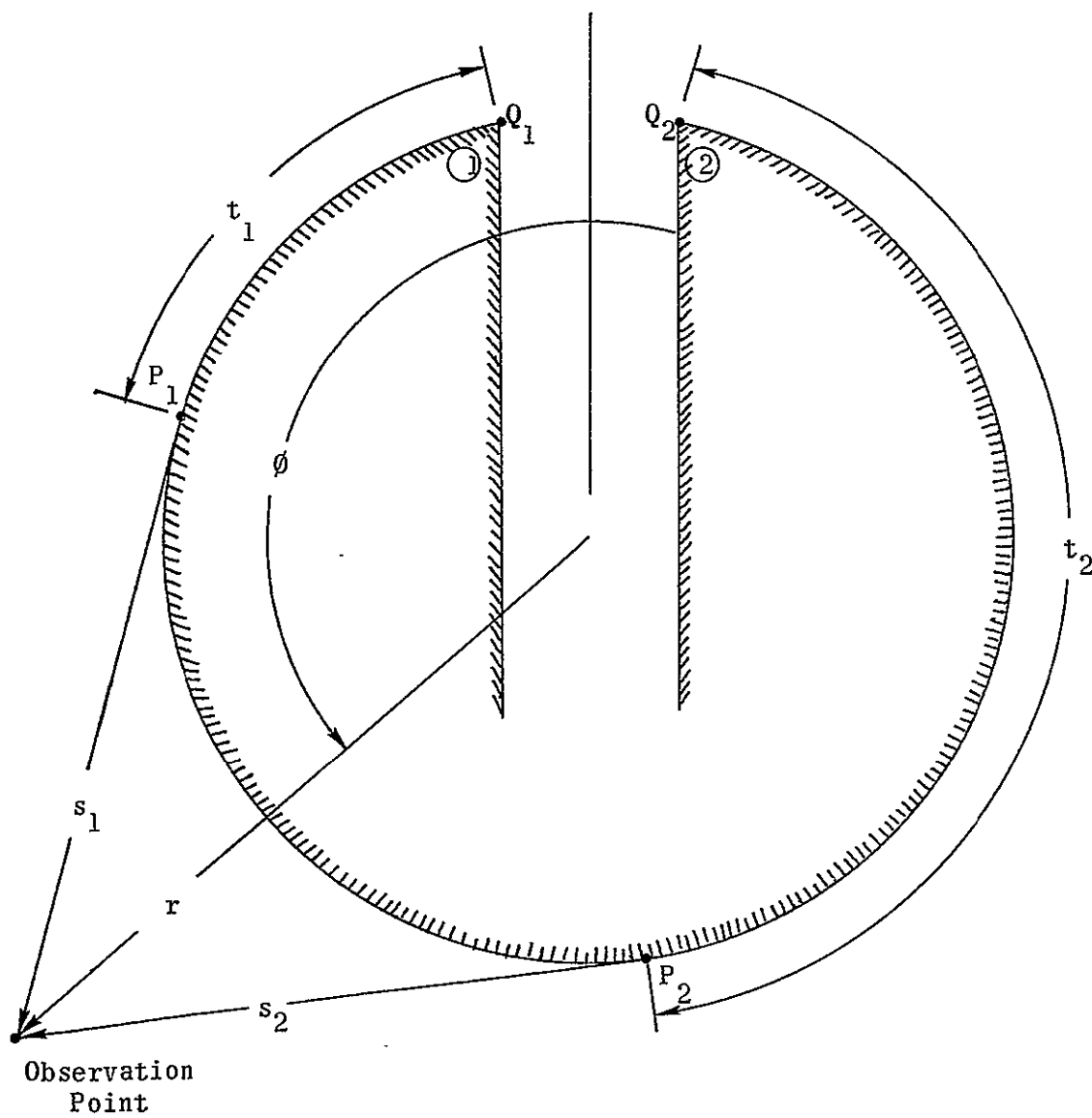
Figure 5. Slotted cylinder creeping wave fields.

To assure continuity of the fields across the boundary between the "lit" and "shadow" regions, the far-field edge diffracted fields are to be equated to the creeping wave fields at the shadow boundary. The angular variation of the wedge-diffracted fields along the shadow boundaries is given by

$$R_A = \frac{\sqrt{r}}{e^{-jkr}} \, E_D\left[r, \; + \left(\frac{\pi}{2} + \zeta\right)\right] \tag{60}$$

$$R_B = \frac{\sqrt{r}}{e^{-jkr}} \, E_D\left[r, \; - \left(\frac{\pi}{2} + \zeta\right)\right] \tag{61}$$

for the geometry of Figure 6. In other words, the angular variation of the wedge-diffracted fields along the shadow boundary will be used as the initial value of the angular variations of the creeping waves. Thus, R_A and R_B will serve as the coupling mechanisms between the wedge-diffracted and creeping waves which assure field continuity along the shadow boundaries. The creeping wave field for a circular cylinder can then be expressed as

$$E_C(r,\phi) = R_A \frac{e^{-jk(t_1 + r)}}{\sqrt{r}} \, e^{-\alpha_{oh}t_1} + R_B \frac{e^{-jk(t_2 + r)}}{\sqrt{r}} \, e^{-\alpha_{oh}t_2} \tag{62}$$

where

$$R_A = E_i(Q_1)D_{oh}^2(Q_1) = \frac{\sqrt{r}}{e^{-jkr}} \, E_D\left[r, \; + \left(\frac{\pi}{2} + \zeta\right)\right] \tag{63}$$
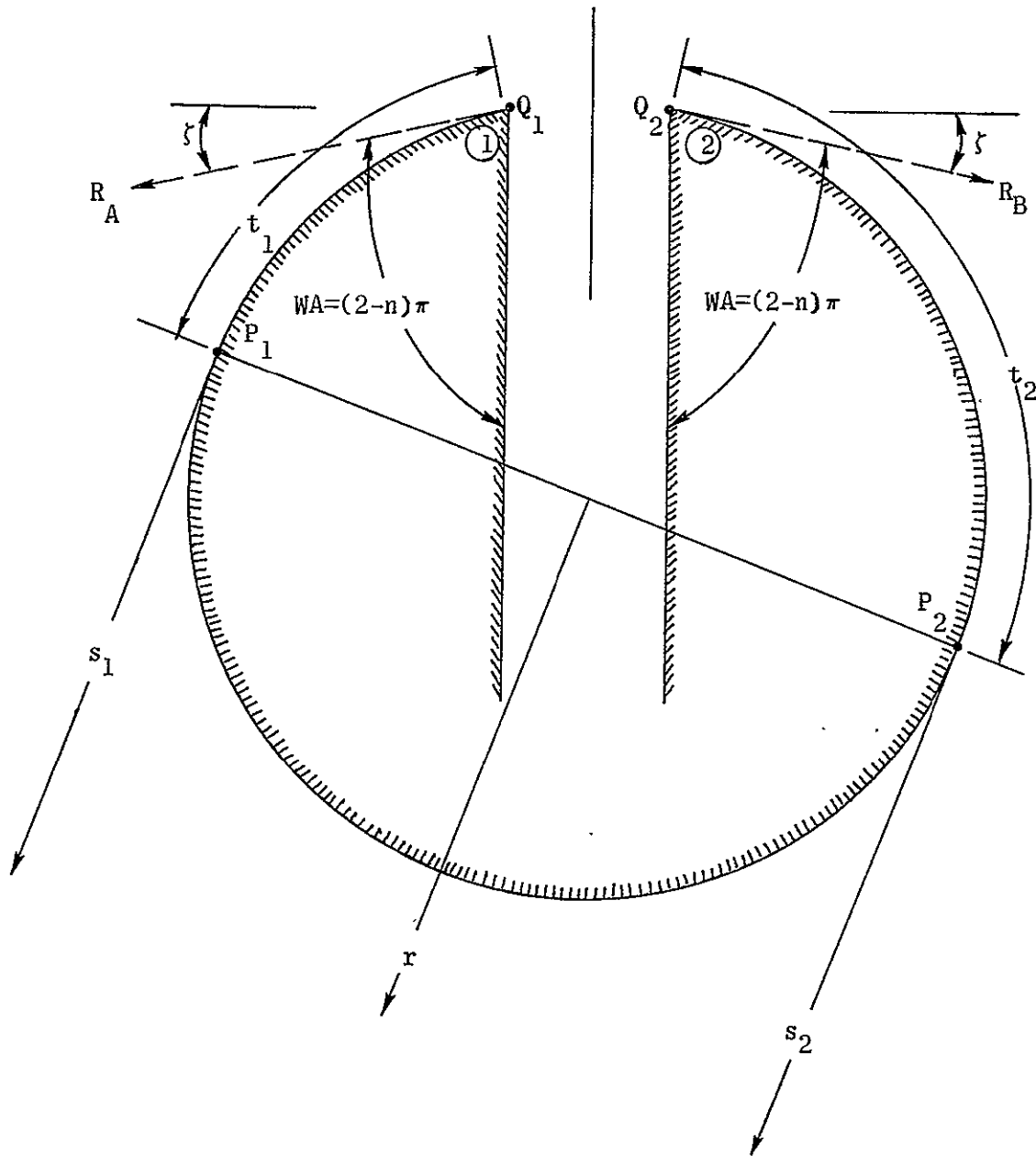
Figure 6. Far-zone creeping wave field coordinates.

$$R_B = E_i(Q_2)D_{oh}^2(Q_2) = \frac{\sqrt{r}}{e^{-jkr}} E_D\left[r, -\left(\frac{\pi}{2} + \zeta\right)\right] \tag{64}$$

For a noncircular cylinder the diffraction coefficient D_{oh} is a function of the radius of curvature. Therefore the creeping wave field given by Equation 62 must be multiplied by $D_{oh}(P)/D_{oh}(Q)$ giving

$$E_C(s,\phi) = R_A \frac{D_{oh}(P_1)}{D_{oh}(Q_1)} \frac{e^{-jk(t_1+s_1)}}{\sqrt{s_1}} e^{-\int_o^{t_1} \alpha_{oh}(\rho)ds}$$

$$+ R_B \frac{D_{oh}(P_2)}{D_{oh}(Q_2)} \frac{e^{-jk(t_2+s_2)}}{\sqrt{s_2}} e^{-\int_o^{t_2} \alpha_{oh}(\rho)ds} \tag{65}$$

The wedge approximation of the parallel-plate-cylinder geometry does alter the physical boundaries of the antenna structure and the diffraction mechanism of the fields especially in the penumbra region. For the wedge approximation, the fields in the $\phi = \pm(\pi/2 + \zeta)$ directions travel along the boundaries of the wedges. However, in the actual antenna structure some of the energy is trapped on the surface of the cylinder and travels along the curved surface reradiating in a tangential direction. Thus the wedge-diffracted and creeping wave fields in the transition region (penumbra) will not satisfy the field boundary conditions. However, computations carried out using such a model compare favorably with existing boundary-value solutions and experimental data. Therefore, such a model would be a valid approximation of the structure as far as the diffraction mechanism of the fields is concerned and Equations 60 and 61 would serve as the coupling mechanisms between wedge-diffracted and creeping wave fields.

CHAPTER III

CIRCULAR CYLINDER RADIATION

The wedge diffraction and creeping wave techniques previously
outlined will first be applied for the calculation of the equatorial
radiation patterns of axial and circumferential slots on circular
conducting cylinders of infinite length. Boundary-value solutions
for slots on circular cylinders with common feeds exist and will be
used for comparison. Once the method is verified, it will be employed
for pattern calculations of slots whose field distribution is such that
modal solutions do not exist and to bodies whose geometric shape does
not conform to a coordinate system where the wave equation is separable.
In addition, the elevation plane pattern for finite length cylinders
will be analyzed. It should be pointed out that no boundary-value
solutions for finite length cylinders exist, and experimental results
will be used for comparison. The diffraction contributions from the
edges of the cylinder and the effect of the finite width aperture to
the overall pattern will be observed. Pattern calculations for more
complex geometries such as an elliptical cylinder will be carried out
in the following chapter.

Equatorial Plane Pattern of Axial Slots Operating in the TEM Mode

The two-dimensional diffraction geometry for an axial slot mounted
on a circular cylinder and operating in the TEM mode is shown in

34

Figure 7. The junctions formed by the walls of the parallel-plate waveguide and the planes tangent to the surface of the cylinder at the edge points are represented by a pair of infinite wedges of finite included angle $WA = (2 - n)\pi$. Two regions, "lit" and "shadow," are formed by the imaginary sides of the finite wedges as shown in Figure 7.

For $\phi_g = 90°$ of Figure 3(a), $R_{D1}(-\phi_o) = 0$, $R_{D1R}(\phi_o) = 0$, $h = w$, $n_1 = n_2 = n$ and Equation 31 for the wedge-diffracted field reduces to

$$E_D(r_o, \phi_o) = \frac{e^{-j\left\{k\left[r_o - (w/2)\sin\phi\right] + \pi/4\right\}}}{\sqrt{2\pi k r_o}} \left\{R_1(\phi_o) + R_2(\phi_o)e^{-jkw\sin\phi_o}\right\}$$

(66)

A shift of coordinates from the aperture to the center of the cylinder is convenient, so that common coordinates will be used for wedge-diffracted and creeping wave fields. Assuming the far-zone approximations

$$r_o \approx r - a \cos\phi \cos\beta \qquad \text{For phase terms} \qquad (67)$$

$$r_o \approx r \qquad \text{For amplitude terms} \qquad (68)$$

$$\phi_o \approx \phi \qquad (69)$$

the total wedge-diffracted field is expressed as

$$E_D(r,\phi) = \frac{1}{\sqrt{2\pi k}} \frac{e^{-jkr}}{\sqrt{r}} e^{j\left\{k\left[(w/2)\sin\phi + a\cos\phi\cos\beta\right] - \pi/4\right\}} \left\{R_1(\phi)\right.$$

$$\left. + R_2(\phi)e^{-jkw\sin\phi}\right\}$$

(70)
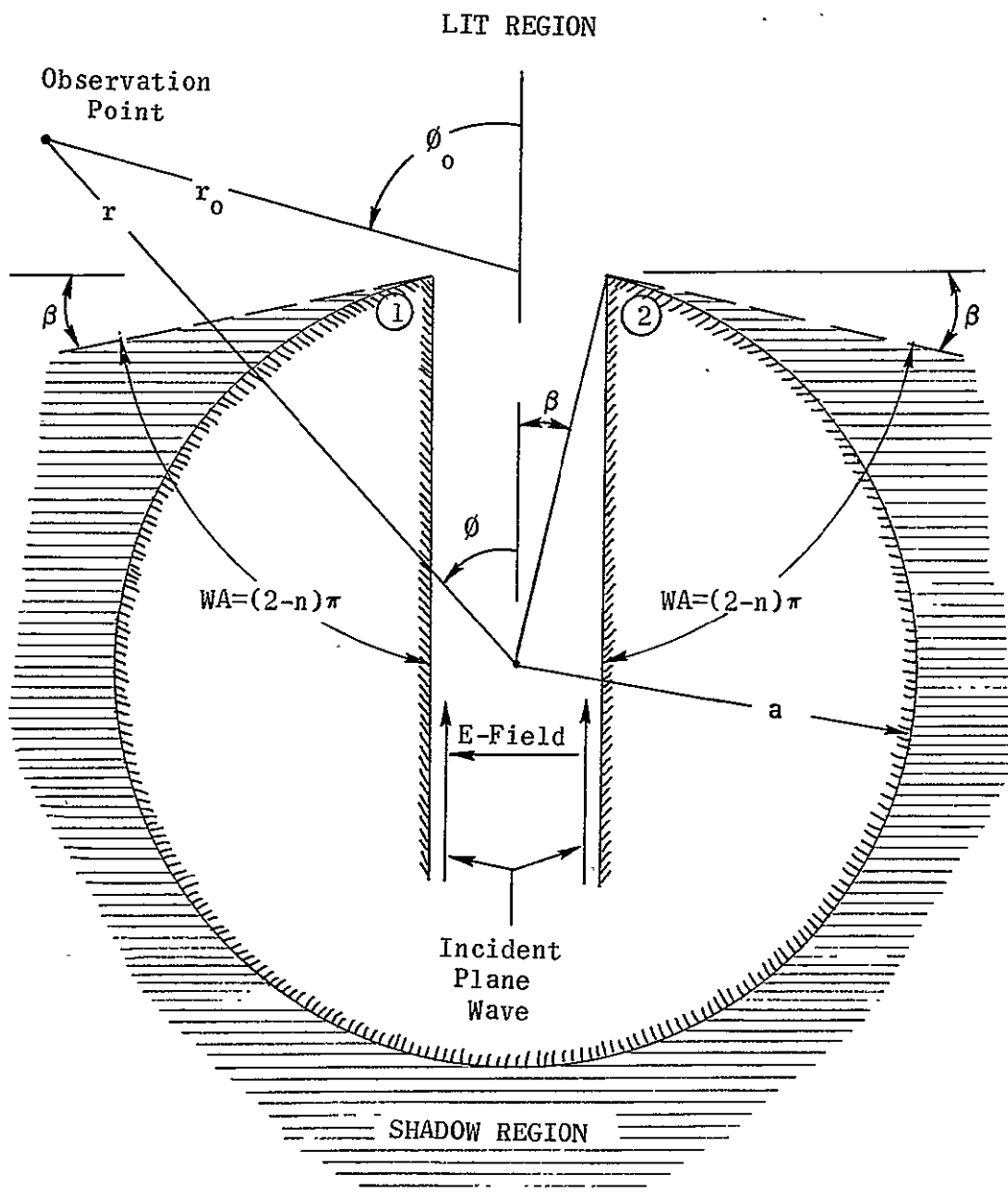
Figure 7. Lit and shadow regions for circular cylinder.

The creeping wave contribution as expressed by Equation 62 is given by

$$E_C(r,\phi) = R_A^- \frac{e^{-jkr}}{\sqrt{r}} e^{-t_1(\alpha_{oh}+jk)} + R_B \frac{e^{-jkr}}{\sqrt{r}} e^{-t_2(\alpha_{oh}+jk)} \qquad (71)$$

The wedge-diffracted and creeping wave fields, suppressing the $e^{-jkr}/\sqrt{r}$ factor, are given by

$$E_D(\phi) = \frac{1}{\sqrt{2\pi k}} e^{j\left\{ k\left[(w/2)\sin\phi+a\cos\phi\cos\beta\right] - \pi/4 \right\}} \left\{ R_1(\phi) + R_2(\phi)e^{-jkw\sin\phi} \right\}$$

$$(72)$$

and

$$E_C(\phi) = R_A e^{-t_1(\alpha_{oh}+jk)} + R_B e^{-t_2(\alpha_{oh}+jk)} \qquad (73)$$

In general, the total field is equal to the sum of the two fields

$$E_T(\phi) = E_D(\phi) + E_C(\phi) \qquad (74)$$

However, wedge-diffracted and creeping wave fields do not exist in all regions. To find the total field in each region, the appropriate wedge-diffracted and creeping wave fields must be considered, as they are tabulated in Table 1.

Radiation patterns computed using the boundary-value solution given by Wait[3] and the fields from Table 1 in their respective regions for the diffracted-field solution are shown on Plates I, II. It should be noted that the second and higher order diffractions are approximated by

TABLE 1.   WEDGE-DIFFRACTED AND CREEPING WAVE FIELDS FOR THE EQUATORIAL PLANE PATTERN

OF A CIRCULAR CYLINDER IN THE DIFFERENT REGIONS

Regions	Wedge-diffracted field $E_D(\phi)$	Creeping wave field $E_C(\phi)$	t_1	t_2
Region I $0 < \phi \le \frac{\pi}{2} - \beta$	$\dfrac{e^{j\left[k((w/2)\sin\phi+a\cos\phi\cos\beta) - \pi/4\right]}}{\sqrt{2\pi k}}\left\{R_1 + R_2 e^{-jkw\sin\phi}\right\}$	$R_A e^{-t_1(a_{oh}+jk)} + R_B e^{-t_2(a_{oh}+jk)}$	$a\left(\phi + \frac{3\pi}{2} - \beta\right)$	$a\left(-\phi + \frac{3\pi}{2} - \beta\right)$
Region II $\frac{\pi}{2} - \beta < \phi \le \frac{\pi}{2}$	$\dfrac{e^{j\left[k((w/2)\sin\phi+a\cos\phi\cos\beta) - \pi/4\right]}}{\sqrt{2\pi k}}\left\{R_1 + R_2 e^{-jkw\sin\phi}\right\}$	$R_B e^{-t_2(a_{oh}+jk)}$		$a\left(-\phi + \frac{3\pi}{2} - \beta\right)$
Region III $\frac{\pi}{2} < \phi \le \frac{\pi}{2} + \beta$	$\dfrac{e^{j\left[k((w/2)\sin\phi+a\cos\phi\cos\beta) - \pi/4\right]}}{\sqrt{2\pi k}}\left\{R_1\right\}$	$R_B e^{-t_2(a_{oh}+jk)}$		$a\left(-\phi + \frac{3\pi}{2} - \beta\right)$
Region IV $\frac{\pi}{2} + \beta < \phi \le \pi$	0	$R_A e^{-t_1(a_{oh}+jk)} + R_B e^{-t_2(a_{oh}+jk)}$	$a\left(\phi - \frac{\pi}{2} - \beta\right)$	$a\left(-\phi + \frac{3\pi}{2} - \beta\right)$
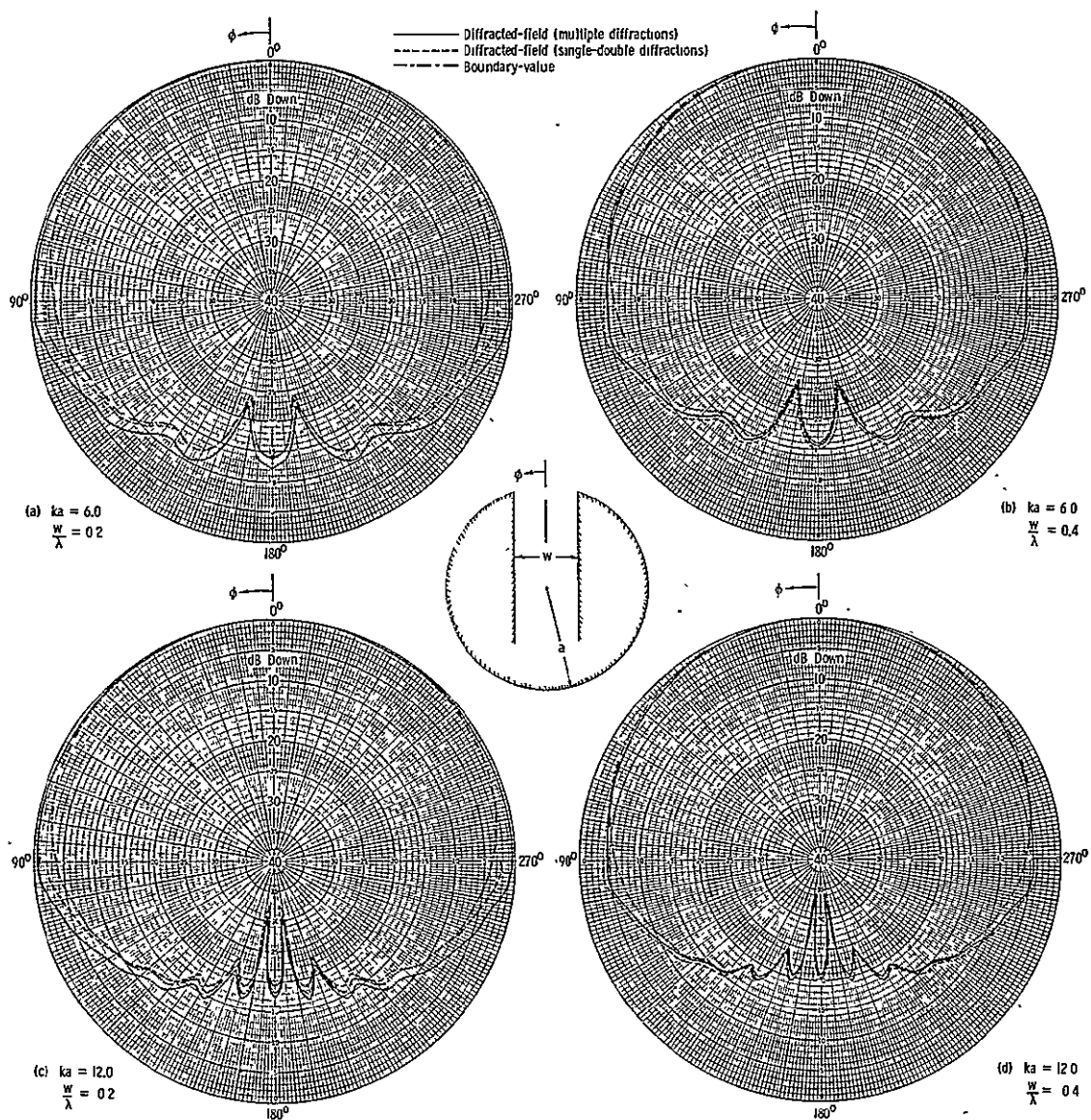
Plate I. Radiation patterns of axial infinite slot on smaller circular conducting cylinder using finite wedges (TEM mode).
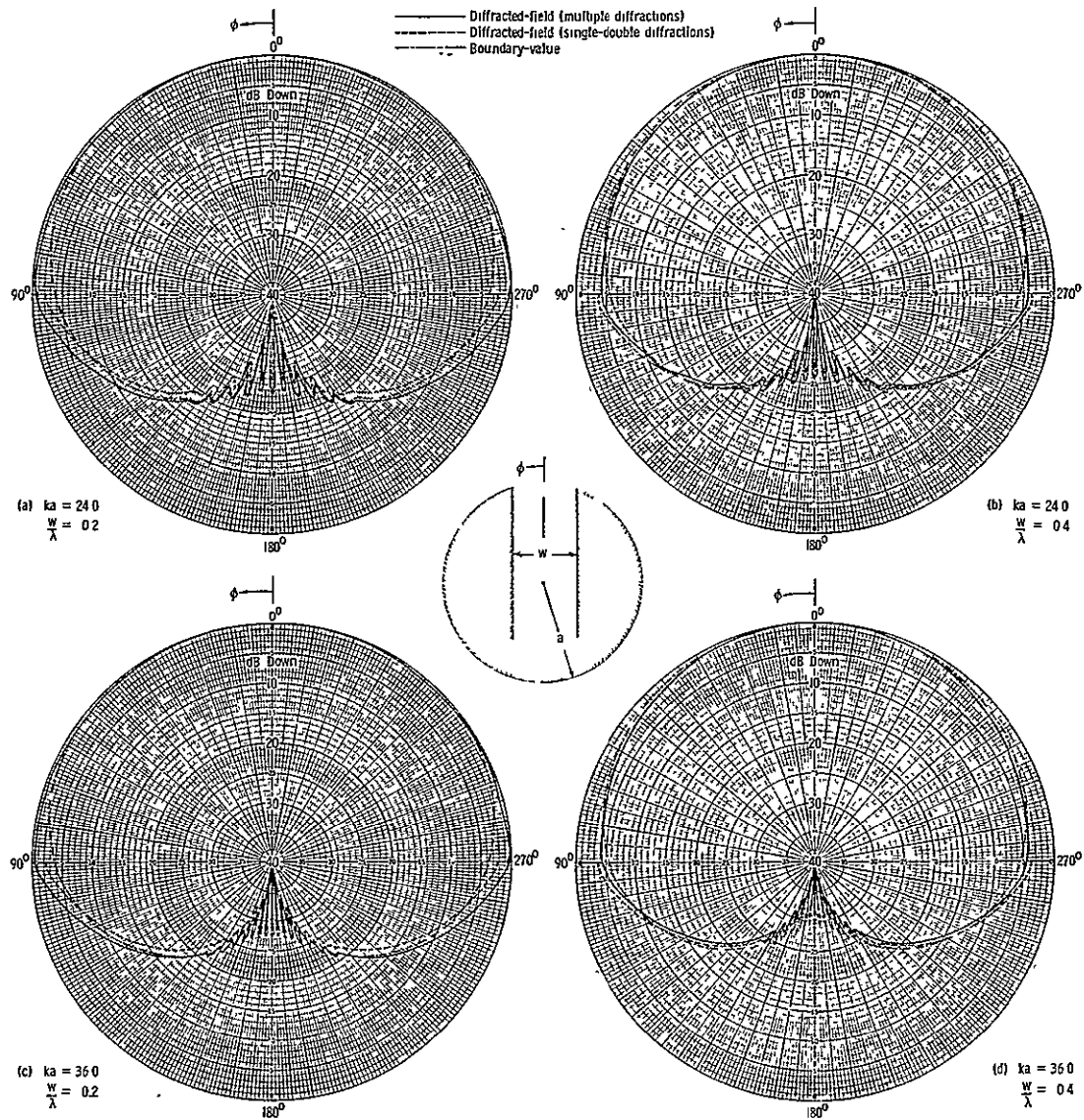
Plate II. Radiation patterns of axial infinite slot on larger circular conducting cylinder using finite wedges (TEM mode).

wedge diffractions resulting from uniform cylindrical waves. Diffracted

waves will resemble cylindrical waves if they are observed sufficiently

far away from any shadow boundary that results from their source. The

double-diffracted waves can be adequately treated as those of uniform

cylindrical waves for guide widths down to about $\lambda/5$. However, triple

and higher order diffractions are not very accurate when $\phi_g = 90^\circ$

since they are viewed at the shadow boundary formed by their source[32]

and the solution is more accurate for wider slots.

The solutions which consider only first and second order diffrac-

tions have a discontinuity in the $\phi = \pm 90^\circ$ directions because higher

order diffractions are neglected. The discontinuity and variation from

the boundary-value solution in the $\phi = \pm 90^\circ$ is greater for smaller

guide widths. The solution which takes into account higher order

diffractions eliminates the discontinuity, but it is not very accurate

in the geometrical shadow boundary region (penumbra) since the assump-

tion of uniform cylindrical waves is not satisfied for triple and

higher order diffractions.

This analysis is more accurate for large ka cylinders since the

decaying exponents of the surface waves are derived from asymptotic

series for large ka. Using this approach, the computations for large

ka cylinders do not require any additional details from those of small

ka. In contrast, the boundary-value solution computations for large ka

cylinders are not very convenient since Bessel functions of large order

and argument are not readily available. Also, the convergence of the

radiation pattern function becomes poor for large ka, and higher order

terms must be included (about 2ka terms). From an economic point of

view, large ka value computations using the boundary-value solution require considerably more computer time compared to the corresponding diffracted field solution (about a factor of 50) since higher order terms must be included for convergence.

As the values of ka increase, the field in the "shadow" region $-(\pi/2 + \beta) > \phi > (\pi/2 + \beta)$ decreases and the ripples start to appear at larger angles. It is noted that the period of the ripples is approximately $(180/ka)$ degrees. A field plot (voltage versus angle) for the ka = 12, $w/\lambda = 0.2$ cylinder is shown in Figure 8. The variations between the boundary-value and wedge-diffracted solutions and the field discontinuity along the $\phi = \pm 90^\circ$ directions are more noticeable on a linear scale. The agreement would be significantly improved for larger cylinders with wider plate separations as shown for the ka = 36, $w/\lambda = 0.4$ cylinder in Figure 9.

Up to now, the parallel-plate-cylinder geometry has been approximated by a set of wedges of finite included angle $(n \neq 2)$ each formed by a wall of the parallel-plate and a tangent plane to the cylinder surface at the edge point. For the far field, it would be the presence of the conducting wall for the wedge geometry of Figure 3 that would force the field to be zero at $\phi = \pi - WA$. However, there is no such conducting wall in the far field of the geometry of Figure 6 and it is only the edge that needs to be considered. Sommerfeld[17] points out that patterns on precise diffraction photographs exhibit almost no dependence on the material and shape of the diffraction edge, and a glass surface with radius of curvature of several meters yields essentially the same diffraction fringes as the edge of a razor. It is then suggested that
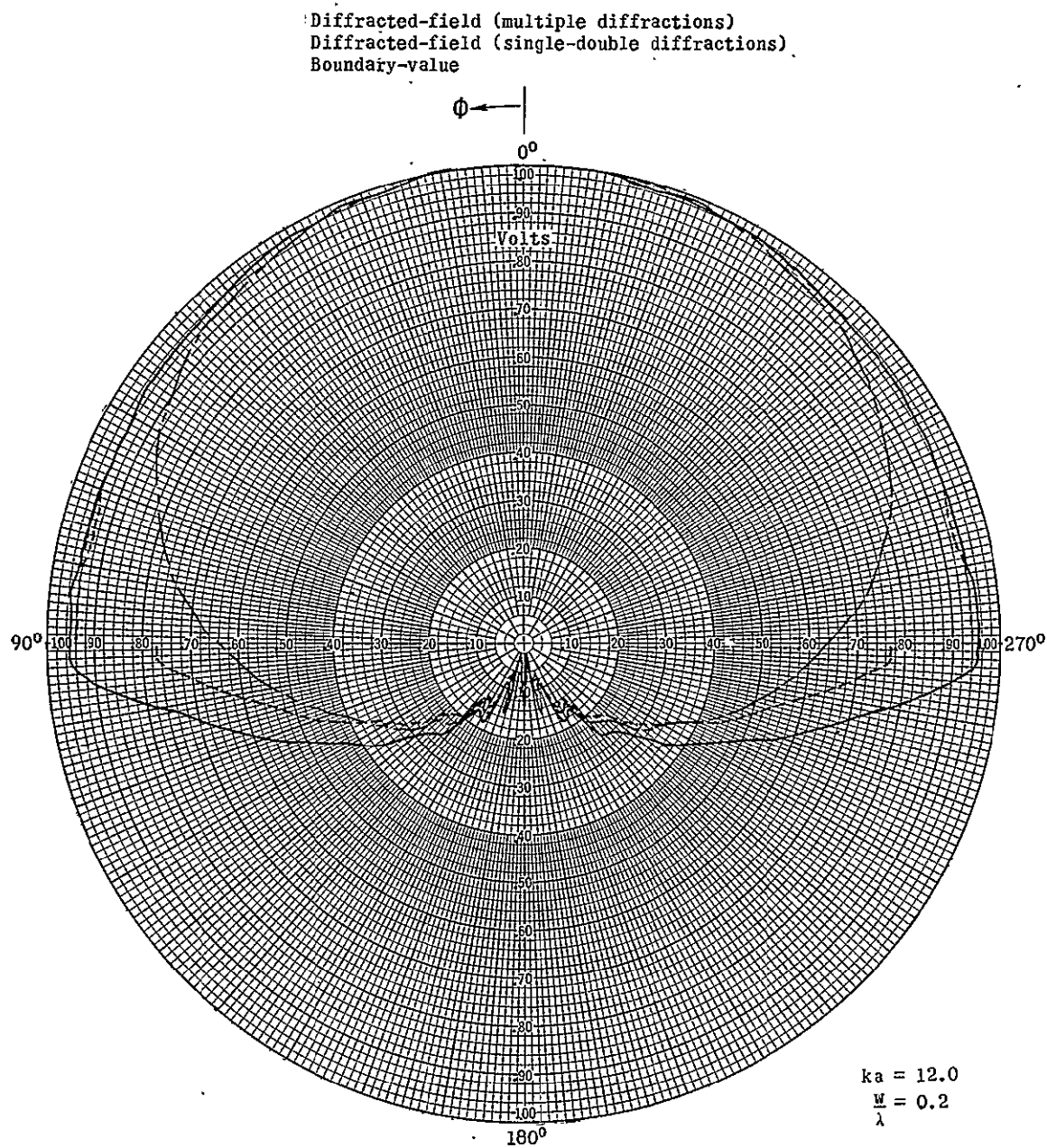
Figure 8. Field plot of axial infinite slot on circular conducting
cylinder (ka = 12,   w/λ = 0.2) using finite wedges (TEM mode).
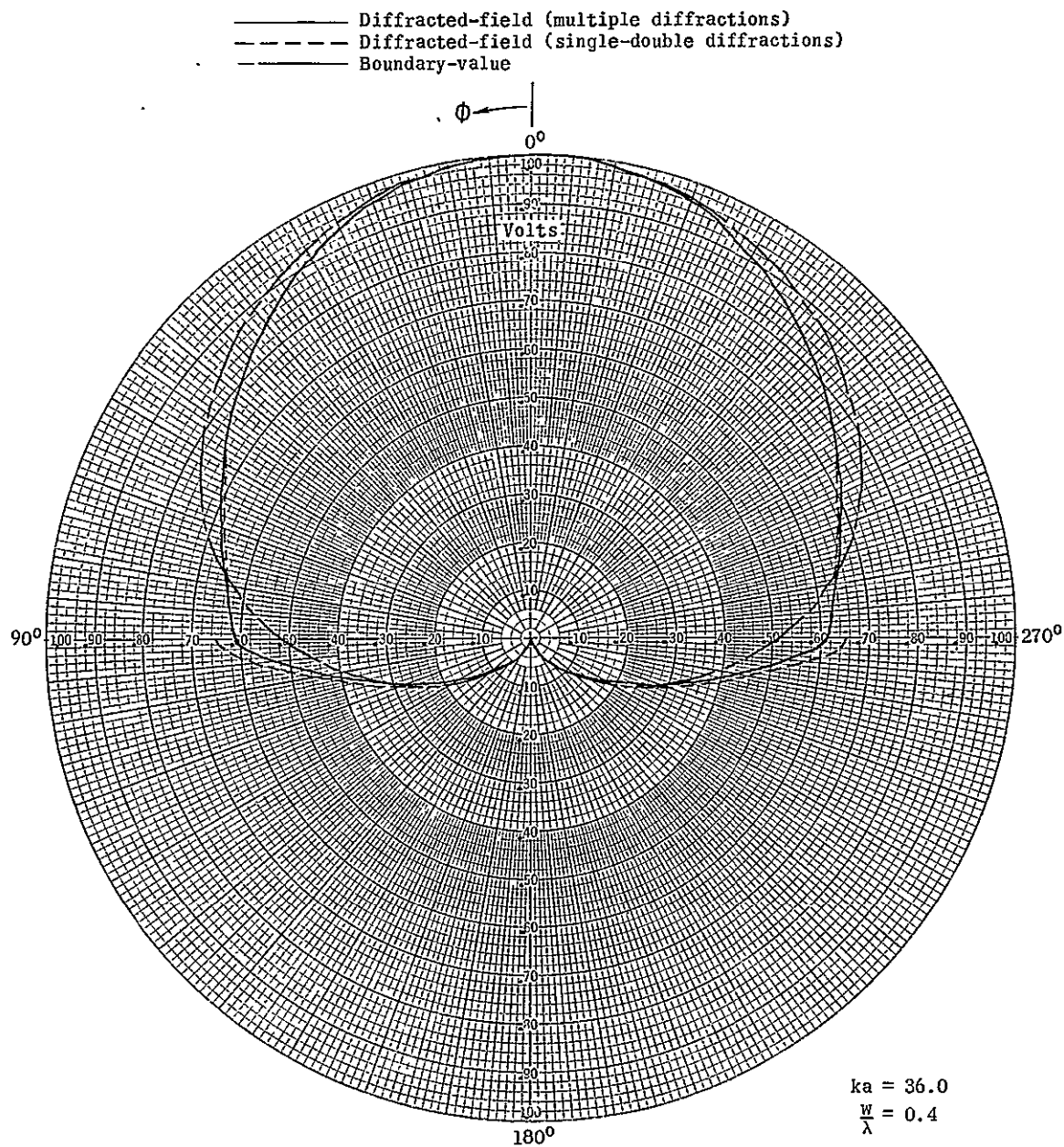
Figure 9. Field plot of axial infinite slot on circular conducting cylinder (ka = 36, w/λ = 0.4) using finite wedges (TEM mode).

another possible approximation of the parallel-plate-cylinder geometry
will be a half-plane (wedge with $n = 2$) instead of a finite wedge
($n \neq 2$). This approximation becomes necessary for the TE_{10} mode because
the wedge-diffracted field along the boundary separating the "lit" and
"shadow" regions for the finite wedge approximation will be zero. Thus,
there will be no creeping waves traveling around the cylinder surface
for the TE_{10} mode and no fields in the "shadow" region. Since this is
not true, the half-plane approximation becomes necessary.

However, to verify the validity of the approximations, finite
wedge ($n \neq 2$) and half-plane ($n = 2$), both models will be used for the
computation of patterns for TEM and TE_{10} mode slots and compared with
boundary-value solutions and experimental results.

It was found, by comparison, that another approximation for the
TEM mode slot on a circular cylinder was to replace the edge 1 geometry
by a half-plane ($n = 2$) for the first order diffraction and by a finite
wedge ($n \neq 2$) for second and higher order diffractions for the 0°-180°
pattern measured in the counterclockwise direction. The edge 2 geometry
was replaced by a finite wedge for all orders of diffraction. For the
180°-360° pattern, the approximations of edge 1 geometry are valid for
edge 2 and vice-versa.

The computed results using the above approximations are shown on
Plates III, IV where they are compared with the boundary-value solution.
It is seen that the above approximations result in better accuracies for
smaller guide widths around the penumbra region than the finite wedge
approximation used previously. However, the finite wedge approximation
gives better results in the "lit" region as it should since the fields
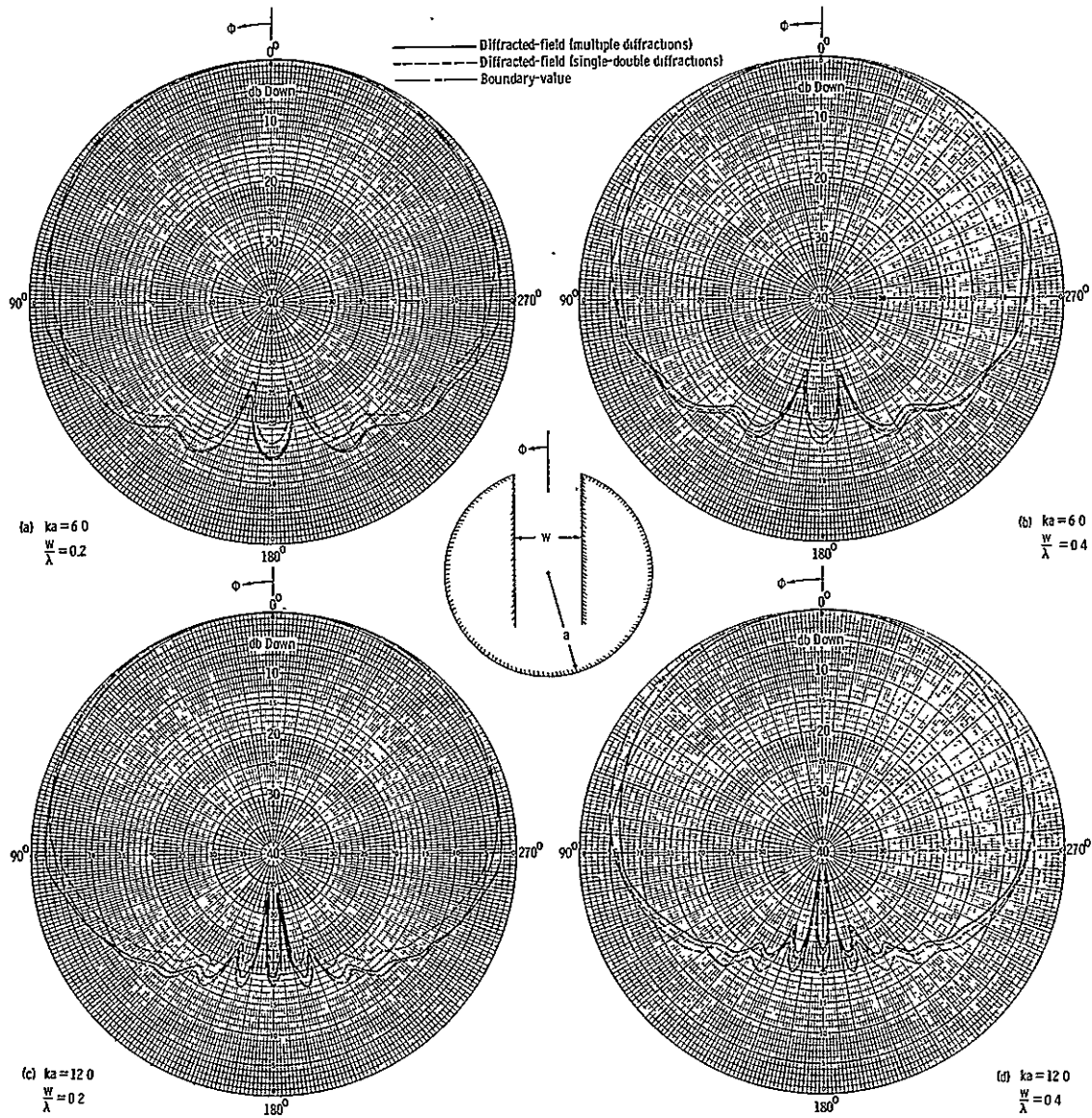
Plate III. Radiation patterns of axial infinite slot on smaller circular conducting cylinder using half-plane and finite wedges (TEM mode).

47
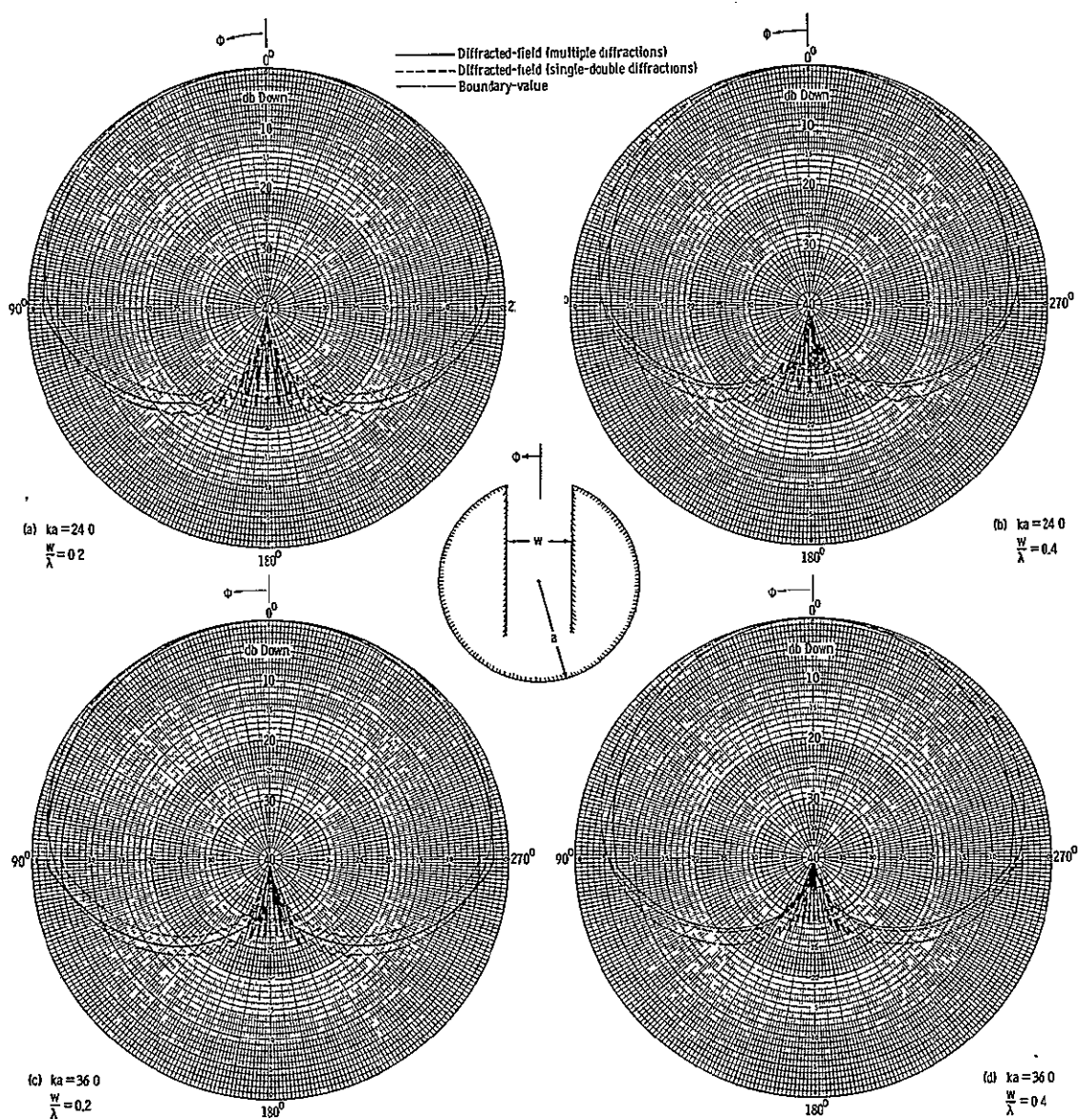
Plate IV. Radiation patterns of axial infinite slot on larger circular
conducting cylinder using half-plane and finite wedges (TEM mode).

in the "lit" region are more strongly dependent on the geometry of the edge of the wedge, while the far fields in the penumbra region would be dependent on the fields on the walls of the wedge. It should then be concluded that both approximations are valid and a combination of the wedge approximations dependent on the location of the observation point would yield optimum results. As a first order of approximation, either one of the suggested models may be used. A field plot for the $ka = 12$, $w/\lambda = 0.2$ cylinder is shown in Figure 10. The accuracy of the above approximation of the penumbra region is better seen in this plot when compared with the one in Figure 8.

As was pointed out earlier, many models for the parallel-plate-cylinder geometry would give good results as a first order of approximation. Another suggested model for the parallel-plate-cylinder geometry would be a thin-walled waveguide ($n = 2$ for all orders of diffractions). Computed results using such a model are shown in Figure 11. A reasonable agreement between the boundary-value and diffracted solutions is indicated.

Sometimes it may be desirable to have the maximum radiation oriented at a given angle other than the zero degree direction described previously. One way of accomplishing this would be to have the feed of the waveguide mounted in a slanted position.

TEM mode propagation along the parallel-plate is assumed but the aperture field distribution will not be uniform in this case. Propagation of this mode in a guide mounted on a cylinder in a slanted position has no boundary-value solution. However, the technique of diffracted fields described previously can be used to obtain the radiation pattern.

Figure 10. Field plot of axial infinite slot on circular conducting
cylinder using half-plane and finite wedges (TEM mode).
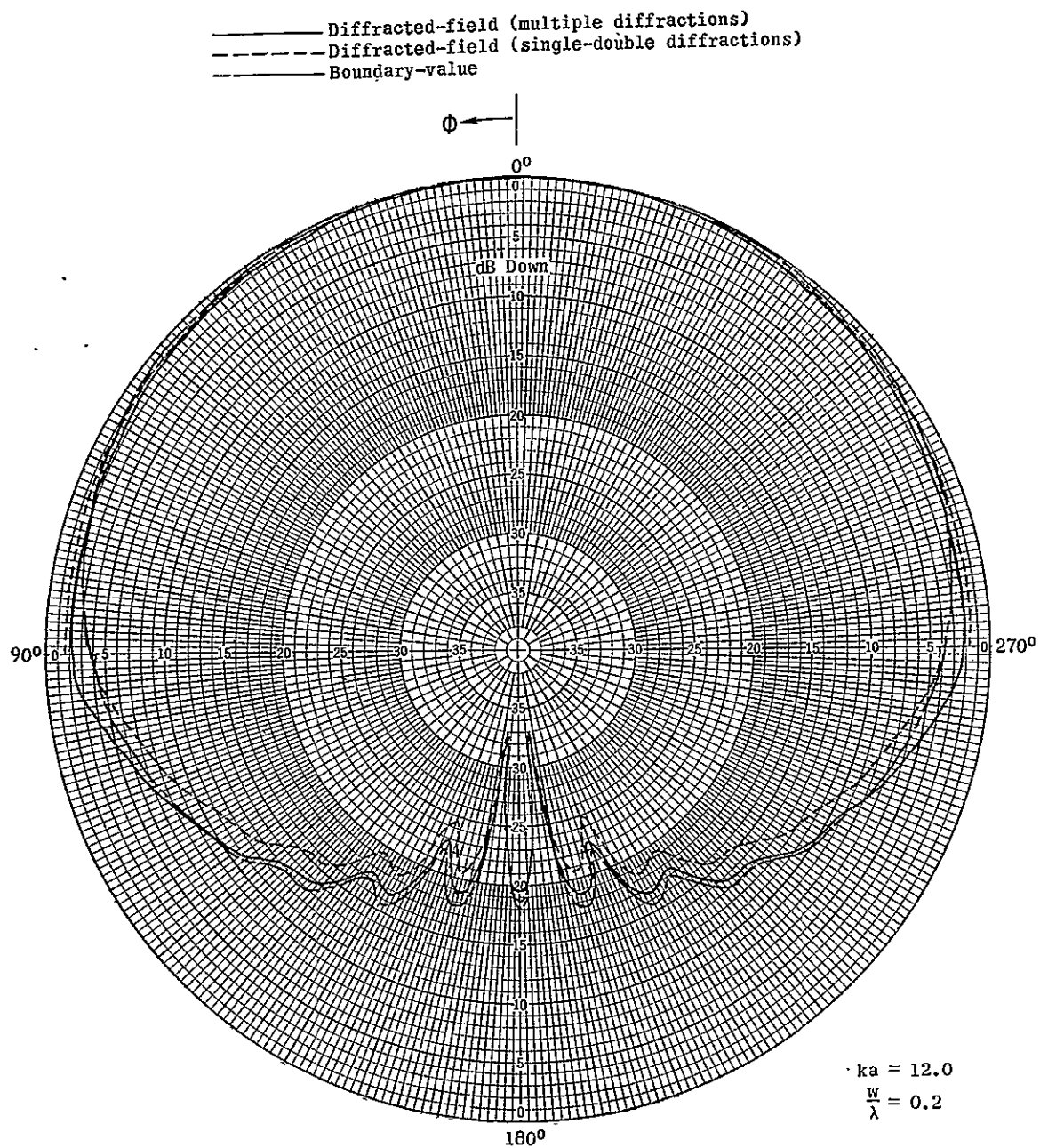
Figure 11. Radiation pattern of axial infinite slot on circular conducting cylinder using half-planes (TEM mode).

The two-dimensional geometry of this mode is shown in Figure 12. The modified equation for the diffracted field is given by

$$E_D(\phi) = \frac{1}{\sqrt{2\pi k}}\, e^{j\left\{k\left[a\cos\phi\cos\beta-(h/2)\cos(\phi+\epsilon+\phi_g)\right]-\pi/4\right\}}\cdot\left\{R_1(\phi)\right.$$

$$\left. + R_2(\phi)e^{jkh\cos(\phi+\epsilon+\phi_g)} + R_1(-\phi)e^{-j2kw\sin(\phi+\epsilon)}\right\} \tag{75}$$

where

$$\phi_g = \frac{\pi}{2} - \epsilon \tag{76}$$

$$h = \frac{w}{\sin\phi_g} \tag{77}$$

and the regions where the appropriate wedge-diffracted fields are applicable are given by

$$R_1(\phi) \qquad\qquad \frac{\pi}{2} + \beta > \phi > -\frac{\pi}{2} \tag{78}$$

$$R_2(\phi) \qquad\qquad \frac{\pi}{2} > \phi > -\left(\frac{\pi}{2}+\beta\right) \tag{79}$$

$$R_1(-\phi) \qquad\qquad \frac{\pi}{2} - \epsilon > \phi > (\phi_g - \epsilon) \tag{80}$$

The creeping wave field is the same as that given by Equation 73 applicable in the regions outlined in Table 1.
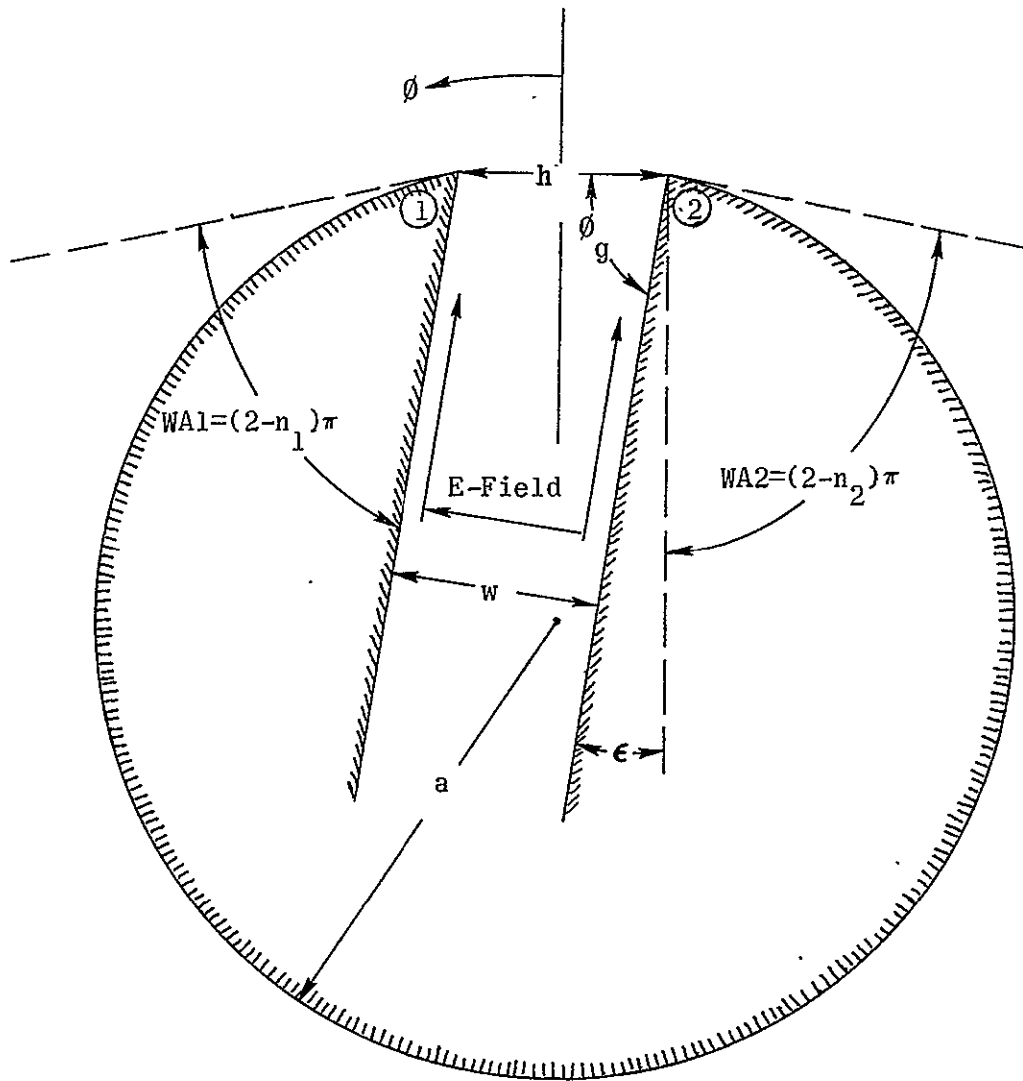
Figure 12. Slanted feed parallel-plate waveguide geometry.

The computed radiation patterns for this mode of operation are shown on Plate V with a field plot for one cylinder in Figure 13. It is observed that the maximum radiation for the cases investigated is oriented at an angle $\phi = -\epsilon/2$. This agrees with the physical reasoning by observing the reflection mechanism of the rays from edge 1 by the side of wedge 2. It can then be concluded that by slanting the feed waveguide at a given angle, it will orient the maximum radiation in other than the $\phi = 0^\circ$ direction. The discontinuities observed in the solution which considers only single-double diffractions occur because third and higher order diffractions which are neglected become significant.

Equatorial Plane Pattern of Circumferential Slots Operating in the TE$_{10}$ Mode

The TE$_{10}$ mode propagation in a parallel-plate guide can be represented by two plane TEM waves reflecting obliquely back and forth between the waveguide walls with the electric field parallel to the edge of the walls. The approximation of the parallel-plate-cylinder geometry by a set of wedges each formed by a waveguide wall and a tangent plane to the cylinder surface at the edge point will not satisfy the electric field boundary conditions. In order to overcome this obstacle, the half-plane approximation is used as a model. The boundary-value solution for a circumferential slot operating in the TE$_{10}$ mode mounted on a circular cylinder exists and it will be used for comparison.

The two-dimensional diffraction geometry is shown in Figure 14. It was found by comparison with the boundary-value solution that one approximation was to replace the edge 1 geometry by a half-plane (n = 2) for the
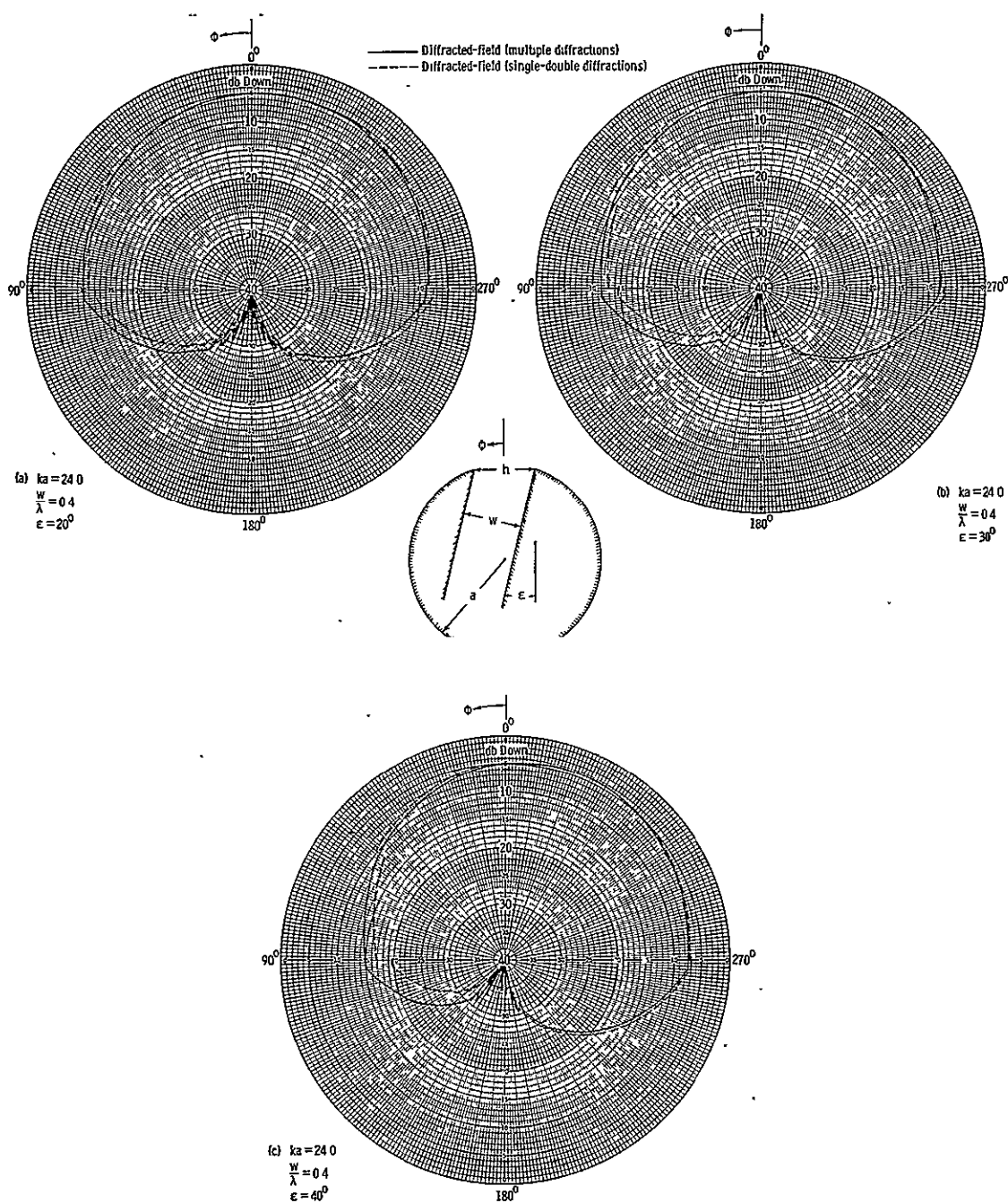
Plate V. Radiation patterns of axial infinite slot on circular
conducting cylinder with slanted feed (TEM mode).
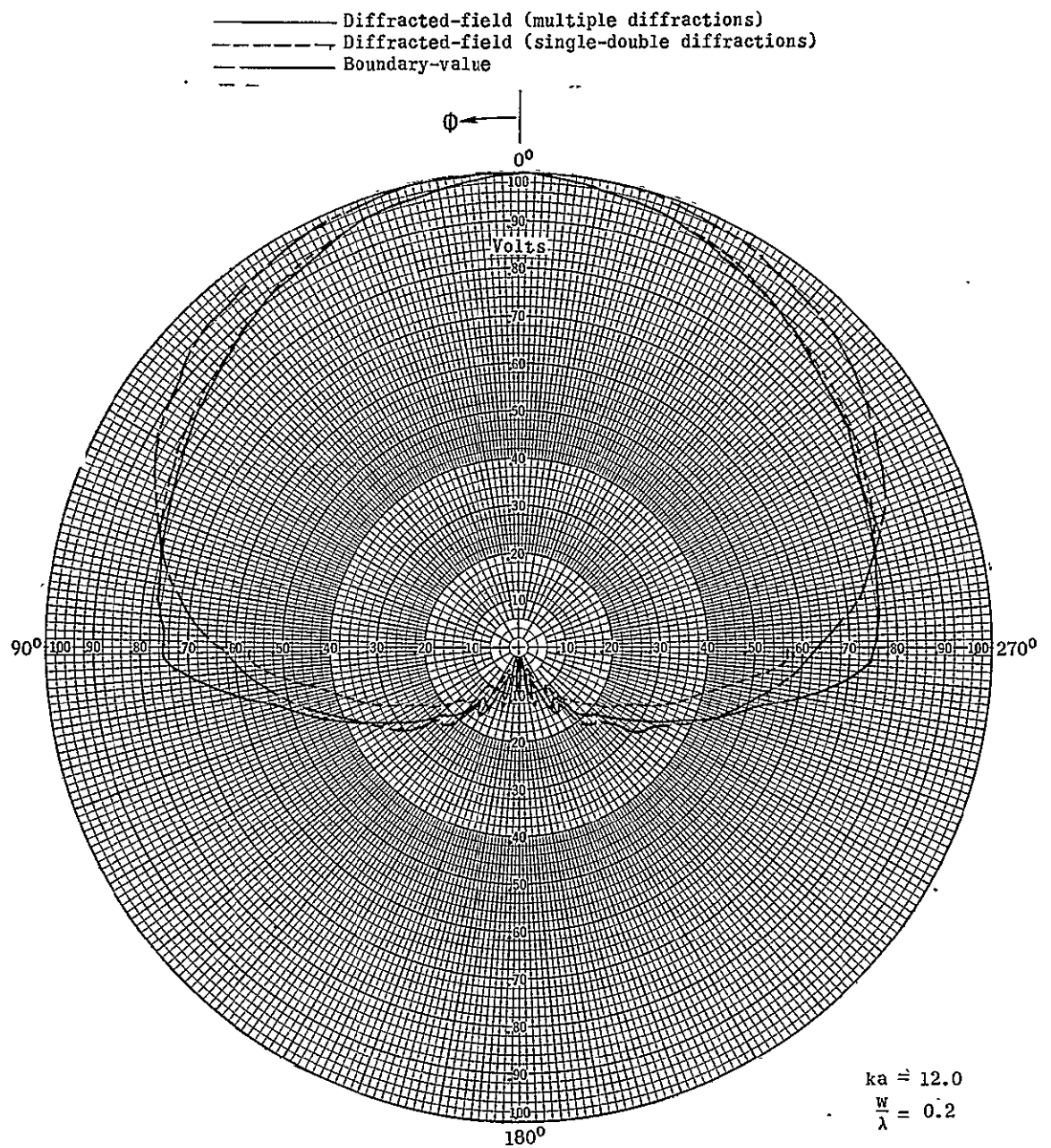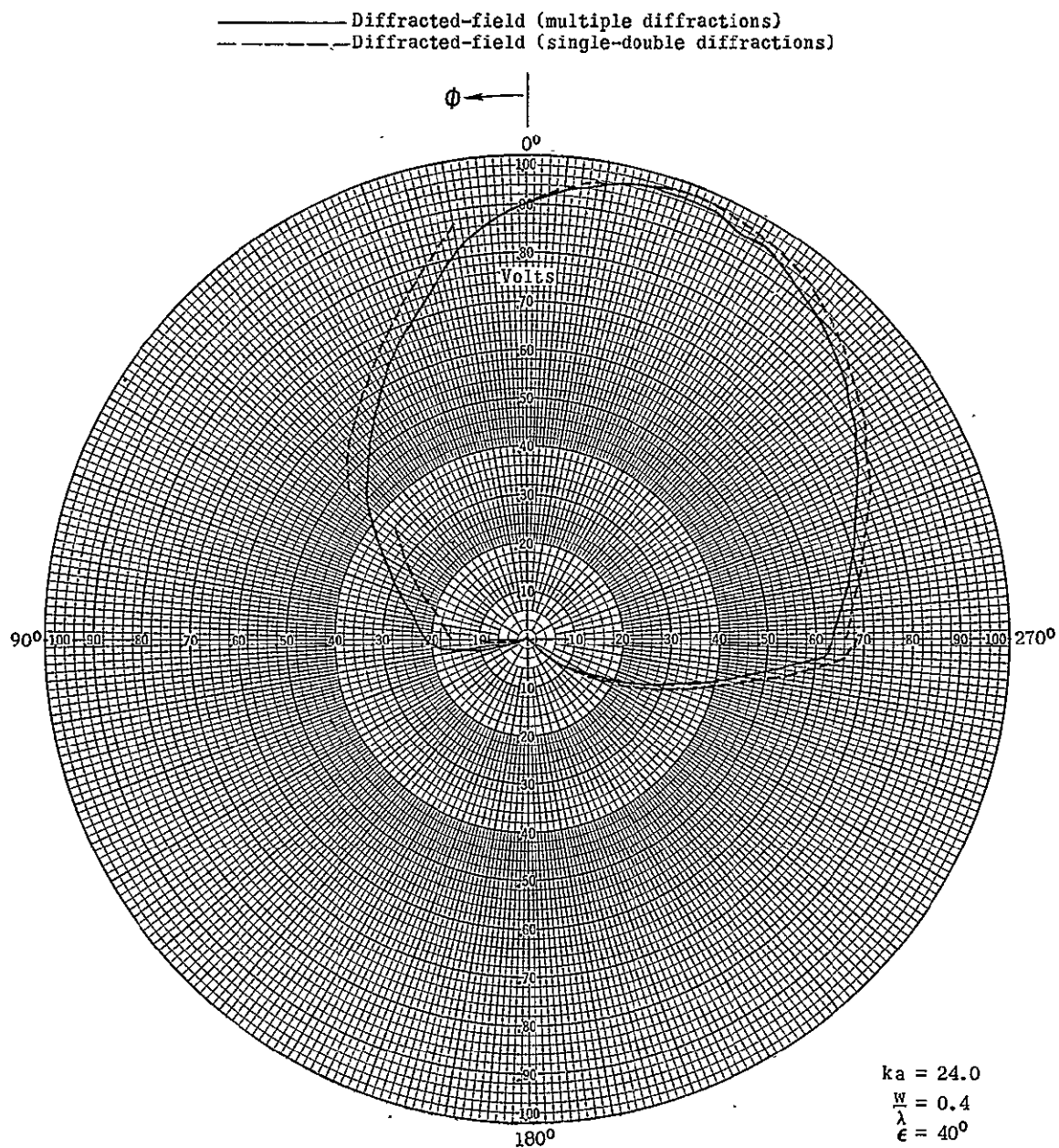
Figure 13. Field plot of axial infinite slot on circular conducting cylinder with slanted feed (TEM mode).
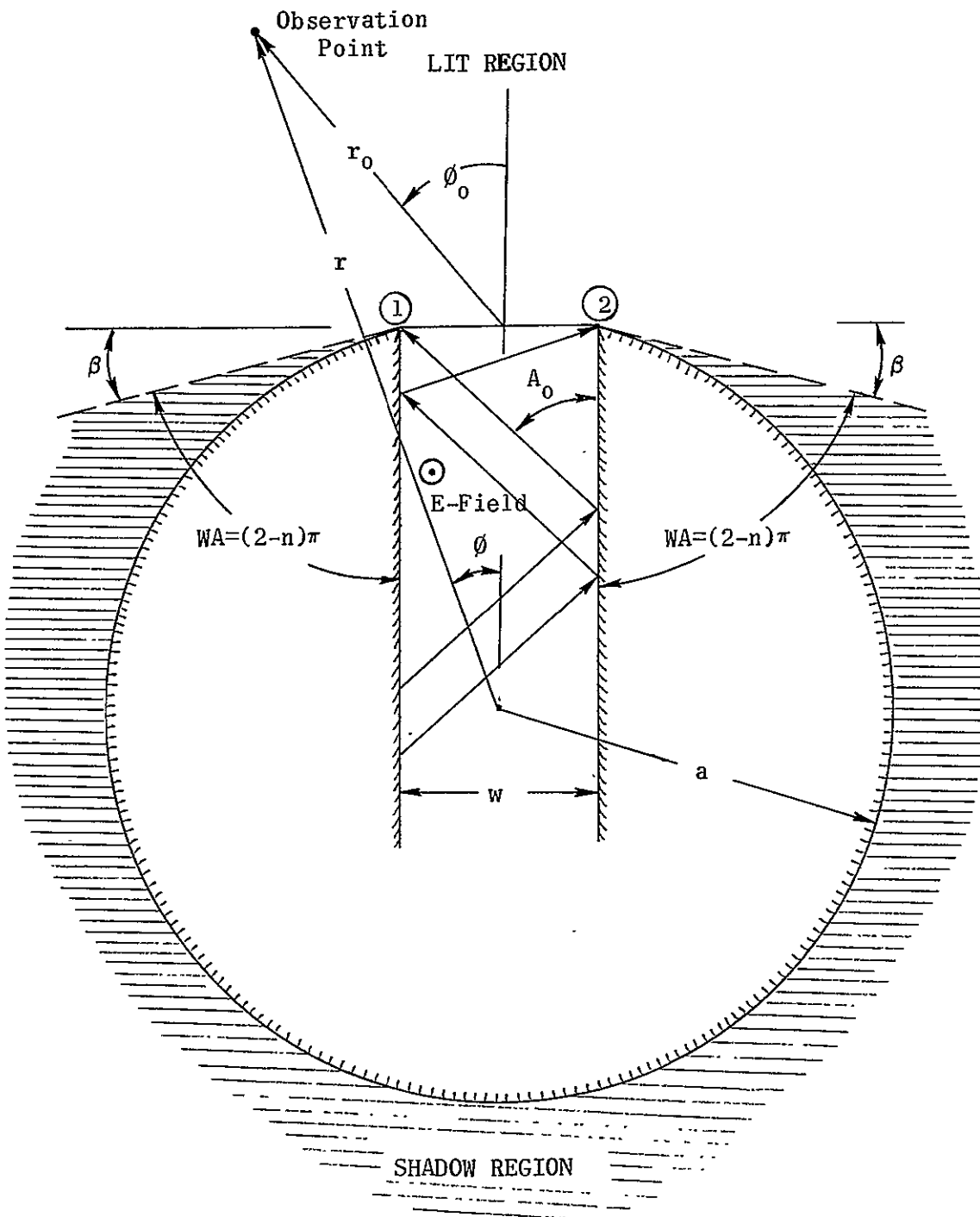
Figure 14. Diffraction geometry for a TE_{10} mode circumferential slot.

57

first order diffraction and by a finite wedge $(n \neq 2)$ for second and higher order diffractions for the $0°$-$180°$ pattern measured in the counterclockwise direction. The edge 2 geometry was replaced by a finite wedge for all orders of diffraction. For the $180°$-$360°$ pattern, the approximations of edge 1 are valid for edge 2 and vice-versa.

The wedge-diffracted field is given by

$$E_D(\phi) = \frac{1}{\sqrt{2\pi k}} e^{j\left\{k\left[(w/2)\sin\phi+a\cos\phi\cos\beta\right] - \pi/4\right\}} \left\{R_1 + R_2 e^{-jkw\sin\phi}\right\}$$

(81)

$$R_1 = R_{D1}^{(1)} + R_{D1}^{(h)}$$

(82)

$$R_2 = R_{D2}^{(1)} + R_{D2}^{(h)}$$

(83)

where $R_{D1}^{(1)}$, $R_{D1}^{(h)}$, $R_{D2}^{(1)}$, and $R_{D2}^{(h)}$ are given by Equations 48, 51, 49, and 52 with $\phi_g = 90°$, $R_{D1}(-\phi) = 0$ and $R_{1P} = 0$. The creeping wave contribution is given by

$$E_C(\phi) = R_A e^{-t_1(\alpha_{os}+jk)} + R_B e^{-t_2(\alpha_{os}+jk)}$$

(84)

where

$$R_A = E_D\left[+\left(\frac{\pi}{2} + \beta\right)\right]$$

(85)

$$R_B = E_D\left[-\left(\frac{\pi}{2}+\beta\right)\right]$$ (86)

as given by Equation 81 and

$$\alpha_{os} = \frac{1}{2a}(ka)^{1/3}\left[\frac{9\pi}{4}\right]^{2/3}e^{j\,\pi/6}$$ (87)

The regions where the appropriate wedge-diffracted and creeping wave fields are applicable are identical to those shown in Table 1 for the TEM mode.

The computed results using this approximation are shown on Plate VI along with the boundary-value solution. It is noted that the solution which includes higher order diffractions gives the best results. A noticeable discontinuity is present at the shadow boundary when higher order diffractions are neglected.

Another approximation for the parallel-plate-cylinder geometry would be a thin-walled guide (n = 2 for all orders of diffraction) as was also true for the TEM mode. Computed results using this model are shown in Figure 15. A good agreement is indicated. The discontinuity in the $\phi = \pm 90°$ directions for the single-double diffractions is again present since higher order diffractions are neglected.

Elevation Plane Pattern of Circumferential Slots on Finite Length Cylinders Operating in the TEM Mode

The elevation plane pattern $\left[F(\theta)|_{\phi=0}\right]$ for a finite length conducting cylinder can be computed using wedge diffraction techniques. The diffracted field from the ends of the cylinder and their contribution
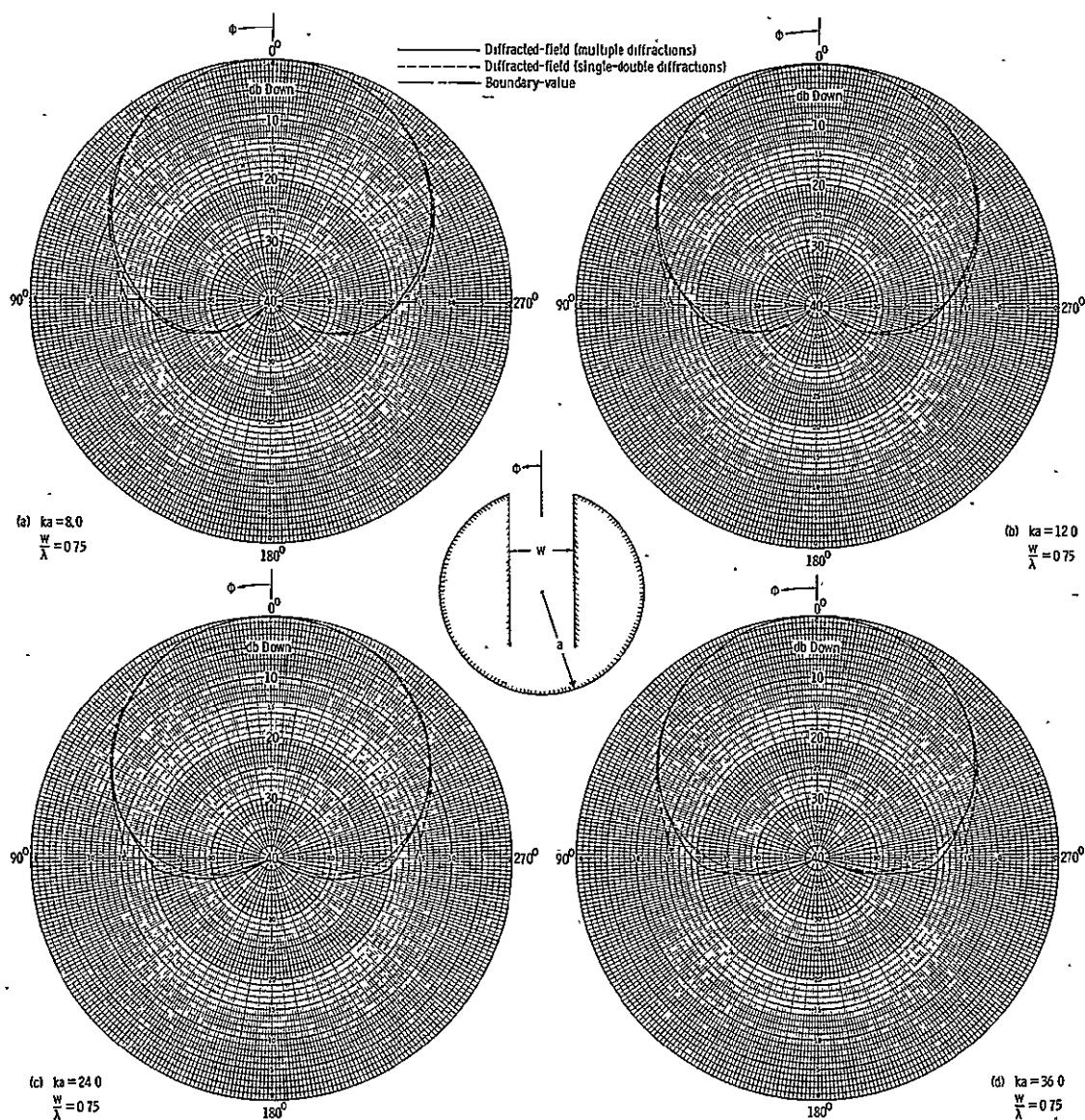
Plate VI. Radiation patterns of circumferential slot on circular conducting cylinder using half-plane and finite wedges (TE_{10} mode).
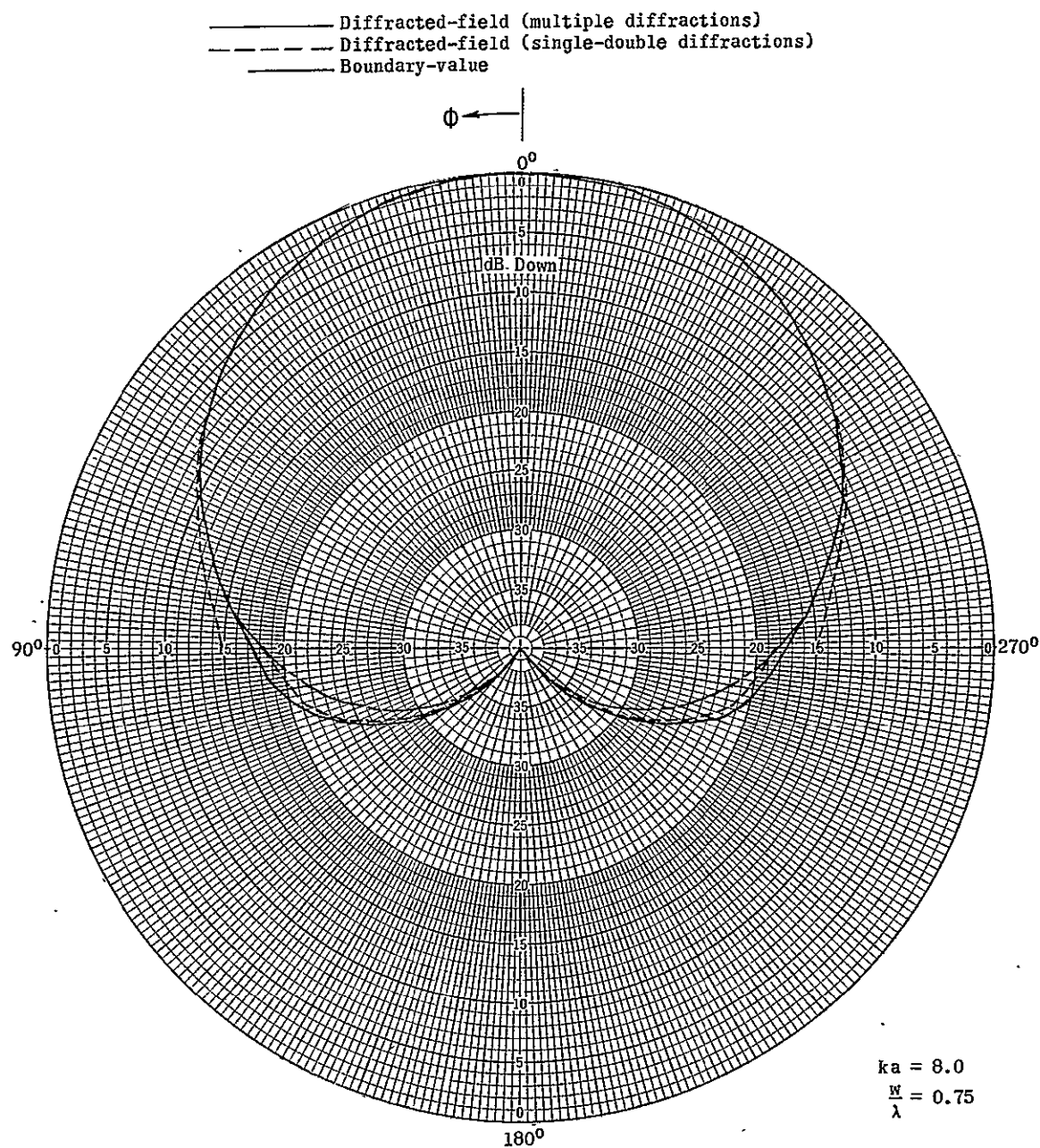
Figure 15. Radiation pattern of circumferential slot on circular conducting cylinder using half-planes (TE_{10} mode).

to the overall radiation pattern can be readily computed. While boundary-value solutions for circular conducting cylinders of infinite length exist,[1,2] no solution which takes into account finite length is available. To check the validity of the technique, experimental results were used for comparison.

The two-dimensional geometry of a slotted cylinder operating in the TEM mode is shown in Figure 16. The diffracted field for the TEM mode from edges 1 and 2 is given by

$$E_D(r_o, \theta_o) = \frac{e^{-j\left[kr_o + \pi/4\right]}}{\sqrt{2\pi kr_o}} R_D(\theta_o) \tag{88}$$

where

$$R_D(\theta_o) = e^{j(kw/2)\sin\theta_o} \left\{ R_1(\theta_o) + R_2(\theta_o)e^{-jkw\sin\theta_o} \right\} \tag{89}$$

and $R_1(\theta_o)$ and $R_2(\theta_o)$ are given by Equations 37 and 41. Diffractions from the aperture in the $\theta_o = \pm\pi/2$ directions will be diffracted by wedges 3 and 4 which in turn will be diffracted by wedges 1, 2, 5, and 6. This process continues to higher orders of diffraction.

To calculate the single-diffracted field by wedge 3, the reciprocity principle (see Appendix) will be applied. This leads to

$$E_{D3}^{(1)}(r_3, \theta_3) = \frac{e^{-j\left[kr_3 + \pi/4\right]}}{\sqrt{2\pi kr_3}} R_{D3}^{(1)}(\theta_3) \tag{90}$$
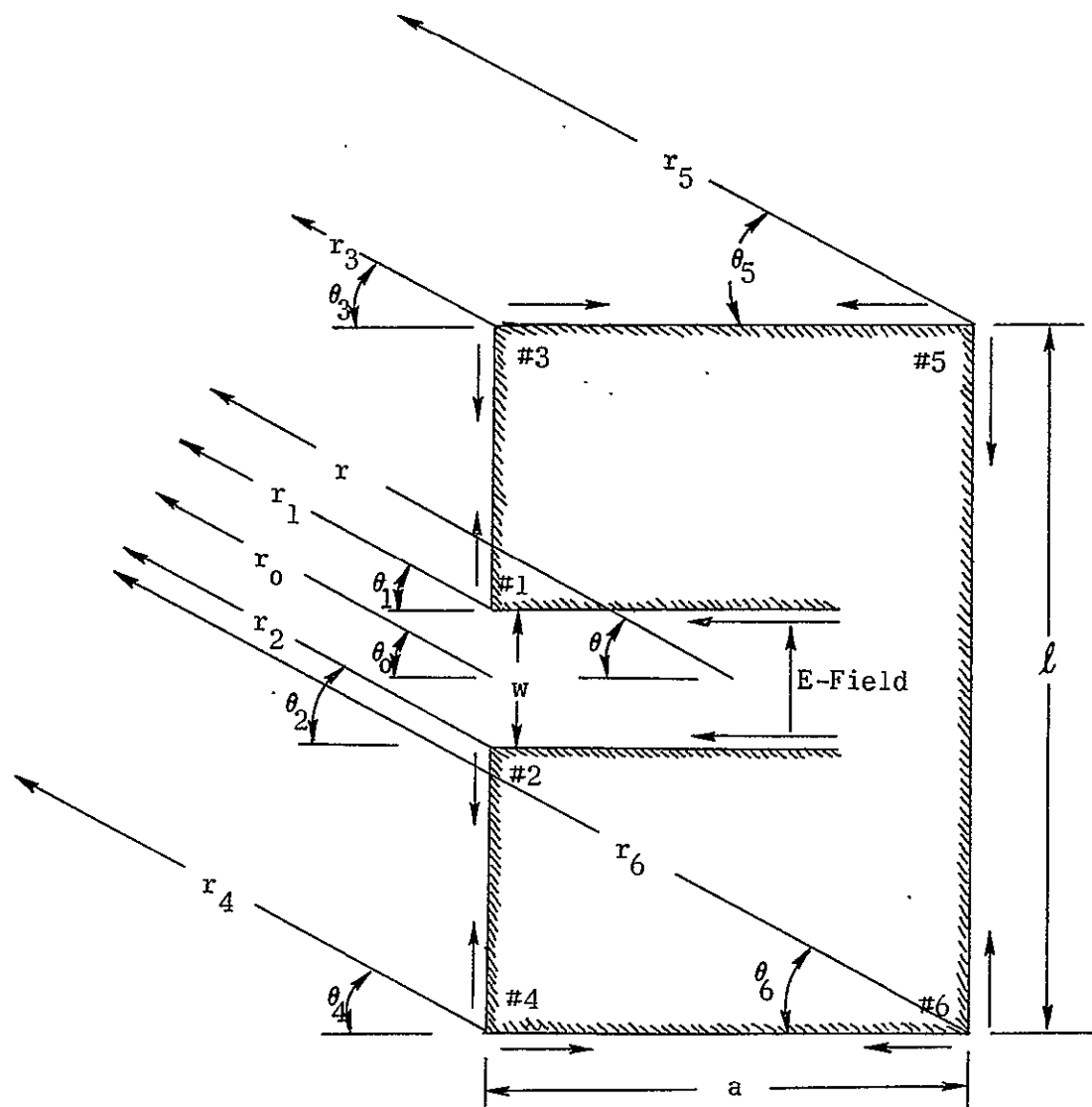
Figure 16. Diffraction mechanism geometry for elevation plane pattern.

where

$$R_{D3}^{(1)}(\theta_3) = R_1\left(\frac{\pi}{2}\right)\left\{V_B\left(\frac{l-w}{2}, \frac{\pi}{2} + \theta_3, n_3\right)\right\} \qquad (91)$$

The single-diffracted ray from wedge 3 in the direction of wedge 5 ($\theta_3 = 180^\circ$) will be diffracted again and its contribution is

$$E_{D5}^{(1)}(r_5, \theta_5) = \frac{e^{-j\left[kr_5 + \pi/4\right]}}{\sqrt{2\pi kr_5}} R_{D5}^{(1)}(\theta_5) \qquad (92)$$

where

$$R_{D5}^{(1)}(\theta_5) = R_{D3}^{(1)}(\pi)\left\{V_B(a, \theta_5, n_5)\right\} \qquad (93)$$

Diffractions from wedge 5 in the directions of wedge 3 ($\theta_5 = 0^\circ$) and wedge 6 ($\theta_5 = 270^\circ$) will cause additional diffractions. Assuming that the length of the cylinder is several wavelengths, the diffractions by wedge 6 are negligible. However, the second order diffractions from wedge 3 are given by.

$$E_{D3}^{(2)}(r_3, \theta_3) = \frac{e^{-j\left[kr_3 + \pi/4\right]}}{\sqrt{2\pi kr_3}} R_{D3}^{(2)}(\theta_3) \qquad (94)$$

where

$$R_{D3}^{(2)}(\theta_3) = R_{D5}^{(1)}(\theta_5 = 0)\left\{V_B(a, \pi - \theta_3, n_3)\right\} \qquad (95)$$

The same procedure used to calculate the fields diffracted by wedges 3 and 5 can be applied to calculate the fields diffracted from wedges 4 and 6 being initiated by the aperture diffractions in the $\theta_o = -\pi/2$ direction.

The first order diffracted fields by wedges 4 and 6 are given by

$$E_{D4}^{(1)}(r_4, \theta_4) = \frac{e^{-j\left[kr_4 + \pi/4\right]}}{\sqrt{2\pi kr_4}} R_{D4}^{(1)}(\theta_4) \tag{96}$$

where

$$R_{D4}^{(1)}(\theta_4) = R_2\left(-\frac{\pi}{2}\right)\left\{V_B\left(\frac{l-w}{2}, \frac{\pi}{2} - \theta_4, n_4\right)\right\} \tag{97}$$

and

$$E_{D6}^{(1)}(r_6, \theta_6) = \frac{e^{-j\left[kr_6 + \pi/4\right]}}{\sqrt{2\pi kr_6}} R_{D6}^{(1)}(\theta_6) \tag{98}$$

where

$$R_{D6}^{(1)}(\theta_6) = R_{D4}^{(1)}(-\pi)\left\{V_B(a, 2\pi - \theta_6, n_6)\right\} \tag{99}$$

and the second order diffracted field from wedge 4 by

$$E_{D4}^{(2)}(r_4,\theta_4) = \frac{e^{-j\left[kr_4 + \pi/4\right]}}{\sqrt{2\pi kr_4}} R_{D4}^{(2)}(\theta_4) \tag{100}$$

where

$$R_{D4}^{(2)}(\theta_4) = R_{D6}^{(1)}(2\pi)\left\{V_B(a,\pi + \theta_4,n_4)\right\} \tag{101}$$

The above derivations were all based upon the validity of the reciprocity principle as outlined in the Appendix.

Shifting the coordinates from the individual edges to the center of the cylinder and assuming the far-field approximations

$$\left. \begin{aligned}
r_0 &\approx r - \frac{a}{2}\cos\theta \\
r_3 &\approx r - d\cos(\gamma - \theta) \\
r_4 &\approx r + d\cos(\pi - \gamma - \theta) \\
r_5 &\approx r - d\cos(\pi - \gamma - \theta) \\
r_6 &\approx r + d\cos(\gamma - \theta)
\end{aligned} \right\} \qquad \text{For phase terms} \tag{102}$$

$$r_0 \approx r_3 \approx r_4 \approx r_5 \approx r_6 \approx r \qquad \text{For amplitude terms} \tag{103}$$

$$\theta_0 \approx \theta_3 \approx \theta_4 \approx \theta_5 \approx \theta_6 \approx \theta \tag{104}$$

where

$$d = \left[\left(\frac{a}{2}\right)^2 + \left(\frac{l}{2}\right)^2 \right]^{1/2} . \tag{105}$$

$$\gamma = \tan^{-1}\left[\frac{l}{a}\right] \tag{106}$$

the diffracted fields, suppressing the $e^{-j\left[kr + \pi/4\right]}/\sqrt{2\pi kr}$ factor, are shown in Table 2 valid in the indicated regions.

It should be pointed out that additional diffractions by each wedge will be present and can very conveniently be accounted for. However, for cylinders with several wavelength·radius and length such diffractions have secondary effects and can be neglected. It is apparent from Figure 16 that the two-dimensional geometry used for the formulation of the elevation plane pattern of a finite length slotted ·cylinder is identical to the cross section configuration of a slotted .finite width ground plane.

The computed results using the fields from Table 2 are shown on Plate VII where they are compared with experimental data.· It is obvious that a very good agreement between theory and experiment is indicated. The ripples in the $-\pi/2 < \theta < \pi/2$ region are present because of the diffraction contribution from the edges of the cylinder, and they become negligible as the length becomes large. The experimental results were obtained from slotted ground plane models since it was deduced .

TABLE 2. WEDGE-DIFFRACTED FIELDS FOR THE ELEVATION PLANE PATTERN

OF A FINITE LENGTH CYLINDER IN THE DIFFERENT REGIONS

Diffraction wedge	Wedge-diffracted field	Region
1 and 2	$E_D(\theta) = e^{j(ka/2)\cos\theta}\left\{R_D(\theta)\right\}$	$-\dfrac{\pi}{2} < \theta < \dfrac{\pi}{2}$
3	$E_{D3}^{(1,2)}(\theta) = e^{jkd\cos(\gamma-\theta)}\left\{R_{D3}^{(1)}(\theta) + R_{D3}^{(2)}(\theta)\right\}$	$-\dfrac{\pi}{2} < \theta < \pi$
4	$E_{D4}^{(1,2)}(\theta) = e^{-jkd\cos(\pi-\gamma-\theta)}\left\{R_{D4}^{(1)}(\theta) + R_{D4}^{(2)}(\theta)\right\}$	$-\pi < \theta < \dfrac{\pi}{2}$
5	$E_{D5}^{(1)}(\theta) = e^{jkd\cos(\pi-\gamma-\theta)}\left\{R_{D5}^{(1)}(\theta)\right\}$	$0 < \theta < \dfrac{3\pi}{2}$
6	$E_{D6}^{(1)}(\theta) = e^{-jkd\cos(\gamma-\theta)}\left\{R_{D6}^{(1)}(\theta)\right\}$	$-\dfrac{3\pi}{2} < \theta < 0$
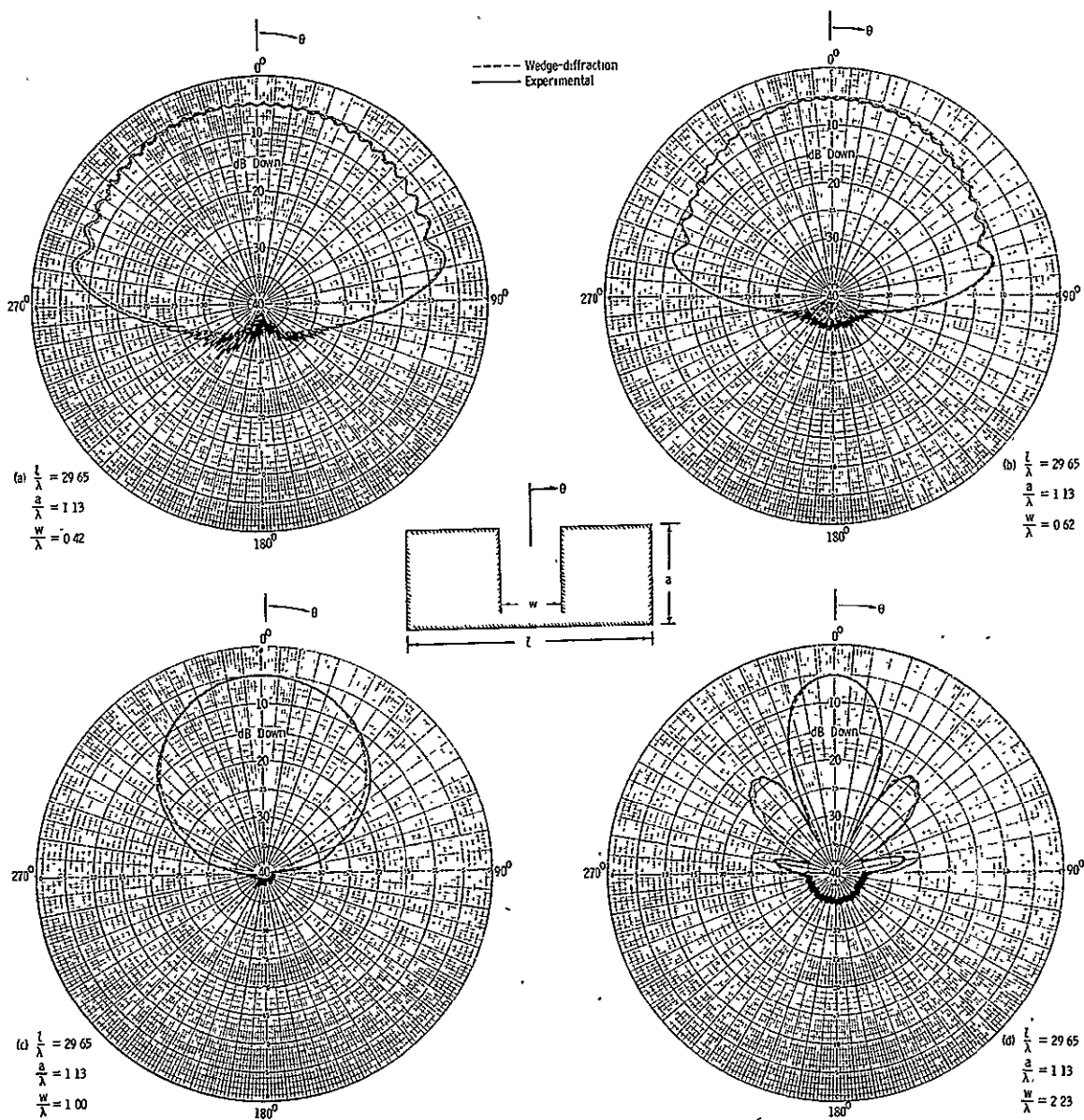
Plate VII. Elevation plane patterns of finite length cylinder (TEM mode).

that their two-dimensional geometry is identical to that of a slotted cylinder.

The beamwidth of the main lobe is decreased as the aperture width is increased. The smoothest pattern and the lowest back lobes are obtained for the aperture whose width is exactly one wavelength since complete cancellation of the fields diffracted from wedges 1 and 2 in the $\theta = \pm\pi/2$ directions occurs. The ripples in the $-90° < \theta < 90°$ region which are much in evidence in (a) and (b) do not appear in (c) and (d) because the fields in the $\theta = \pm\pi/2$ directions are very weak and any diffractions from the edges are negligible. Additional lobes appear as the aperture width is larger than one wavelength.

Another formulation for the diffractions from wedges 1 and 2 would be to use continuous double diffractions.[37] In this case, double-diffracted rays from wedge 2 $\left[R_{D2}^{(2)}(\theta)\right]$ are neglected in the $0° < \theta < 90°$ region while double-diffracted rays from wedge 1 $\left[R_{D1}^{(2)}(\theta)\right]$ are neglected in the $-90° < \theta < 0°$ region. Computed results using the above formulation are shown on Plate VIII where they are compared with experimental results. Again a very good agreement between theory and experiment is indicated.
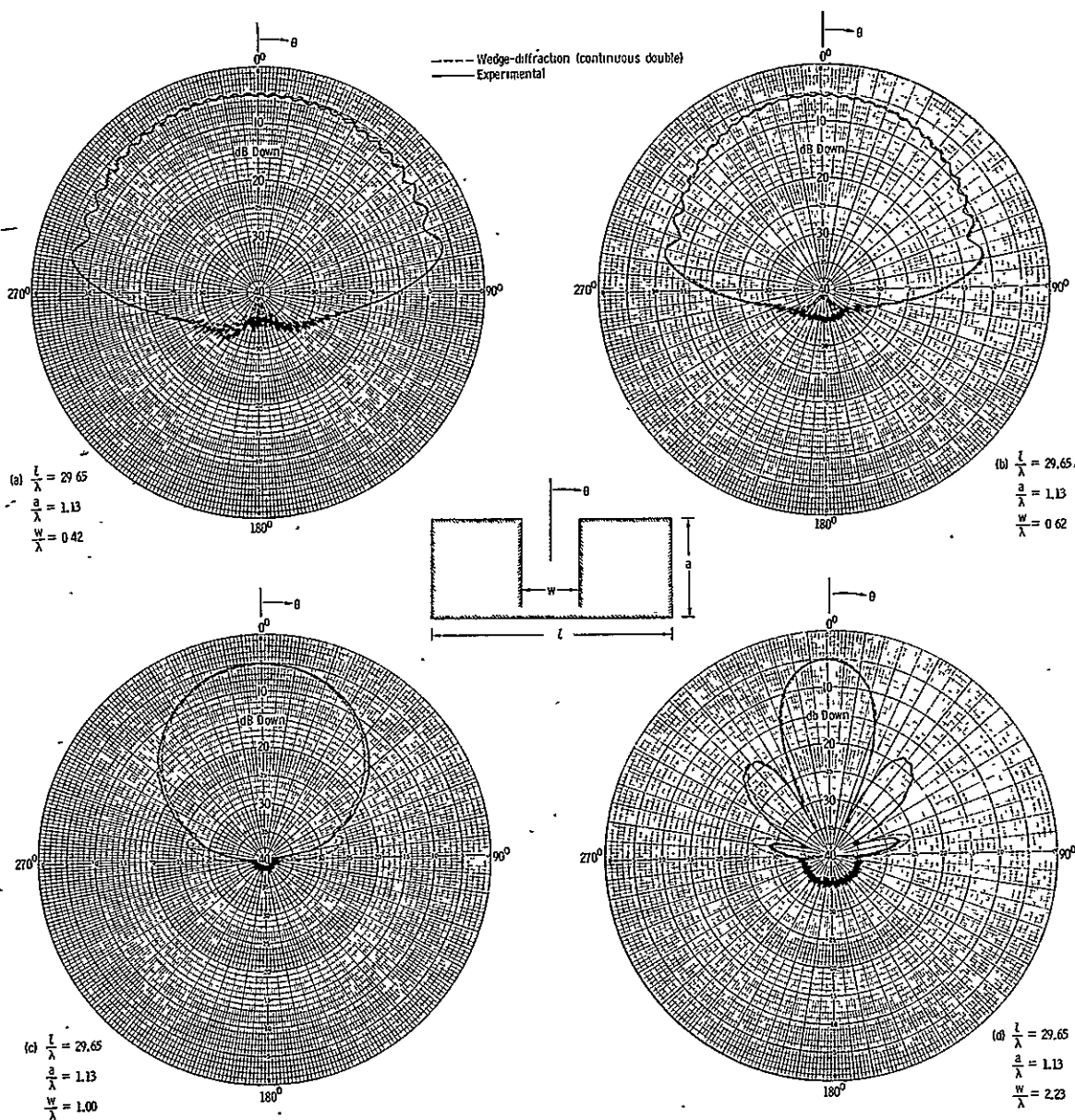
Plate VIII. Elevation plane patterns of finite length cylinder using continuous double diffractions (TEM mode).

CHAPTER IV

ELLIPTICAL CYLINDER RADIATION

Flush-mounted antennas are commonly used on space vehicles,
missiles, and aircraft. However, their radiation properties usually
cannot be predicted analytically because the geometric shape of the
body to which they are mounted does not conform to a coordinate system
where the wave equation is separable. The method used to analyze the
radiation properties of axial slots on circular conducting cylinders
can be applied to cylindrical shaped bodies of arbitrary convex cross
section. One geometry of wide interest is an elliptical cylinder which
can be used as an approximate model for the wings of an aircraft or the
fins of a missile.

The far-field radiation produced by a slot of arbitrary shape on
the surface of an elliptical cylinder of infinite length using modal
solutions has been carried out by Wait.[5] Computations using the modal
solution are numerically convenient only for very thin-shaped elliptical
cylinders, and as the size increases (larger ka and kb) higher order
terms must also be included for convergence. However, the analysis
using wedge diffraction and creeping wave theory can be used for com-
putations of any size and shape of an elliptical cylinder. As the
physical dimensions increase, the accuracy of the obtained data increases
because diffraction coefficients (D_{mh}) and decay constants (α_{mh}) used in

71

the analysis are derived from asymptotic series of canonical boundary-value problems for $\lambda \to 0$.

Equatorial Plane Pattern of Axial Slots Operating in the TEM Mode

As in the analysis of the circular cylinder, the two-dimensional geometry for an axial slot mounted on an elliptical cylinder and operating in the TEM mode is shown in Figure 17. Again, the junctions formed by the walls of the parallel-plate waveguide and the planes tangent to the surface of the cylinder at the edge points are approximated by a pair of infinite wedges of finite included angle WA = $(2 - n)\pi$. The wedge-diffracted field is given by Equation 66 and is repeated here.

$$E_D(r_o, \phi_o) = \frac{e^{-j\left\{k\left[r_o - (w/2)\sin\phi\right] + \pi/4\right\}}}{\sqrt{2\pi k r_o}} \left\{R_1(\phi_o) + R_2(\phi_o)e^{-jkw\sin\phi_o}\right\}$$

(107)

Using the far-field approximations

$$r_o \approx r - \tau_o \cos\phi \cos\beta \qquad \text{For phase terms} \quad (108)$$

$$r_o \approx r \qquad \text{For amplitude terms} \quad (109)$$

$$\phi_o \approx \phi \qquad (110)$$

Equation 107 reduces to

LIT REGION

Observation
Point
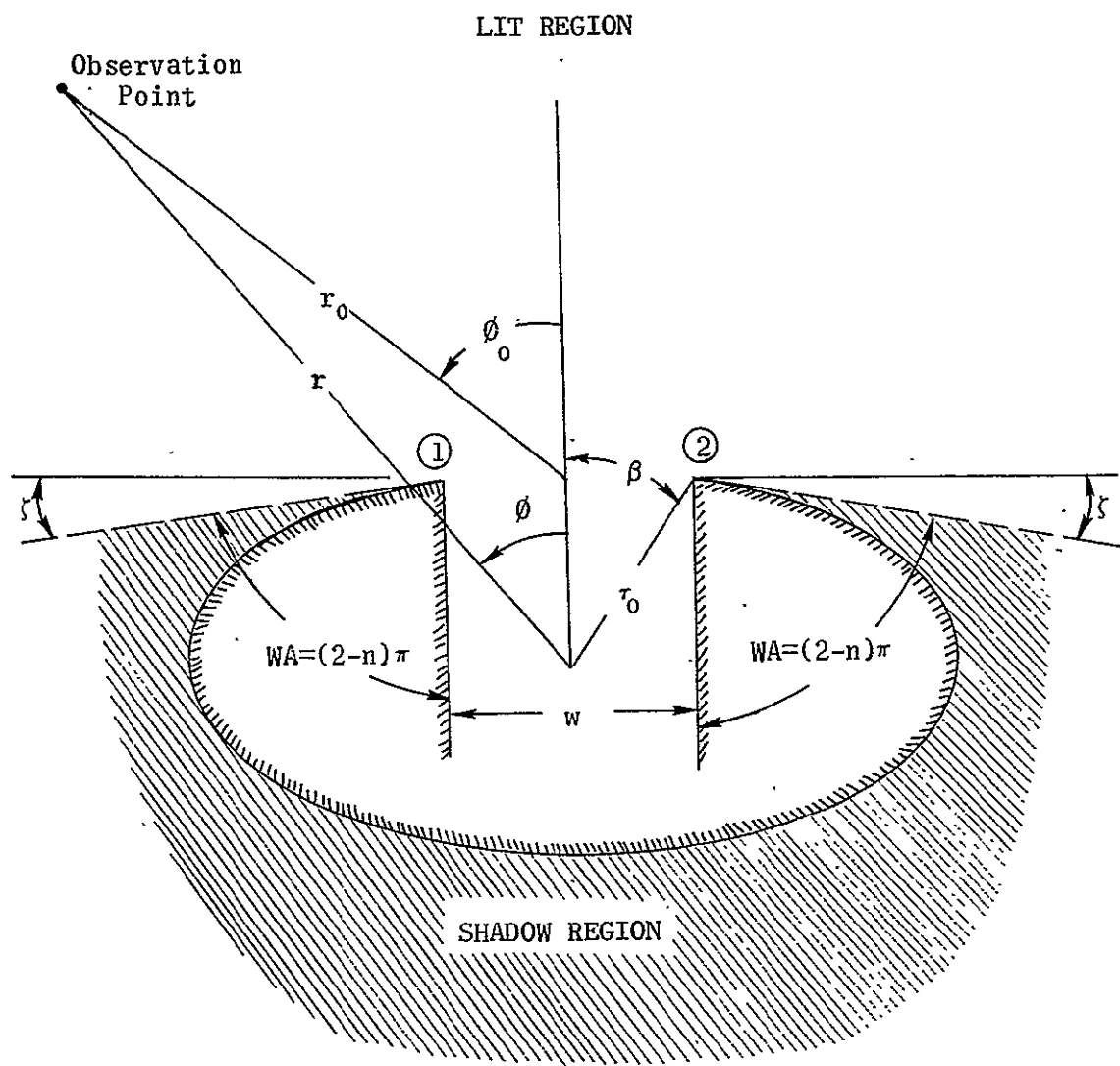
Figure 17. Lit and shadow regions for elliptical cylinder.

$$E_D(r,\phi) = \frac{1}{\sqrt{2\pi k}} \frac{e^{-jkr}}{\sqrt{r}} e^{j\left\{k\left[(w/2)\sin\phi + \tau_o\cos\phi\cos\beta\right] - \pi/4\right\}} \left\{R_1(\phi)\right.$$

$$\left. + R_2(\phi)e^{-jkw\sin\phi}\right\}$$

where

$$\tau_o = \sqrt{x_o^2 + y_o^2} \tag{112}$$

$$x_o = \pm \frac{w}{2} \tag{113}$$

$$y_o = \frac{b}{2a}\sqrt{4a^2 - w^2} \tag{114}$$

with $R_1(\phi)$ and $R_2(\phi)$ as defined previously.

The creeping wave field is given by Equation 65 and repeated here.

$$E_C(s,\phi) = R_A \frac{D_{oh}(P_1)}{D_{oh}(Q_1)} \frac{e^{-jk(t_1+s_1)}}{\sqrt{s_1}} e^{-\int_o^{t_1} \alpha_{oh}(\rho)ds}$$

$$+ R_B \frac{D_{oh}(P_2)}{D_{oh}(Q_2)} \frac{e^{-jk(t_2+s_2)}}{\sqrt{s_2}} e^{-\int_o^{t_2} \alpha_{oh}(\rho)ds} \tag{115}$$

From the geometry of Figure 18, one may obtain the far-field approximations

$$\tau_1 \approx \tau_2 \approx \tau \tag{116}$$
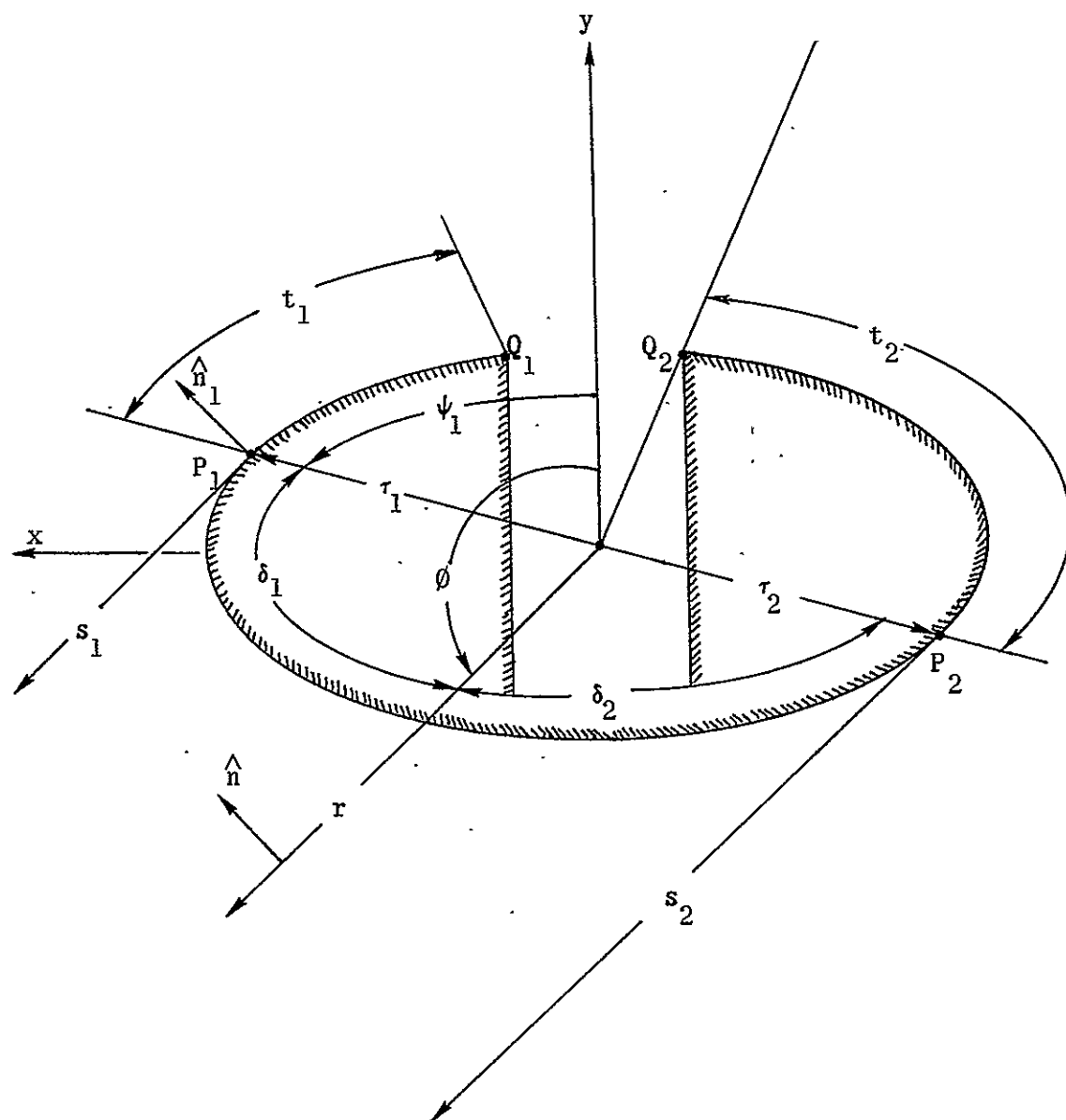
Figure 18. Far-zone creeping wave field coordinates.

$$\delta_2 \approx \pi - \delta_1 \qquad\qquad\qquad\qquad\qquad\qquad (117)$$

$$\left.\begin{array}{l} s_1 \approx r - \tau \cos \delta_1 \\[2mm] s_2 \approx r + \tau \cos \delta_1 \end{array}\right\} \qquad\qquad \text{For phase terms} \qquad (118)$$

$$s_1 \approx s_2 \approx r \qquad\qquad\qquad \text{For amplitude terms} \qquad (119)$$

Equation 115 reduces to

$$E_C(r,\phi) = V_A \frac{e^{-jkr}}{\sqrt{r}} \, e^{-jkt_1} e^{-\int_o^{t_1} \alpha_{oh}(\rho)ds}$$

$$+ V_B \frac{e^{-jkr}}{\sqrt{r}} \, e^{-jkt_2} e^{-\int_o^{t_2} \alpha_{oh}(\rho)ds} \qquad\qquad (120)$$

where

$$V_A = R_A \frac{D_{oh}(P_1)}{D_{oh}(Q_1)} \, e^{jk\tau\cos\delta_1} \qquad\qquad\qquad (121)$$

$$V_B = R_B \frac{D_{oh}(P_2)}{D_{oh}(Q_2)} \, e^{-jk\tau\cos\delta_1} \qquad\qquad\qquad (122)$$

$$R_A = \frac{\sqrt{r}}{e^{-jkr}} E_D\left[r, +\left(\frac{\pi}{2} + \zeta\right)\right] = E_i(Q_1)\left[D_{oh}(Q_1)\right]^2 \tag{123}$$

$$R_B = \frac{\sqrt{r}}{e^{-jkr}} E_D\left[r, -\left(\frac{\pi}{2} + \zeta\right)\right] = E_i(Q_2)\left[D_{oh}(Q_2)\right]^2 \tag{124}$$

as obtained from Equation 111.

Expressions for the radius of curvature and differential arc length for an ellipse can be obtained by applying the basic geometric

$$ds = \sqrt{(dx)^2 + (dy)^2} \tag{125}$$

$$\rho = \frac{\left[1 + (y')^2\right]^{3/2}}{|y''|} \tag{126}$$

$$x = \tau \sin \phi \tag{127}$$

$$y = \tau \cos \phi \tag{128}$$

Using Equations 125, 127, and 128 lead to

$$dx = \tau \cos \phi \, d\phi + \sin \phi \, d\tau \tag{129}$$

$$dy = -\tau \sin \phi \, d\phi + \cos \phi \, d\tau \tag{130}$$

$$ds = \left[\tau^2 (d\phi)^2 + (d\tau)^2\right]^{1/2} \tag{131}$$

$$y' = -\left(\frac{b}{a}\right)^2 \frac{\sin \phi}{\cos \phi} \tag{132}$$

$$y'' = \frac{b}{a^5} \frac{\left(a^2 \cos^2\phi + b^2 \sin^2\phi\right)^{3/2}}{\cos^3\phi} \tag{133}$$

Substituting Equations 127 and 128 into the equation for an ellipse in rectangular coordinates

$$\frac{x^2}{a^2} + \frac{y^2}{b^2} = 1 \tag{134}$$

lead to

$$\tau = \frac{ab}{\left[a^2 \cos^2\phi + b^2 \sin^2\phi\right]^{1/2}} \tag{135}$$

$$d\tau = \frac{ab(a^2 - b^2)\sin \phi \cos \phi}{\left[a^2 \cos^2\phi + b^2 \sin^2\phi\right]^{3/2}} \, d\phi \tag{136}$$

Substituting Equations 132 and 133 into 126, and Equations 135 and 136 into 131 yield

$$\rho = \frac{1}{ab}\left[\frac{a^4\cos^2\phi + b^4\sin^2\phi}{a^2\cos^2\phi + b^2\sin^2\phi}\right]^{3/2} \tag{137}$$

$$ds = ab\,\frac{(a^4\cos^2\phi + b^4\sin^2\phi)^{1/2}}{(a^2\cos^2\phi + b^2\sin^2\phi)^{3/2}}\,d\phi \tag{138}$$

The arc length and complex attenuation factor of the creeping wave on the elliptic surface can then be expressed as

$$t = \int_{\phi_{11}}^{\phi_{12}} ds = ab\int_{\phi_{11}}^{\phi_{12}}\frac{(a^4\cos^2\phi + b^4\sin^2\phi)^{1/2}}{(a^2\cos^2\phi + b^2\sin^2\phi)^{3/2}}\,d\phi \tag{139}$$

$$\int_0^t \alpha_{oh}(\rho)\,ds = \frac{(k)^{1/3}}{2}\left(\frac{3\pi ab}{4}\right)^{2/3} e^{j\,\pi/6} \times$$

$$\int_{\phi_{11}}^{\phi_{12}} \frac{ab\,d\phi}{\left[(a^4\cos^2\phi + b^4\sin^2\phi)(a^2\cos^2\phi + b^2\sin^2\phi)\right]^{1/2}} \tag{140}$$

where

ϕ_{11} = trapping point angle of the creeping wave

ϕ_{12} = exit point angle of the creeping wave

The points of trapping, Q_1 and Q_2, are given by Equations 113 and 114. To determine the points of reradiation, P_1 and P_2, of each creeping wave on the surface of the elliptical cylinder, the vector cross product will be utilized.[24] As shown in Figure 18 for the observation angle ϕ (assuming far-field observations)

$$\hat{n} \times \hat{n}_1 = 0 \tag{141}$$

where

$$\hat{n} = -\hat{x} \cos \phi + \hat{y} \sin \phi = \begin{array}{l} \text{unit vector perpendicular to the} \\ \text{line from the origin of the} \\ \text{cylinder to the observation} \\ \text{point} \end{array} \tag{142}$$

$$\hat{n}_1 = \frac{\hat{x}\left(\dfrac{x}{a^2}\right) + \hat{y}\left(\dfrac{y}{b^2}\right)}{\left[\left(\dfrac{x}{a^2}\right)^2 + \left(\dfrac{y}{b^2}\right)^2\right]^{1/2}} = \begin{array}{l} \text{unit vector normal to the} \\ \text{cylinder surface at the} \\ \text{point of tangency} \end{array} \tag{143}$$

Applying Equation 141 and using the equation for an ellipse in rectangular coordinates

$$\frac{x^2}{a^2} + \frac{y^2}{b^2} = 1 \tag{144}$$

leads to

$$x_1(P_1) = \frac{-a^2\cos\phi}{\left[a^2\cos^2\phi + b^2\sin^2\phi\right]^{1/2}}$$

$$y_1(P_1) = \frac{b^2\sin\phi}{\left[a^2\cos^2\phi + b^2\sin^2\phi\right]^{1/2}} \left.\vphantom{\begin{array}{c}1\\1\\1\end{array}}\right\} \quad \text{Reradiation point } P_1 \quad (145)$$

$$\psi_1 = \tan^{-1}\left[\frac{x_1(P_1)}{y_1(P_1)}\right]$$

$$x_2(P_2) = \frac{a^2\cos\phi}{\left[a^2\cos^2\phi + b^2\sin^2\phi\right]^{1/2}}$$

$$\left.\vphantom{\begin{array}{c}1\\1\\1\end{array}}\right\} \quad \text{Reradiation point } P_2 \quad (146)$$

$$y_2(P_2) = \frac{-b^2\sin\phi}{\left[a^2\cos^2\phi + b^2\sin^2\phi\right]^{1/2}}$$

The angles β and ζ are given by

$$\beta = \tan^{-1}\left[\frac{a}{b}\frac{w}{\sqrt{4a^2 - w^2}}\right] \tag{147}$$

$$\zeta = \tan^{-1}\left[\frac{b}{a}\frac{w}{\sqrt{4a^2 - w^2}}\right] \tag{148}$$

The wedge-diffracted and creeping wave fields, suppressing the $e^{-jkr}/\sqrt{r}$ factor, are given by

$$E_D(\phi) = \frac{1}{\sqrt{2\pi k}}\, e^{j\left\{k\left[(w/2)\sin\phi + \tau_o\cos\phi\cos\beta\right] - \pi/4\right\}}\left\{R_1 + R_2 e^{-jkw\sin\phi}\right\} \tag{149}$$

$$E_C(\phi) = V_A e^{-jkt_1} e^{-\int_o^{t_1}\alpha_{oh}(\rho)ds} + V_B e^{-jkt_2} e^{-\int_o^{t_2}\alpha_{oh}(\rho)ds} \tag{150}$$

$$t_1 = \int_{\phi_{11}}^{\phi_{12}} ds \tag{151}$$

$$t_2 = \int_{\phi_{21}}^{\phi_{22}} ds \tag{152}$$

In general, the total field is given by

$$E_T(\phi) = E_D(\phi) + E_C(\phi) \tag{153}$$

where the appropriate fields must be considered in each region as shown in Table 3.

Radiation patterns computed using the fields from Table 3 in their respective regions are shown on Plates IX, X, and Figure 19. Experimental models were constructed and the obtained data were used for comparison since boundary-value solutions are numerically convenient only for very thin elliptical cylinder. Harrington[4] points out that the equatorial radiation pattern ($\theta = 90^o$ plane) for a circular cylinder with finite axial slot is identical to that with an infinite axial slot. It is

TABLE 3. WEDGE-DIFFRACTED AND CREEPING WAVE FIELDS FOR THE EQUATORIAL PLANE PATTERN OF AN ELLIPTICAL CYLINDER IN THE DIFFERENT REGIONS

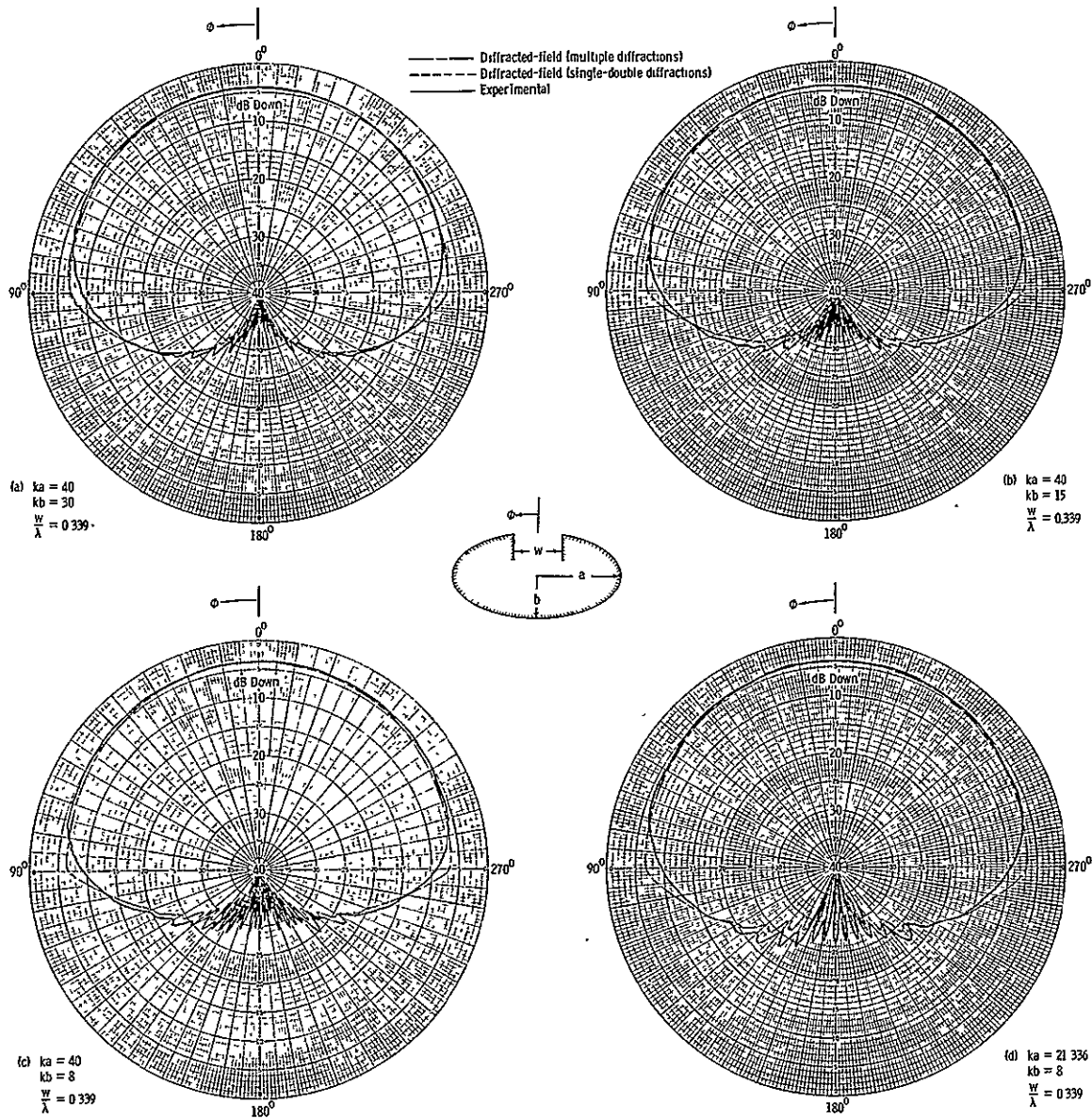| Regions	Wedge-diffracted field $E_D(\phi)$	Creeping wave field $E_C(\phi)$	ϕ_{11} ϕ_{12}	ϕ_{21} ϕ_{22}
Region I $0 < \phi \leq \frac{\pi}{2} - \zeta$	$\dfrac{e^{j\left[k((w/2)\sin\phi + r_0\cos\phi\cos\beta) - \pi/4\right]}}{\sqrt{2\pi k}}\left\{R_1 + R_2 e^{-jkw\sin\phi}\right\}$	$V_A e^{-jkt_1} e^{-\int_0^{t_1} a_{oh}(\rho)ds} + V_B e^{-jkt_2} e^{-\int_0^{t_2} a_{oh}(\rho)ds}$	$\phi_{11} = \beta$ $\phi_{12} = 2\pi + \psi_1$	$\phi_{21} = -(\pi - \psi_1)$ $\phi_{22} = -\beta$
Region II $\frac{\pi}{2} - \zeta < \phi \leq \frac{\pi}{2}$	$\dfrac{e^{j\left[k((w/2)\sin\phi + r_0\cos\phi\cos\beta) - \pi/4\right]}}{\sqrt{2\pi k}}\left\{R_1 + R_2 e^{-jkw\sin\phi}\right\}$	$V_B e^{-jkt_2} e^{-\int_0^{t_2} a_{oh}(\rho)ds}$	----	$\phi_{21} = -(\pi - \psi_1)$ $\phi_{22} = -\beta$
Region III $\frac{\pi}{2} < \phi \leq \frac{\pi}{2} + \zeta$	$\dfrac{e^{j\left[k((w/2)\sin\phi + r_0\cos\phi\cos\beta) - \pi/4\right]}}{\sqrt{2\pi k}}\left\{R_1\right\}$	$V_B e^{-jkt_2} e^{-\int_0^{t_2} a_{oh}(\rho)ds}$	---	$\phi_{21} = -(\pi - \psi_1)$ $\phi_{22} = -\beta$
Region IV $\frac{\pi}{2} + \zeta < \phi \leq \pi$	0	$V_A e^{-jkt_1} e^{-\int_0^{t_1} a_{oh}(\rho)ds} + V_B e^{-jkt_2} e^{-\int_0^{t_2} a_{oh}(\rho)ds}$	$\phi_{11} = \beta$ $\phi_{12} = \psi_1$	$\phi_{21} = -(\pi - \psi_1)$ $\phi_{22} = -\beta$

Plate IX. Radiation patterns of axial infinite slot on elliptical conducting cylinder using finite wedges (TEM mode).
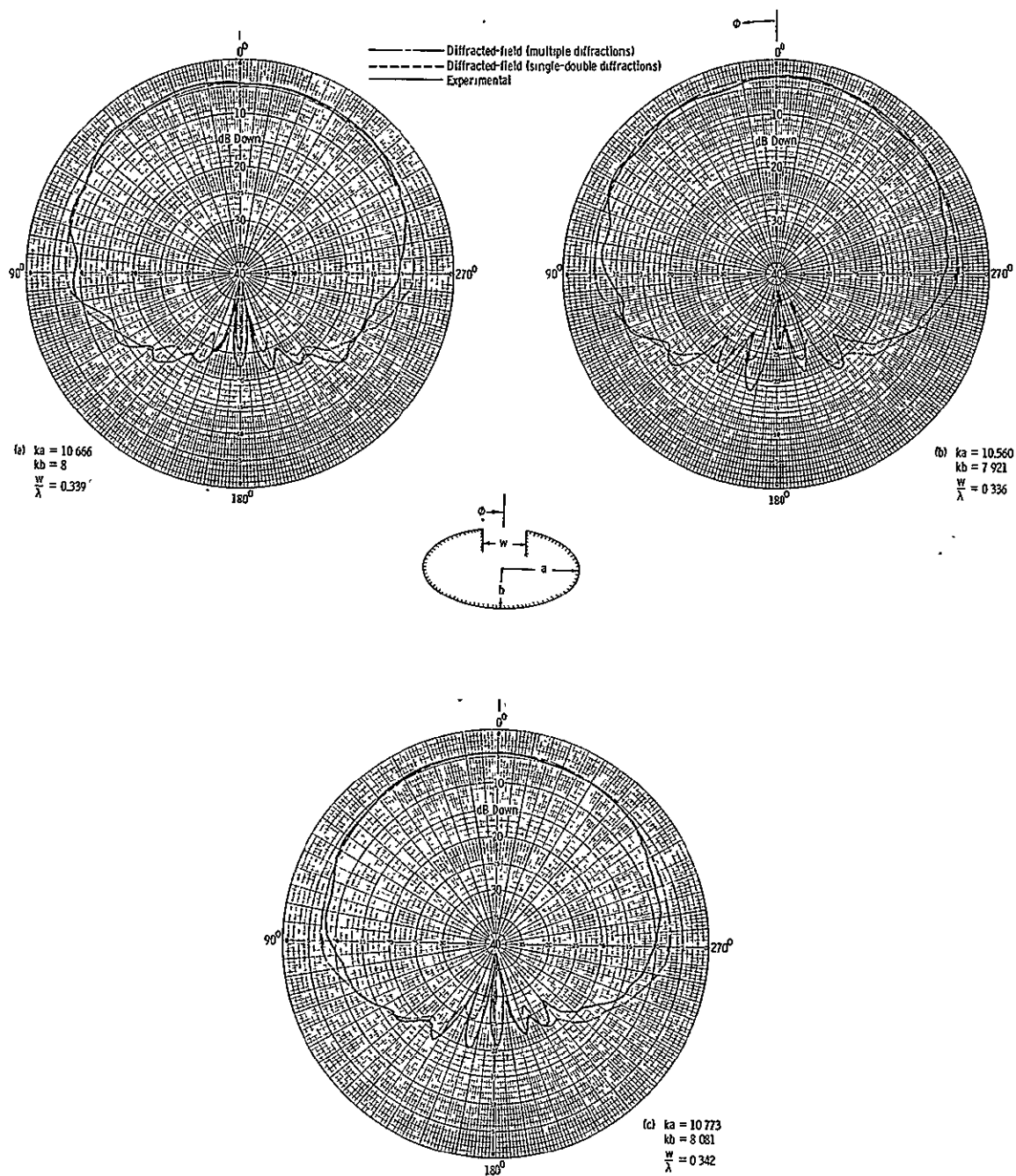
Plate X. Comparison of radiation patterns for smaller size
elliptical cylinder (TEM mode).
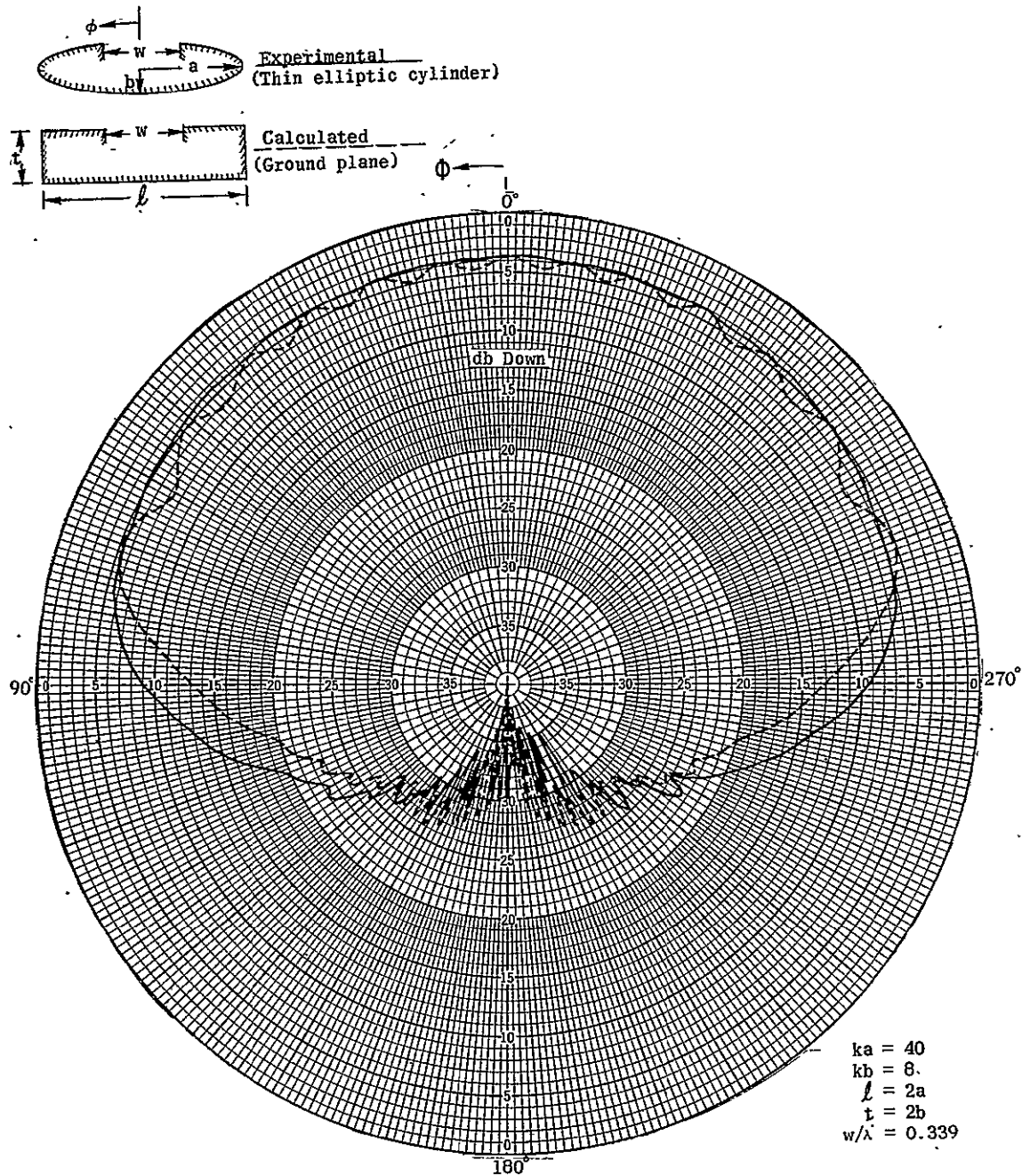
Figure 19. Radiation pattern of a thin elliptical cylinder and a
finite size ground plane (TEM mode).

assumed that such a relation holds for an elliptical cylinder, and the experimental results were obtained using finite axial slots. The experimental models were also of finite length of about 30 wavelengths; diffractions from the edges of the cylinders should then be negligible. Dimension construction accuracies were within $\pm\lambda/25$ and surface irregularities within $\pm\lambda/50$. All measurements were performed at a frequency of about 10 GHz.

The agreement between computed and experimental patterns is good particularly in the forward hemisphere. Errors of the order of 2-3 dB are obtained in the penumbra region and they indicate that further improvement could be made on the approximations of the parallel-plate-cylinder geometry by a wedge and those implicit in Equations 123 and 124. The use of the half-plane wall for certain diffractions processes would yield improved results near the penumbra region as has been discussed previously for the circular cylinder. In general, the errors in the shadow region are of the same order of magnitude, and they are quite acceptable for determining possible interference and noise that might be introduced from other systems through these back lobes.

For elliptical cylinders with constant major axis but decreasing minor axis (thinner shape ellipse), the rate of attenuation of the creeping waves, whose main contribution is in the "shadow" region, is larger. However, the "lit" region radiation, whose primary source is the wedge-diffracted fields, is essentially unaffected as shown on Plate IX(a)-(c). The creeping waves are strongly influenced by the radius of curvature which is rapidly changing while the wedge-diffracted

fields depend on the included angle of the wedges (WA) which remains essentially constant.

For the small elliptical cylinder (ka = 10.666, kb = 8) of Plate X(a) slightly larger variations and asymmetries between experiment and theory are noted. For ±1.0 percent changes in frequency (Plate X(b),(c)), the variations and asymmetries are even greater and it is believed that the physical construction tolerances of the elliptical cross section are critical for the measurements on this size body. For a thin elliptical cylinder the radius of curvature of the surface near the major axis is small and any diffractions from that region would not be very accurate since the asymptotic series assumption of large physical dimensions is not well satisfied.

In Figure 19, the experimental pattern of a thin elliptical cylinder (ka = 40, kb = 8) is compared with a theoretical curve of a finite size ground plane obtained using wedge diffraction techniques. A good agreement is noted in the $90^{\circ} < \phi < -90^{\circ}$ region. However, in the $90^{\circ} > \phi > -90^{\circ}$ region the ripples predicted by the computed curve of the ground plane do not appear in the experimental curve for the thin elliptical cylinder. The surface of the cylinder is smooth and has no sharp edges to contribute diffractions in the "lit" region for the ripples to appear. The fact that edge diffracted fields do disturb the pattern is an interesting fact to the antenna designer who would certainly prefer the smooth pattern. Cylindrical caps on the sides of the ground plane would reduce the ripples and smooth the pattern.

To check the validity of the half-plane (n = 2) approximation for the parallel-plate-cylinder geometry instead by a finite wedge (n ≠ 2),

Equations 149 and 150 were used with modified n's and the computed results were compared with experimental results. It was found by comparison, like for the circular cylinder, that the best approximation was to replace the edge 1 geometry by a half-plane (n = 2) for the first order diffraction and by a finite wedge (n ≠ 2) for second and higher order diffractions for the 0°-180° pattern measured in the counter-clockwise direction. The edge 2 geometry was replaced by a finite wedge for all orders of diffraction. For the 180°-360° pattern, the approximations of edge 1 geometry are valid for edge 2 and vice-versa.

The computed results using the above approximations are shown on Plate XI, where they are compared with the experimental curves. It is seen that the above approximations result in better accuracies in the penumbra region than the finite wedge approximation but larger variations exist in all other regions. As concluded previously, the solution used then depends on the region of space of interest. It should be noted that computed results for single-double diffractions and multiple diffraction shown on Plates IX, X, and XI are almost the same, and it is rather difficult to distinguish any variations between the two.

Equatorial Plane Pattern of Circumferential Slots Operating in the TE_{10} Mode

As was explained previously, the TE_{10} mode is represented by two plane TEM mode waves reflecting obliquely back and forth between the waveguide walls with the electric field being parallel to the edge of the walls. The finite wedge approximation for the parallel-plate-cylinder geometry will not satisfy the boundary conditions and the half-plane approximation will be used.
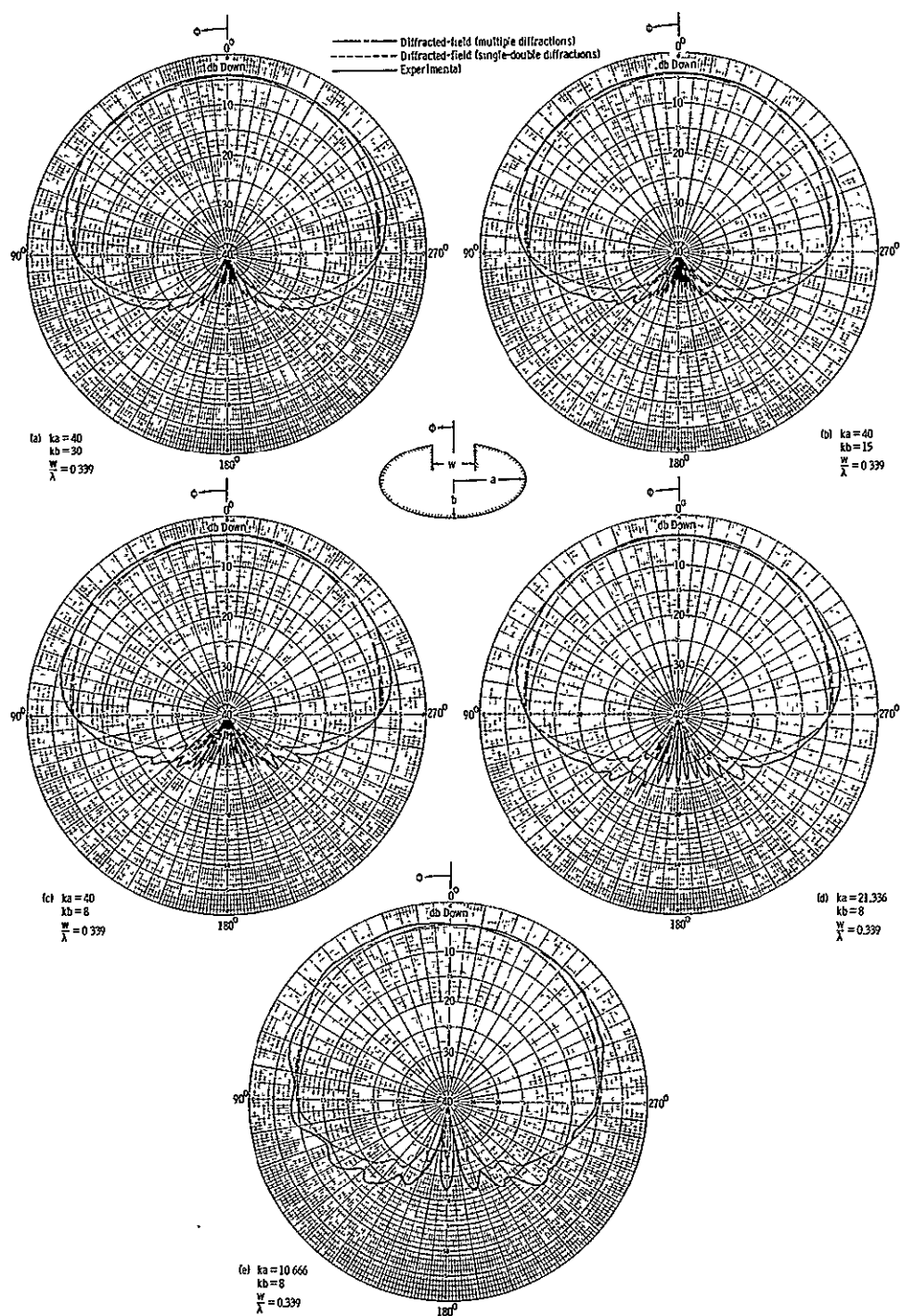
Plate XI. Radiation patterns of axial slot on elliptical conducting cylinder using half-plane and finite wedges (TEM mode).

For a circumferential slot operating in the TE_{10} mode and mounted on a circular cylinder it was found that the best approximation was to replace edge 1 by a half-plane (n = 2) for the first order diffraction and by a finite wedge (n ≠ 2) for the second and higher order diffractions for the $0°$-$180°$ pattern measured in the counterclockwise direction. The edge 2 geometry was replaced by a finite wedge for all orders of diffraction. For the $180°$-$360°$ pattern, the approximations of edge 1 geometry are valid for edge 2 and vice-versa.

The above approximation will be used also for the elliptical cylinder. The wedge-diffracted field is given by Equations 81-83 with n's modified as explained above. The creeping wave field is given by

$$E_C(\phi) = V_A e^{-jkt_1} e^{-\int_o^{t_1} \alpha_{os}(\rho)ds} + V_B e^{-jkt_2} e^{-\int_o^{t_2} \alpha_{os}(\rho)ds} \quad (154)$$

where

$$\int_o^t \alpha_{os}(\rho)ds = \frac{(k)^{1/3}}{2}\left(\frac{9\pi ab}{4}\right)^{2/3} e^{j\ \pi/6} \times$$

$$\int_{\phi_{11}}^{\phi_{12}} \frac{ab\ d\phi}{\left[(a^4\cos^2\phi + b^4\sin^2\phi)(a^2\cos^2\phi + b^2\sin^2\phi)\right]^{1/2}} \quad (155)$$

The regions where the appropriate wedge-diffracted and creeping wave fields are applicable are identical to those shown in Table 3 for the TEM mode.

The computed results for the TE_{10} mode slot on an elliptical cylinder are shown on Plate XII. Like for the circular cylinder, the single-double diffraction solution has a discontinuity in the $\phi = \pm 90^{\circ}$ directions because higher order diffractions are neglected. The thin-walled guide approximation ($n = 2$ for all order of diffraction) could also be used as was demonstrated for the circular cylinder. Good results would also be obtained in this case.

Diffracted-field (multiple diffractions)
Diffracted-field (single-double diffractions)

(a) ka = 40
kb = 30
$\frac{W}{\lambda}$ = 0.762

(b) ka = 40
kb = 15
$\frac{W}{\lambda}$ = 0.762
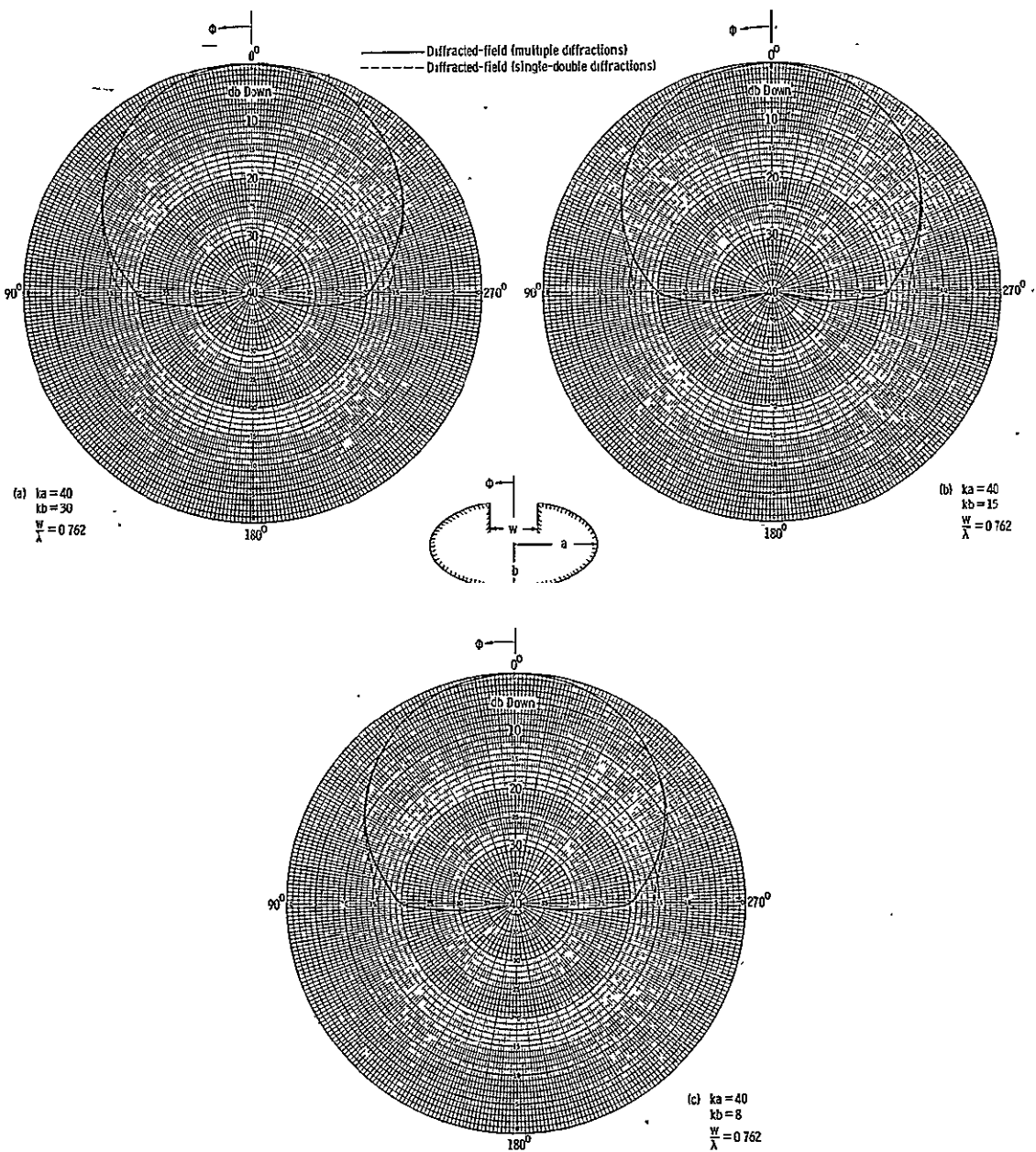
(c) ka = 40
kb = 8
$\frac{W}{\lambda}$ = 0.762

Plate XII. Radiation patterns of circumferential slot on elliptical conducting cylinder using half-plane and finite wedges (TE_{10} mode).

CHAPTER V

MUTUAL COUPLING BETWEEN SLOTS ON A CYLINDER

The coupling between two or more waveguide apertures on the surface of a cylinder is calculated using wedge diffraction and creeping wave theory. Mutual coupling is defined[30] as follows:

$$\text{Mutual Coupling} = \frac{\text{Modal current (or voltage) in coupled guide}}{\text{Modal current (or voltage) in transmitting guide}} \quad (156)$$

It should be noted that this quantity gives the phase as well as the magnitude of the coupling, and may be readily converted to mutual impedance or any other desired form for expressing coupling. The analysis of coupling will be formulated in the following manner. The transmitting guide, with its associated modal current, is replaced by an equivalent line source. The modal current induced in the coupled guide by a line source is determined. These two steps are then combined to obtain the mutual coupling.

The coupling problem considered in this discussion is described in Figure 20. The formulation of the solution to the coupling problem is as follows. A unit-amplitude wave with its associated modal current is incident in the transmitting guide. An equivalent line source, having an omnidirectional pattern and a field matching that of the guide in the direction ϕ_t, is substituted for the transmitting guide. A coupled
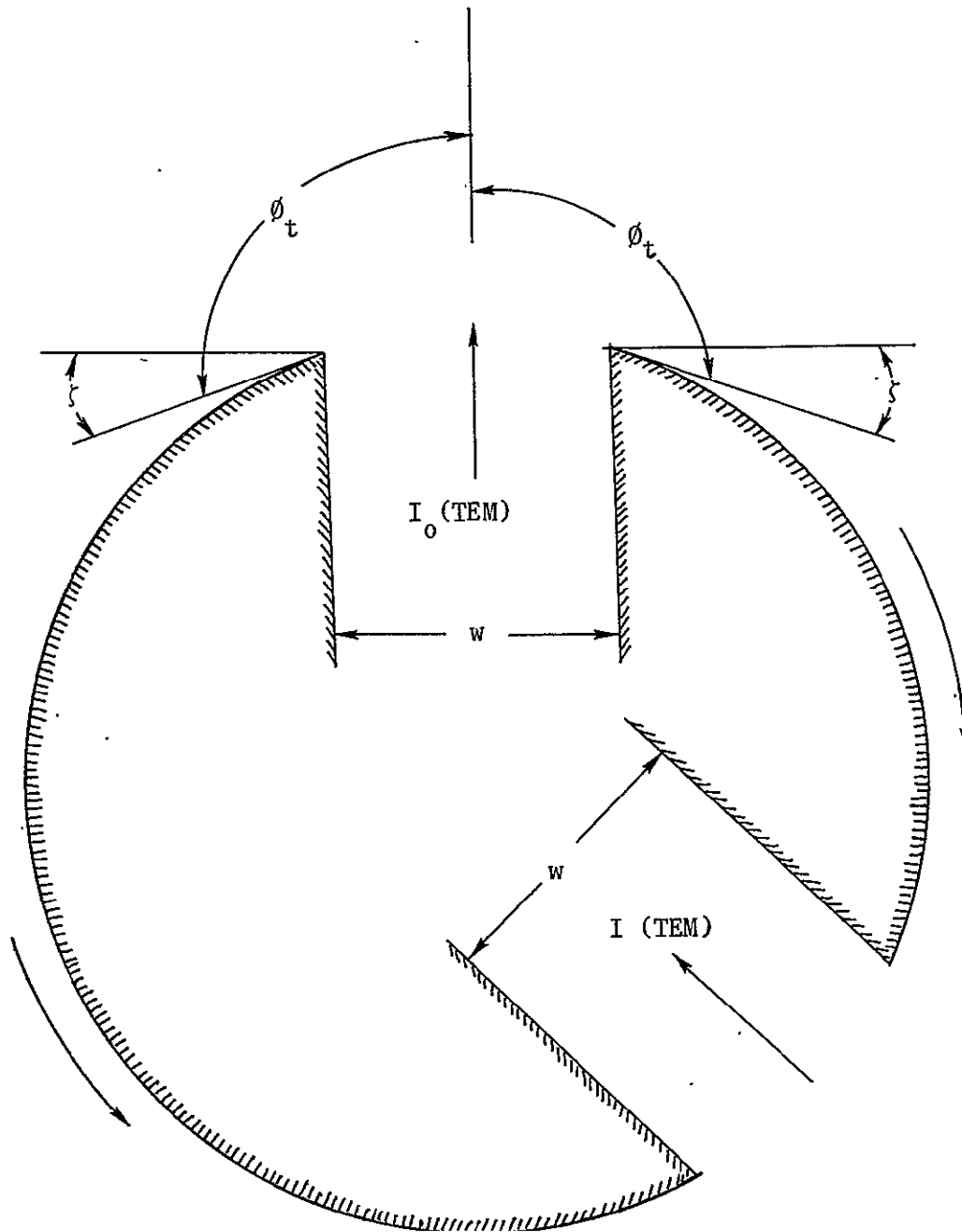
Figure 20. Coupling between parallel-plate waveguide slots on a cylinder.

wave with its associated modal current is induced in the receiving guide. The mutual coupling is defined as the ratio of the modal quantity in the coupled guide to that of the transmitting guide.

TEM Mode

For the TEM mode, the field component perpendicular to the plane of Figure 20 is the magnetic field. The incident field is uniform across the guide width, and thus the incident power flow for a unit-amplitude magnetic field is given by

$$P_O = wZ_O, \qquad Z_O = \sqrt{\frac{\mu_O}{\epsilon_O}} \tag{157}$$

The modal current associated with this mode is

$$I_O = \sqrt{w} \tag{158}$$

The replacement of the guide by a uniform equivalent line source is illustrated in Figure 21. The field radiated by the equivalent line source is equated to the field radiated by the guide, thus

$$I_1 \frac{e^{-j(kr - \pi/4)}}{\sqrt{2\pi r}} = H_{TO}(r, \phi_t) = D_{TO}(\phi_t)\frac{e^{-jkr}}{\sqrt{r}} \tag{159}$$

where $D_{TO}(\phi_t)$ is the diffraction coefficient of the transmitting guide in the direction ϕ_t. The modal current I_1 is that of the equivalent line source with an antenna impedance Z_O, and is given by

$$I_1 = \sqrt{2\pi}\, D_{TO}(\phi_t)e^{-j\,\pi/4} \tag{160}$$
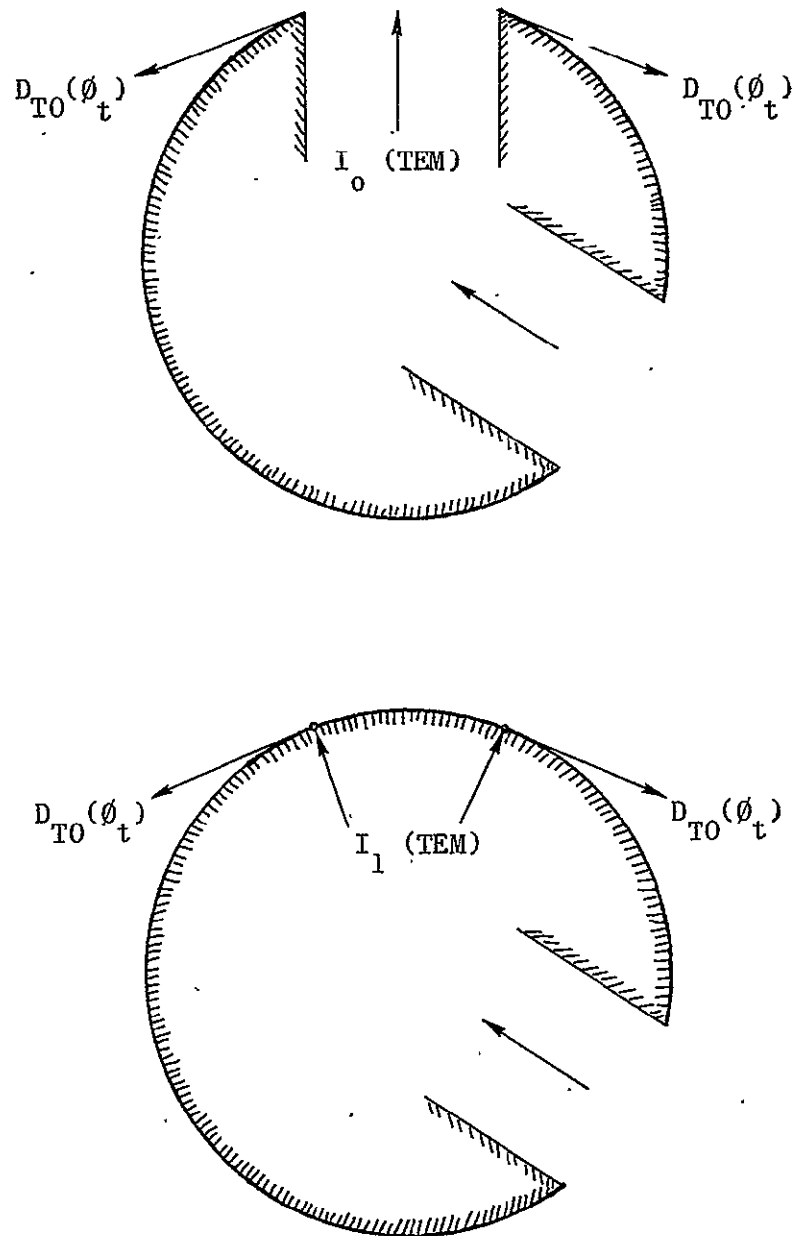
Figure 21. Equivalent line source for transmitting guide.

A principal criterion for the validity of this analysis is the accuracy of substituting the equivalent line source for the guide.

The modal current induced in the receiving guide by the equivalent line source is obtained by application of reciprocity, as illustrated by Figure 22. The modal current induced in a line source by a guide excited by a modal current I_1 will be obtained. The power received by the line source, being the product of the effective aperture width of the line source $\lambda/2\pi$, multiplied by the power density, is given by

$$P = \frac{\lambda}{2\pi} Z_o \left[\left| H_{T1}(Q_1) - H_{T2}(Q_2) \right|^2 \right] \tag{161}$$

where $H_{T1}(Q_1)$ and $H_{T2}(Q_2)$ are the fields of the receiving guide at points Q_1 and Q_2 as shown in Figure 22. The modal current received by the line source is thus given by

$$I = \sqrt{\frac{\lambda}{2\pi w}} \left[H_T(Q_1) - H_T(Q_2) \right] I_1 \tag{162}$$

where

$$H_T(Q_1) = V_{i1} e^{-jkt_1} e^{-\int_o^{t_1} \alpha_{oh}(\rho)ds} \tag{163}$$

$$H_T(Q_2) = V_{i2} e^{-jkt_2} e^{-\int_o^{t_2} \alpha_{oh}(\rho)ds} \tag{164}$$
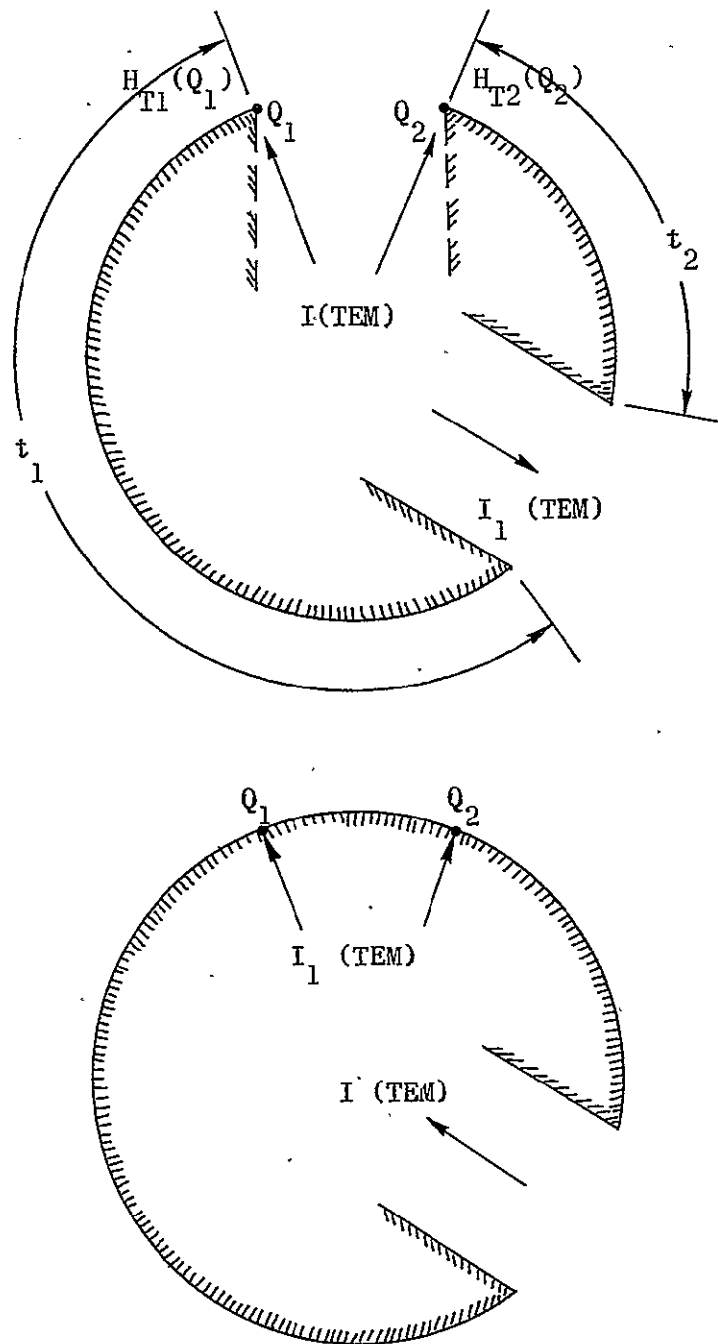
Figure 22. Use of reciprocity to obtain response of parallel-plate guide to line source.

By reciprocity, this is the modal current induced in the guide by the line source excited by a modal current I_1.

The mutual coupling for the TEM mode is obtained by taking the ratio of the modal current in the coupled guide to the modal current in the transmitting guide. Using Equations 158, 160, and 162, the mutual coupling is given by

$$\frac{I}{I_o} = \frac{\sqrt{\lambda}}{w} D_{TO}(\phi_t)e^{-j\,\pi/4}\left\{ H_T(Q_1) - H_T(Q_2) \right\} \tag{165}$$

Computed results of mutual coupling between two slots operating in the TEM mode on a circular conducting cylinder are shown in Figure 23 for different size cylinders and compared with data from a flat ground plane.[30] It is seen that the coupling decreases as the relative position between the two slots increases and it would be zero when the two slots are diametrically opposite since the two creeping waves would cancel in the second slot. It should be noted that the phase of the coupling is also available from this analysis. Since theoretical determination of coupling by conventional methods is difficult and experimental data are not available, no comparison can be made.

Figure 23. Mutual coupling between slots on a circular conducting cylinder (TEM mode) and on ground plane.

CHAPTER VI

CONCLUSIONS

Wedge diffraction and creeping wave theory have been used to
analyze the radiation properties of slots on cylindrical bodies. Using
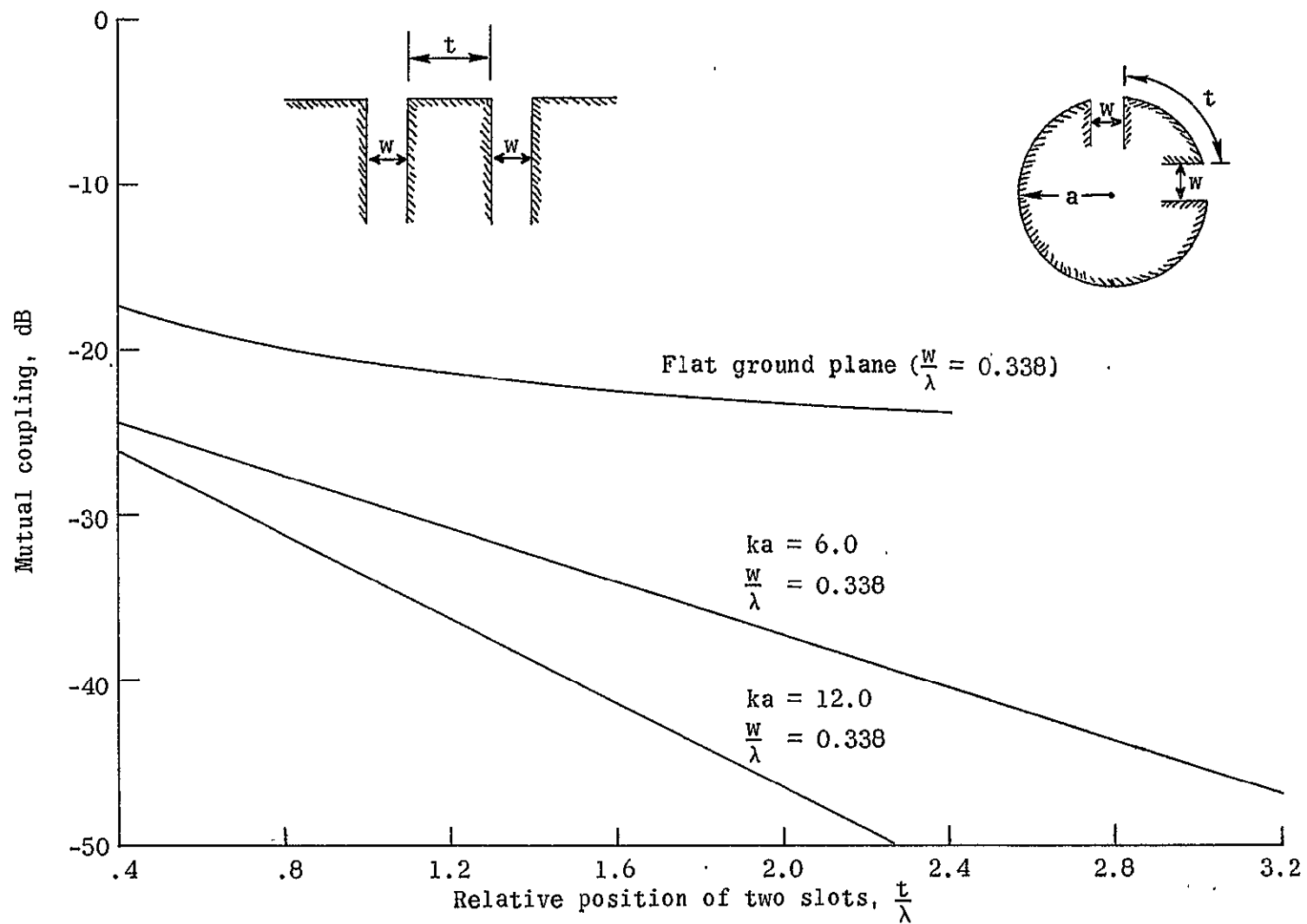this technique, the computed results for circular and elliptical
cylinders have been favorably compared with existing modal solutions and
experimental results. Three models representing the parallel-plate-
cylinder geometry have been introduced and their validity verified.

One model representing the parallel-plate-cylinder geometry was a
set of infinite wedges with finite included angle ($n \neq 2$). Such an
approximation served as a good model for TEM mode slots. Although the
physical structure of the antenna was comprised of flat and curved
surfaces forming an edge, a model of two flat surfaces forming an edge
was a good approximation for computing the diffracted fields in the lit
region. The values of the fields obtained in the penumbra region may
not have been very accurate, because of the presence of the wedge, but
it was demonstrated that good values can be obtained. Such a model can
be used in approximating other complex structures which may be similar
to the ones applied in this dissertation.

Another model representing the parallel-plate-cylinder geometry for
all orders of diffraction was a set of two flat ground planes ($n = 2$).
Even though the physical structure of such a model was quite different
from the actual antenna, it was demonstrated that it also served as a

good model for computing the diffracted fields in the lit region. Since wedge-diffracted fields are strongly dependent on the tip of the wedge, the edge of the flat ground plane was similar to that formed by the plate of the guide and the surface of the cylinder. For this case, the fields in the penumbra region were more accurate than for the previous model because there was no physical structure to interfere with the fields. This model can be used for TEM and TE_{10} modes and will give accurate results, as a first order of approximation, for a variety of structures which form a tip even though the physical structure may be different.

The third model used for approximating the edge region of the antenna was a half-plane in combination with a finite wedge in the following manner: replace the edge 1 geometry by a half-plane $(n = 2)$ for the first order diffraction and by a finite wedge $(n \neq 2)$ for second and higher order diffractions for the $0°-180°$ pattern measured in the counterclockwise direction. The edge 2 geometry is replaced by a finite wedge $(n \neq 2)$ for all orders of diffraction. For the $180°-360°$ pattern, the approximations of edge 1 were valid for edge 2 and vice-versa. It was demonstrated that this model also served as a good replacement for the parallel-plate-cylinder operating in the TEM and TE_{10} modes. It can also be used as a model for the wedge-diffracted fields of structures forming edges which may be similar to the ones for which it was applied in this dissertation.

As a result of the preceding, the antenna designer now has at his disposal three models for approximating edges formed by curved and flat surfaces. Each one will give good results as a first order

of approximation. However, since each one is more accurate in different regions, a combination of them will give better results.

For the TEM mode slots, all three models have been used in the computations. The computed results using the half-planes model and the half-plane in combination with the finite wedges approximation are more accurate for smaller guide widths in the penumbra region but the finite wedge approximation gives better results in all other space. However, as the guide width is increased, the finite wedge approximation gives better results in all regions.

For the TE_{10} mode slots, the parallel-plate-cylinder geometry cannot be approximated by a set of wedges of finite included angle because the tangential E-field boundary conditions are not satisfied. Therefore it was necsssary to use either the half-planes model or the half-plane in combination with the finite wedges approximation as a model. The computations agreed very closely with existing boundary-value solutions.

The elevation plane pattern of a finite length cylinder of an arbitrary cross section was computed using wedge diffraction techniques. The diffractions from the edges of the cylinder are taken into account and their contributions to the overall pattern are noted. As the aperture width is increased, the beamwidth of the main lobe is decreased. The smoothest pattern and the lowest back lobes are obtained for the guide whose width is exactly one wavelength since complete cancellation of the fields diffracted from wedges 1 and 2 along the cylinder surface ($\theta = \pm 90^{\circ}$) occurs. As the guide width is increased beyond one wavelength, additional lobes appear.

The maximum radiation of a slotted cylinder can be oriented in any desired direction by simply slanting the input guide. Such an orientation may be warranted to achieve desired radiation characteristics. The problem of mutual coupling between slots on a cylinder has been outlined. Computations have been carried out but cannot be compared since boundary-value or experimental data are not available.

The above technique used to analyze the radiation properties of aperture antennas on cylinders presents two problems: approximation of the aperture geometry by wedges and the excitation mechanism of the creeping waves. In other words, the representation of a complex geometry by simpler models whose solutions are known and the initiation of the creeping waves seem to be the main obstacles. It was found that a junction formed by a flat plate and a curved surface can be approximated by a wedge with infinite sides but finite included angle $(n \neq 2)$, by a half-plane $(n = 2)$ or by a half-plane in combination with a finite wedge as far as the diffracted fields are concerned. This agrees with Sommerfeld's conclusion that patterns on precise diffraction photographs exhibit almost no dependence on the shape of the diffraction edge and the fields diffracted by the wedges in the "lit" region are chiefly dependent on the region near the tip of the wedge.

All models give good results as has been demonstrated. Also it was found that the creeping waves can be initiated by using the wedge-diffracted field along the boundary which separates the "lit" and "shadow" regions as their initial value. This type of assumption preserves continuity of fields as it is necessary. However, this cannot very easily be established for any case. For example, creeping wave

theory along with image theory on curved surfaces was applied for the analysis of the radiation properties of a vertical infinitesimal stub on cylindrical bodies. The results obtained were compared with existing boundary-value solutions but a very poor agreement was indicated. A more practical case of a finite dipole might yield a creeping wave solution by segmenting the dipole. Each segment of the dipole would launch a creeping wave on the cylinder at the tangent point fixed by the height of the segment. There would also be a different "image" element for every radiation angle. This would represent a lengthy problem but its solution should be tractable.

TEM mode aperture field distributions can be realized in practice using H-plane sectoral horns of several wavelengths. This type of field realization was used for the elevation plane pattern experimental measurements. The computed results agreed very closely with the experimental data which indicates that the assumed aperture field distribution is closely approached. However, for circular cylinders, the equatorial plane radiation pattern function of an infinite axial TEM mode slot is the same as that of finite slot. It is assumed that such a relation holds for elliptical cylinders and experimental measurements of TEM mode axial slots were carried out using standard rectangular waveguide feeds. A comparison between computed and experimental results indicated a very good agreement which justifies its validity.

The essential feature of this technique is that it is applicable to all types of complicated problems some of which are, in general, impractical to solve rigorously. The approach is to resolve a complicated problem into simpler component problems with approximations, if necessary,

such that each of them will have a simple rigorous solution. The known

solutions of these individual components permit the calculation of the

overall radiation pattern by the use of superposition. Other analyses,

such as the point-matching technique have been developed for the solu-

tion of complicated antennas. However, the point-matching approach

yields good results for antennas and supporting structures whose

electrical size is small, resulting in a set of N linear equations

which are within the capacity of present digital computers to handle

and the time involved in such computations is great resulting in a high

cost per data point. The analysis presented in this dissertation based

on the geometrical theory of diffraction and creeping wave theory yields

approximate results with relatively little expenditure of computer time.

Also, since the field contribution from each individual component is

separated, this technique is ideal in parametric design problems.

Individual parameters can be varied and their effect to the overall

pattern studied.

Another possible approach to the solution of a complicated problem

would be an asymptotic series expansion for each problem of interest.

However, such an approach presents difficulties. First of all, an

asymptotic series expansion may not always be very convenient due to

the complexity of the formulation. Secondly, even if such an analysis

is possible, it is applicable only to that individual problem at hand.

A slight variation in the geometry would require a new derivation which

in some cases may not be possible. The technique outlined in the main

text, although less accurate, provides solutions to general type of

problems with only slight variations. It should be pointed out that

data obtained with the above technique are well within measured accuracies.

The concept of a hybrid solution utilizing wedge diffraction and creeping wave theory has been established in solving aperture antenna problems on cylindrical bodies that have not been considered previously from this point of view or problems that otherwise may not be possible to solve in any other way. The first attempt was to apply this technique to bodies with known boundary-value solutions for comparison of the results. It was then extended to more complicated geometries where exact solutions are not possible but where experimental data are available. Once a good understanding of the radiation mechanism is established, the technique can be extended to other more complex geometries to include slots on spheres, prolate spheroids, ogives, etc. Also problems involving dipoles on the surface of such geometric shapes should be considered. Experimental data and modern computational methods such as the point-matching boundary-value techniques should be used to obtain improved values and gain better understanding of the radiation mechanisms involved.

Another possibility would be to combine solutions of the type given in this dissertation with the computer techniques. For example, the case of the monopole antenna on a cylinder would use point-matching methods to find the fields in the vicinity of the monopole and the diffraction concepts would be used over the remainder of the cylinder. This would greatly extend the size cylinder that could be treated using point-matching techniques.

APPENDIX

DIFFRACTION BY A PERFECTLY CONDUCTING WEDGE

The diffracted field for a plane wave incident on a wedge of included angle $(2 - n)\pi$ shown in Figure 24 is given by

$$E_D(r,\psi,\psi_0,n) = V_B(r,\psi - \psi_0,n) \pm V_B(r,\psi + \psi_0,n) \qquad (166)$$

where the plus sign applies for the polarization of the electric field perpendicular to the edge

$$\left(\frac{\partial E}{\partial n}\bigg|_{\text{wedge}}\right) = 0 \qquad (167)$$

and the minus sign applies for polarization parallel to the edge

$$\left(E\big|_{\text{wedge}}\right) = 0 \qquad (168)$$

The wedge diffraction function $\left[V_B(r,\psi \mp \psi_0,n)\right]$ for a plane wave has been determined by Pauli[18] and improved by Hutchins.[19]

The improved form of the diffraction function is defined as

$$V_B(r,\psi \mp \psi_0,n) = I_{-\pi}(r,\psi \mp \psi_0,n) + I_{+\pi}(r,\psi \mp \psi_0,n) \qquad (169)$$
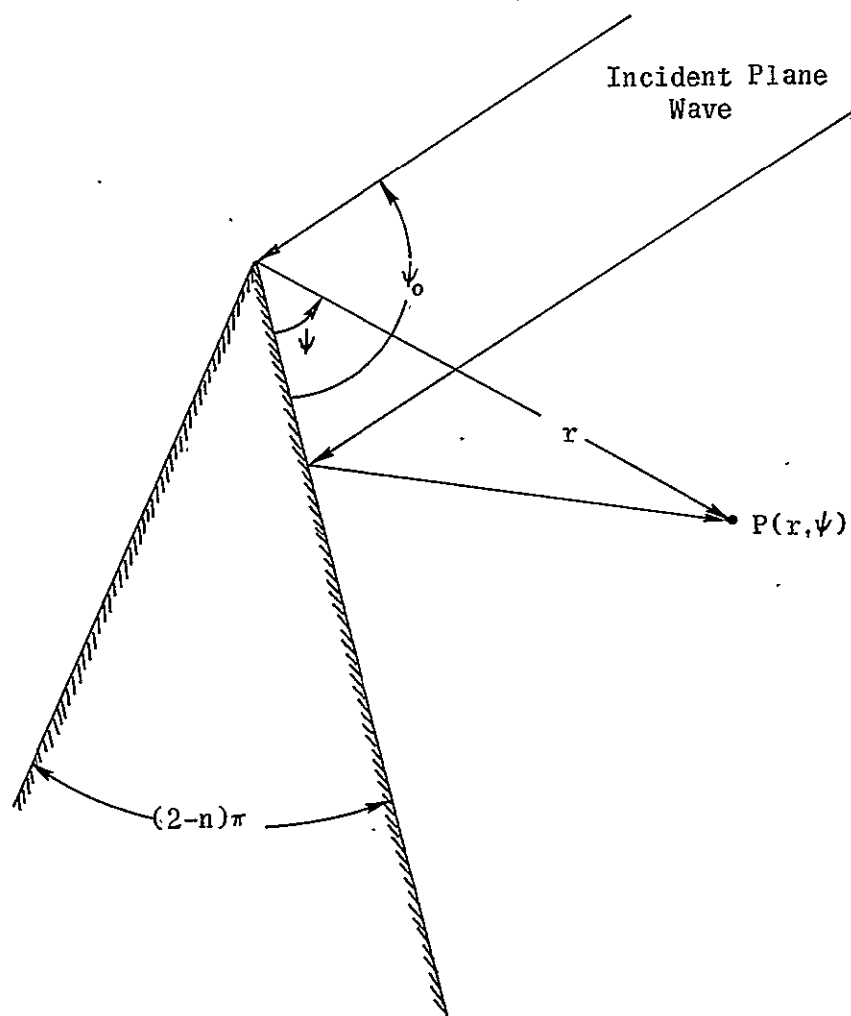
where

109

Figure 24. Diffraction by a wedge of included angle $(2 - n)\pi$.

$$I_{\pm\pi}(r, \psi \mp \psi_0, n) \sim \frac{e^{-j(kr + \pi/4)}}{jn\sqrt{2\pi}} \sqrt{a} \cot\left[\frac{\pi \pm (\psi \mp \psi_0)}{2n}\right] e^{jkra} \int_{\sqrt{kra}}^{\infty} e^{-j\tau^2} d\tau$$

$$+ \text{ Higher order terms} \tag{170}$$

$$a = 1 + \cos\left[(\psi \mp \psi_0) - 2n\pi N\right] \tag{171}$$

and N is a positive or negative integer or zero which most nearly satisfies the equation

$$\left.\begin{array}{ll} 2n\pi N - (\psi \mp \psi_0) = -\pi & \text{for } I_{-\pi} \\ 2n\pi N - (\psi \mp \psi_0) = +\pi & \text{for } I_{+\pi} \end{array}\right\} \tag{172}$$

Equation 170 contains the leading terms plus higher order terms which are negligible for large values of kr. For large values of kra Equation 170 reduces to the form presented by Pauli and given by

$$V_B(r, \psi \mp \psi_0, n) = \frac{e^{-j(kr + \pi/4)}}{\sqrt{2\pi kr}} \frac{\frac{1}{n} \sin\left(\frac{\pi}{n}\right)}{\cos\frac{\pi}{n} - \cos\left(\frac{\psi \mp \psi_0}{n}\right)} + \ldots \tag{173}$$

The diffracted field of Equation 173 is that from which the asymptotic diffraction coefficients of the geometrical theory of diffraction are obtained.[10] This expression is not valid in the shadow boundary because $a = 0$ there.

The solution for cylindrical wave diffraction at large distances from the edge can be determined by the use of the principle of reciprocity together with the solution for plane wave diffraction.[6]

For plane wave incidence the diffracted field at observation point P of cylindrical coordinates (r, ψ) as shown in Figure 25(a) is given by $V_B(r, \psi, n)$ of Equation 169. Now consider the situation in Figure 25(b) in which the wedge is illuminated by a cylindrical wave with its source at (x_0, ξ_0). By reciprocity the diffracted field V_A in the direction ξ is equal to the diffracted field V_B which is located at the point $(r = x_0, \psi = \xi_0)$ with a plane wave incident from the direction $\psi_0 = \xi$.
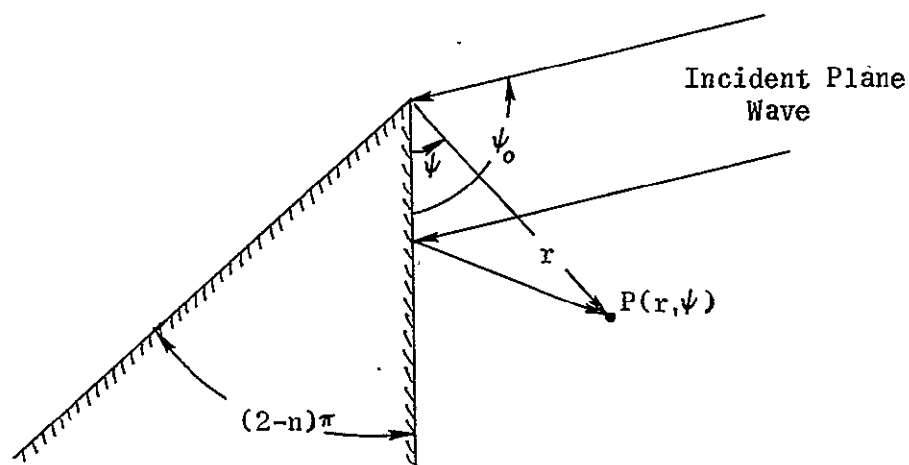
(a)
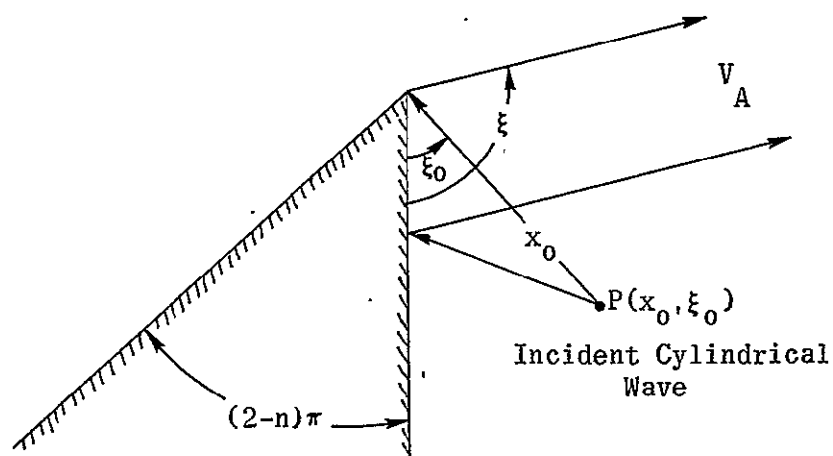
(b)

Figure 25. Illustration of reciprocity.

BIBLIOGRAPHY

1. Silver, S., and Saunders, W. K. "The Radiation from a Transverse Rectangular Slot in a Circular Cylinder," Journal of Applied Physics, 21(August, 1950), 745-749.

2. Bailin, L. L. "The Radiation Field Produced by a Slot in a Large Circular Cylinder," IRE Transactions, AP-3(July, 1955), 128-137.

3. Wait, J. R. "Radiation Characteristics of Axial Slots on Conducting Cylinder," Wireless Engineer, (December, 1955), 316-322.

4. Harrington, R. F. Time Harmonic Fields. New York: McGraw-Hill, 1961, Pp. 245-254.

5. Wait, J. R. Electromagnetic Radiation from Cylindrical Structures. New York: Pergamon Press, 1959, Pp. 88-104.

6. Rudduck, R. C. "Application of Wedge Diffraction To Antenna Theory," Report 1691-13, Antenna Laboratory, The Ohio State University Research Foundation; prepared under Grant NsG-448, National Aeronautics and Space Administration, Office of Grants and Research Contracts, Washington, D.C., June 30, 1965. ———

7. Ryan, C. E., and Rudduck, R. C. "Radiation Patterns of Rectangular Waveguides," IEEE Transactions on Antennas and Propagation, AP-16 (July, 1968), 488-489.

8. Ryan, C. E., and Rudduck, R. C. "A Wedge Diffraction Analysis of the Radiation Patterns of Parallel-Plate Waveguides," IEEE Transactions on Antennas and Propagation, AP-16(July, 1968), 490-491.

9. Rudduck, R. C., and Yu, J. S. "Higher-Order Diffraction Concept Applied to Parallel-Plate Waveguide Patterns," Report 1691-16, Antenna Laboratory, The Ohio State University Research Foundation; prepared under Grant NsG-448, National Aeronautics and Space Administration, Washington, D.C., October 15, 1965.

10. Keller, J. B. "Diffraction by an Aperture," Journal of Applied Physics, 28(April, 1957), 426-444.

11. Keller, J. B. "Geometrical Theory of Diffraction," Journal of Optical Society of America, 52(February, 1962), 116-130.

12. Franz, W., and Depperman, K. "Theorie der Bengang Am Zylinder unter Berücksichtigung der Kreichwelle," Ann. Physik, 10(June, 1952), 361-373.

13. Levy, B. R., and Keller, J. B. "Diffraction by a Smooth Object," Communications on Pure and Applied Mathematics, 12(1959), 159-209.

14. Keller, J. B., and Levy, B. R. "Decay Exponents and Diffraction Coefficients for Surface Waves on Surfaces of Non-Constant Curvature," IRE Transactions, AP-3(December, 1959), 552-561.

15. Levy, B. R. "Diffraction by an Elliptic Cylinder," Journal of Mathematics and Mechanics, 9(1960), 147-165.

16. Kouyoumjian, R. G. "Asymptotic High-Frequency Methods," Proceedings of the IEEE, (1965), 864-875.

17. Sommerfeld, Arnold. Optics. New York: Academic Press, 1954, Pp. 245-265.

18. Pauli, W. "On Asymptotic Series for Functions in the Theory of Diffraction of Light," Physical Review, 54(December, 1938), 924-931.

19. Hutchins, D. L. "Asymptotic Series Describing the Diffraction of a Plane Wave by a Two-Dimensional Wedge of Arbitrary Angle," Ph.D. Dissertation, The Ohio State University, Electrical Engineering Department, (1967).

20. Oberhettinger, F. "On Asymptotic Series for Functions Occurring in the Theory of Diffraction of Waves by Wedges," J. Math. and Phys., 34(1955), 245-255.

21. Senior, T. B. A., and Goodrich, R. F. "Scattering by a Sphere," Proc. IEE, 111(May, 1964).

22. Hong, S. "Asymptotic Theory of Diffraction by Smooth Convex Surfaces of Nonconstant Curvature," Technical Report No. 2, The University of Michigan, Department of Electrical Engineering Radiation Laboratory, Contract AF 04(694)-834, August, 1966.

23. Kinber, B. Ye. "Asymptotic Solution of the Problem of Diffraction by a Sphere," Telecommunications and Radio Engineering, No. 10, October, 1966.

24. Ryan, C. E. Jr. "Memorandum on Analysis of Echo Area of Targets Using Geometrical Theory of Diffraction and Creeping Wave Theory," Report 2430-1, ElectroScience Laboratory, The Ohio State University, Department of Electrical Engineering, Columbus, Ohio, May 22, 1967.

25. Peters, L. Jr., and Ryan, C. E., Jr. "The Relation of Creeping Wave Phenomena to the Shadow-Zone Geometry," GISAT III Symposium, 1967.

26. Ryan, C. E. "A Geometrical Theory of Diffraction Analysis of the Radar Cross Section of a Sectionally Continuous Second-Degree Surface of Revolution," Technical Report 2430-4, The Ohio State University, ElectroScience Laboratory, Department of Electrical Engineering, March, 1968.

27. Kinber, B. Ye. "Short-Wave Asymptotic Diffraction of Acoustic and Electromagnetic Waves from Surfaces of Revolution," Radiotechnika, 20(1965), 101.

28. Russo, P. M., Rudduck, R. C., and Peters, L. Jr. "A Method for Computing E-Plane Patterns of Horn Antennas," IEEE Transactions on Antennas and Propagation, AP-13(March, 1965), 219-224.

29. Obha, Y. "On the Radiation Pattern of a Corner Reflector Finite in Width," IEEE Transaction on Antennas and Propagation, AP-11(March, 1963), 127-132.

30. Dybdal, R. B., Rudduck, R. C., and Tsai, L. L. "Mutual Coupling Between TEM and TE_{10} Parallel-Plate Waveguide Apertures," IEEE Transactions on Antennas and Propagation, AP-14 (September, 1966), 574-580.

31. Mikuteit, S. "Mutual Coupling in a Three-Element, Parallel-Plate Waveguide Array by Wedge Diffraction and Surface Integration Techniques," Report 2485-1, The Ohio State University Electro-Science Laboratory, Columbus, Ohio, August 30, 1967.

32. Rudduck, R. C., and Tsai, L. L. "Aperture Reflection Coefficient of TEM and TE_{10} Mode Parallel-Plate Waveguides," IEEE Transactions on Antennas and Propagation, AP-16(January, 1968), 83-89.

33. Burnside, W. D. "The Reflection Coefficient of a TEM Mode Symmetric Parallel-Plate Waveguide Illuminating a Lossless Dielectric Layer," Technical Report 1691-25, The Ohio State University, ElectroScience Laboratory, May, 1968.

34. Jones, J. E., Tsai, L. L., Rudduck, R. C., Swift, C. T., and Burnside, W. D. "The Admittance of a Parallel-Plate Waveguide Aperture Illuminating a Metal Sheet," IEEE Transactions on Antennas and Propagation, AP-16(September, 1968), 528-535.

35. Kraus, J. D. Electromagnetics. New York: McGraw-Hill, 1953, Pp. 446-450.

36. Wu, D. C. F., Rudduck, R. C., and Pelton, E., "Application of a Surface Integration Technique to Parallel-Plate Waveguide Radiation Analysis," IEEE Transactions on Antennas and Propagation, AP-17 (May, 1969).

37. Wu, D. C. F., and Rudduck, R. C., "Slope Diffraction Analysis of TEM Parallel-Plate Guide Patterns," Technical Report 1691-29, The Ohio State University, ElectroScience Laboratory, Department of Electrical Engineering, Columbus, Ohio.